N71-18990

CHARACTERISTICS OF SEPARATED FLOW REGIONS

WITHIN ALTITUDE COMPENSATING NOZZLES

Thomas J. Mueller, Wayne P. Sule

and Charles R. Hall, Jr.

Final Report UNDAS TN-029-FR-9

January, 1971

Prepared under Contract No. NSR 15-004-029 by

UNIVERSITY OF NOTRE DAME

NOTRE DAME, INDIANA

for

NATIONAL AERONAUTICS AND SPACE ADMINISTRATION

FORWARD

ABSTRACT

Results of an experimental and analytical investigation of
the characteristics of separated flow regions within altitude com-
pensating nozzles are presented. Experimental results for a planar
and an axisymmetric truncated plug nozzle are included while analyti-
cal results for planar and axisymmetric truncated plug and expansion-
deflection nozzles are presented. The experimental results include
extensive optical and pressure data covering nozzle operating char-
acteristics, diffuser effects, sonic line shape, lip shock strength,
turbulence effects and nozzle flow development. The extension
of the analytical method of Mueller and Hall to included nonuniform
nozzle flows produced the correct base pressure trends with overall
nozzle area ratio, base temperature ratio, ambient pressure ratio,
amount of base bleed, and initial boundary layer thickness as well
as good qualitative agreement between the experimental and analytical
flow fields when no strong internal shock was present. It was found
that the lip shock was not of significant strength in the cases
studied to warrant including it in the theory. Also it was found
that the sonic line shape was noticeably distorted and that the
separated free shear layer was turbulent under all conditions
studied.

iii

TABLE OF CONTENTS

LIST OF SYMBOLS

A,B,C,D	Coefficients of a general partial differential equation
A	Area
a	Velocity of Sound
B	Expression defined by Equation 2
C	Crocco number; Variable defined by Equation (I-34)
C_T	Thrust coefficient
F	Variable defined by Equations (I-34a) and (I-37b)
f	An arbitrary function
G_d	Base bleed rate (lb_m/sec)
g	Gravitational Constant (32.178 lb_m-ft/lb_f-sec^2)
h	Enthalpy
I_1, I_2, J_1, J_2	Integrals defined by Equations 3-6
K	Variable defined by Equation (I-35)
L	Plug length
M	Mach number
$\dot{m}$	Mass flow (lb_m/sec)
N	Recompression coefficient
n	Velocity profile power law exponent; direction normal to a streamline
P	Pressure
R	Radius
$\mathbb{R}$	Gas constant (=53.3 lb_f-ft/lb_m-$^\circ$R for air)
R'	Compressible divergence factor
r	Radius
s	Direction along a streamline

$\tilde{s}$	Entropy
T	Temperature
u	Velocity in x or X direction
V	Velocity
X, Y	Coordinates of the reference (inviscid) coordinate system
X', Y'	Planar Truncated Plug Nozzle Coordinates
x, y	Coordinates of the intrinsic (viscous) coordinate system
β	Base temperature ratio $(=T_{o1}/T_b)$
γ	Ratio of specific heats $(=c_p/c_v)$
δ	Boundary layer thickness
$\delta**$	Boundary layer momentum thickness
ε	$\doteq 0$ for planar flow; $= 1$ for axisymmetric flow
η, ξ	Distances along left-running and right-running characteristics, respectively
η	Dimensionless coordinate $(=\sigma y/x)$
θ	Streamline angle
$\varkappa$	Defined by Equation (18)
$\mathcal{H}$	Non-dimensional bleed number
Λ	Base stagnation temperature ratio $(=T_{ob}/T_{o1})$
μ	Mach angle $\left[= \sin^{-1} (1/M)\right]$
ν	Prandtl-Meyer turn angle
ρ	Density
σ	Jet spread parameter
Φ	Variable in the general partial differential equation
ϕ	Velocity ratio $(=u/u_a)$

Subscripts

1,2,3,4	Stations for the basic flow model
a	Conditions in the external stream adjacent to the mixing region; refers to ambient conditions
at	Atmospheric conditions
b	Conditions at the base of the plug
BL	Boundary layer
d	Streamline whose kinetic energy is just sufficient to enter the recompression region, diffuser, dew point temperature
ex	Exit conditions
inc	Incompressible value
i	Condition at the end of internal expansion
j	Condition along the jet boundary separating streamline
m	Coordinate shift in the mixing theory due to the momentum integral
max	Refers to a maximum value
ne	Nozzle exit
nt	Nozzle throat
o	Stagnation conditions
ol	Nozzle stagnation conditions
p	Refers to plug base
R	Condition along the R-streamline
r	Conditions at recompression
s	Sting
st	Second throat
sw	Sidewall
tc	Top contour
w	Wake

Superscripts

——	Average value
'	Position of points on the hodograph plane

LIST OF FIGURES

ix

INTRODUCTION

GENERAL REMARKS

Advanced rocket and air-breathing propulsion systems require ex-
haust nozzles that will perform efficiently over a wide range of ambient
operating conditions. Furthermore, these exhaust nozzles should be short,
lightweight, and relatively easy to cool. Analyses and tests have dem-
onstrated that a group of nozzles referred to as altitude compensating
nozzles satisfy these requirements. The expansion-deflection, truncated
plug, and aerospike nozzles are included in this group. Although in
the past, propulsion systems usually required axisymmetric exhaust nozzles,
non-axisymmetric (e.g., planar or three-dimensional) exhaust nozzles
appear attractive in some future rocket and hypersonic air-breathing
propulsion systems under consideration.

A viscous separated flow region and wake within the nozzle flow
field enables this type of nozzle to reduce over-expansion losses at
low altitudes and to produce a significant portion of the total thrust
during high altitude operation. To facilitate optimization of the
design, accurate prediction of performance, and the design of altitude
test facilities for this type of nozzle, it is desirable to calculate
the entire nozzle flow field. This necessitates a calculation of the
inviscid flow field and the viscous separated flow region and wake as
well as the viscous boundary layer along contour walls. Although nu-
merical calculation of inviscid flow fields using the method of char-
acteristics and contour boundary layers using momentum and energy in-
tegral methods are common, an adequate method for including separated
flow regions has not been established. The principal reason for this
deficiency is a lack of understanding of the separated flow region
submerged in the nonuniform nozzle flow field.

DESCRIPTION OF PROBLEM

The truncated plug and expansion-deflection nozzles shown in
Figs. 1 and 2 will be used in this discussion since they contain typi-
cal examples of a separated flow region within a nonuniform nozzle flow
field. The similar nature of the separated flow regions in other al-
titude compensating nozzles and other aerodynamic problems is apparent.

At low values of chamber to ambient pressure ratio the separated
flow region is "open" (i.e., sensitive to ambient conditions), and
unsteady in nature as shown in Fig. 1. As the chamber to ambient pres-
sure ratio increases the jet mixing region moves toward the nozzle
axis until it "closes". The structure of the separated flow region
is of particular interest after it "closes" since this represents de-
sign operating conditions. Although the base pressure and near wake
have usually been assumed to be independent of ambient conditions when
this region is "closed", recent data (Ref. 1) indicate that this is
not always the case. These results suggest that the near wake is not
"sealed off" at the neck but can be influenced by disturbances fed

upstream through this corridor even though the flow is slightly super-
sonic on the nozzle centerline. The portion of the trailing wake which
can feed disturbances upstream is referred to by Lees (Ref. 2) as sub-
critical. The location downstream of the neck where disturbances can
no longer be transmitted upstream (i.e., the change from subcritical
to supercritical) could be an important consideration in the design
of a diffuser system to test any nozzle with a wake of this type.

When the flow that has been accelerated in the contoured plug
portion of the nozzle reaches the corner of the plug base, the viscous
boundary layer negotiates the corner and then separates from the base
(Ref. 3) while the adjacent supersonic flow over-expands and then re-
compresses through the lip shock which originates in the vicinity of
the separation. The strength of the lip shock is a function of Mach
number, Reynolds number and corner geometry. The result is a "semi-
dead-air" or separated region in the middle of the nozzle flow field.
This separation region is surrounded by the high velocity nozzle flow
and may be completely laminar, completely turbulent or transional (i.e.,
transition occurring downstream of the plug base). At the interface
between these two portions of the nozzle flow field, there is a large
velocity difference which produces a strong shearing action. As a re-
sult of this shearing action between adjacent fluid elements, the high
velocity flow tends to entrain the gas from the separated or base re-
gion. The mechanisms involved in this entrainment process are similar
to those experienced in an ejector, thus, the familiar term "pumping"
is often used to describe the process.

The high velocity nozzle flow surrounding the separated base re-
gion attempts to "pump out" this region through the growth of a mixing
or shear layer along the interface. This mixing layer grows in size
as it progresses downstream from the edge of the base. At the separa-
tion point, its thickness is influenced by the size of the boundary
layer on the plug wall and whether it is laminar or turbulent.* As
this mixing layer grows downstream it encounters some form of recom-
pression region so that it eventually satisfies ambient conditions.
When the separated flow region is "open", recompression usually takes
place far downstream of the nozzle exit. However, when the separated
flow region is "closed" the mixing layer approaches the nozzle axis
and encounters a recompression region which is the result of a system
of compression waves or shocks generated in the inviscid flow field.
The shock system is necessary to turn the supersonic inviscid flow
parallel to the axis after it has been accelerated toward the nozzle
axis by the expansion about the corner of the plug base. The key to
the determination of the base pressure lies in the behavior of the

---

* The delay of transition from laminar to turbulent flow and even re-
verse transition from turbulent to laminar flow may occur in the con-
vergent section of a nozzle for low unit Reynolds numbers in the presence
of wall cooling (Ref. 4). Since propulsive nozzles are frequently
cooled cryogenicly, laminar and transitional flow have recently become
important and should be considered.

mixing layer in the presence of the high pressure recompression zone. As the mixing layer or shear flow approaches this high pressure region, it is decelerated accordingly. In fact, it will decelerate or be diffused until the static pressure in the shear flow layer nearly equals that behind the recompression zone. The type of velocity profile in the shear layer just before the recompression zone indicates that a significant portion of this layer has a relatively low velocity or kinetic energy. Since this portion of the shear layer does not have enough kinetic energy to get through the recompression region, it is recirculated back into the base region.

The separated flow regions described above may be further complicated when expansion and/or compression waves of the opposite family intercept the mixing and recompression regions. This situation frequently occurs in the truncated plug and aerospike nozzles and may occur in the E-D nozzle if the shroud contour is truncated or the plug is translated to off-design positions. The influence of base bleed is also important for this type of nozzle. The difficulties in analyzing the enclosed base region focus around the non-constant pressure jet mixing region and the recompression process at the end of the near wake, the subcritical nature of the trailing wake, and the possible intersection of these regions by expansion and compression waves.

SCOPE OF PRESENT WORK

The primary objective of this research was to obtain a better understanding of the characteristics of separated flow regions within altitude compensating nozzle flows in order to develop an analytical method of predicting these characteristics. As in all separated flow research, an experimental program was necessary to supply specific information and overall guidance for the analytical program.

In order to take full advantage of the flow visualization capabilities of the Notre Dame supersonic smoke tunnels (SST), the majority of the experiments were conducted with a planar truncated plug nozzle in this facility. Previous experiments with a planar expansion-deflection nozzle in the SST were also used. A smaller number of experiments were performed with an axisymmetric truncated plug nozzle in a blowdown nozzle thrust facility.

An iterative solution of the viscous separated flow region and the adjacent inviscid nonuniform flow was developed for both truncated plug and expansion-deflection nozzles. The separated flow region is determined by an integral method while the adjacent flow region is determined by the rotational method of characteristics. Parametric studies were made for several nozzle configurations. The parameters included: nozzle expansion ratio, the ratio of specific heats of the gas, base temperature ratio, base bleed ratio, and initial boundary layer thickness at the plug base.

Since analytical solutions to separated flow problems are at best very difficult, it is important that a reasonable number of definitive experiments precede any analytical effort. Consequently, the initial emphasis of this project was placed on the experimental phase. The altitude compensation characteristics of the plug nozzle were studied quantitatively from pressure measurements, etc., and qualitatively using several flow visualization techniques. Correlations of the measurements and visual flow patterns were made whenever possible.

PLANAR TRUNCATED PLUG NOZZLE FACILITY

A schematic of the planar truncated plug nozzle test facility is shown in Fig. 3a and a photograph of the facility is presented in Fig. 3b. Basically the installation consists of a contraction section, a planar truncated plug nozzle section, and a diffuser section. Following is a detailed description of these major components and also an outline of the auxiliary equipment employed for data acquisition.

Contraction Section

The contraction section is rectangular and converges in both directions. It was fabricated from 1/16 inch galvanized sheet steel which was welded together to form the desired contour. To insure a low turbulence level, screens were designed with tapered frames to mate with and conform to the contour of the metal contraction section. These screens were attached to the inlet of the metal section. Of the total of ten screens, the first two are 16 mesh bronze and the remaining eight are 24 mesh Nylon Marquisette. The overall contraction in area from inlet to the screens to the nozzle throat is about 200:1.

Plug Nozzle Section

The plug nozzle section (Fig. 4) was designed to fit between the contraction section and the diffuser of the existing indraft wind tunnel. The width of the existing diffuser section was 4.953 inches and this criterion fixed the width of the nozzle section at the same dimension. Based on the available mass flow of about 3.2 lbm/sec., the geometric throat height on each side of the plug was set at 0.74 inches producing an aspect ratio for each throat of 6.69. The plug which was fabricated from lucite was designed for an isentropic expansion to Mach 2. The aft portion of the spike was removed producing a 16% length truncated plug (i.e., the distance from the geometric throat to the plug base was 16% of the total distance from the geometric throat to the tip of the isentropic spike, as shown in Fig. 5). The truncated plug could be used with either a solid base plate for base pressure measurement or base plates of various porosity for base bleed studies. The coordinates of the nozzle contour and plug are given in Tables I and II, respectively, and the origins used for the coordinate tabulations are

shown in Fig. 5.

The overall geometric nozzle expansion ratio, A_{ne}/A_{nt} was 1.957 and the plug base area ratio of the truncated plug, A_b/A_{nt}, was 0.531. The plug nozzle discharges into a rectangular diffuser duct, A_d/A_{nt}= 3.8, which forms the remainder of the nozzle test section. The top of the nozzle test section was instrumented with a total of 33 static pressure taps. An aluminum sidewall plate was equipped with a total of 32 static pressure taps on the sidewall centerline.

The relative locations of the pressure taps and the numbering system are shown in Fig. 6. Table III gives the coordinates of the top contour pressure taps and the coordinates of the sidewall center-line taps are given in Table IV. Also the solid base plate for the truncated plug was furnished with 5 static pressure taps.

In order to study the effect of a diffuser on the flow field, two movable 10° ramp diffuser blocks were constructed of aluminum (Fig. 4). The second-throat contraction ratio, A_{st}/A_d was 0.644.

Diffuser Section and Vacuum Pumps

The planar truncated plug nozzle test section was connected to a standard, diverging channel diffuser which led to three rotary vacuum pumps. Each pump was able to deliver 3130 cubic feet per minute at 18 inches of Hg vacuum. By using various combinations of pumps and by bleeding into the system it was possible to obtain data over a range of exit pressures (or, since the total pressure was fixed at atmospheric pressure, a range of overall nozzle pressure ratios).

Flow Visualization Equipment

A standard single-pass, parallel-light schlieren system utilizing two 6-inch diameter parabolic mirrors was used in this investigation. The parabolic mirrors had a focal length of approximately 48 inches and were located 11 feet apart on the optical axis of the system. The viewing screen was made from the back of an 8 x 10 inch camera and the system included a shutter to facilitate taking schlieren photographs.

The standard schlieren system was converted to an opaque stop system by replacing the slit source by a circular source and the knife edge by a small circular opaque stop. This system produces a schlieren picture where undeflected light (i.e., no density gradient) hits the opaque stop producing a black background and deflected light misses the stop and appears white in the picture. The advantage of this technique is that the system is sensitive to density gradients in all directions perpendicular to the optical axis instead of just one.

The smoke generator and smoke rake are shown in Fig. 3. Smoke is generated by dripping kerosene on to electric strip-heaters in each

of the four legs of the generator. This vaporized kerosene or "smoke" is forced to the smoke rake by a squirrel cage blower. By passing through a system of vertical pipes the smoke is cooled to room temperature. The smoke then passes through an absorbent cloth bag which absorbs any large droplets or condensate. Finally the smoke passes through one or more of the horizontal tubes whose outlets are placed flush with the anti-turbulence screen at the contraction section inlet. These tubes introduce the smoke into the test section at any desired location. Lighting is a critical factor in taking smoke pictures and the best results were usually obtained by aiming two high-spot flood lamps through the glass sidewall of the test section at an angle of 45° to the flow.

Base Bleed Apparatus and Miscellaneous Equipment

In order to investigate the effects of base bleed on the nozzle flow field a 1/16 inch thick stainless steel plate with a filtration grade of 100 microns was fitted to the base of the truncated plug. A cavity inside the plug was supplied with air at atmospheric pressure and the air was then drawn through the porous base plate by the low pressure on the plug base. The air flow through the base was measured with a Rockwell Roto-Seal Gas Meter which is a rotary type positive displacement meter. The amount of bleed flow was regulated with a gate valve in the supply line.

To measure the static pressure variation along the geometric center of the nozzle section a special sliding tube probe was constructed and is shown in Fig. 7. This probe consisted of a slotted hypotube attached to the plug base and extending downstream through the diffuser and then through the tunnel sidewall. A second movable hypotube with a static pressure orifice was contained within the first. The static pressure orifice could therefore be translated along the geometric center of the nozzle by sliding the inner hypotube.

Other equipment necessary for taking data included two ten tube mercury manometer banks for pressure measurement, a sling psychrometer for wet and dry bulb temperatures, a mercury barometer for atmospheric pressure and assorted cameras and photographic equipment.

Experimental Procedure

Before starting the discussion of the experimental results it would be instructive to briefly outline the methods used to obtain and reduce the data. The details of these procedures are presented below.

Data Reduction

The static pressure readings from the manometer photographs were punched onto computer cards using a Wayne-George X-Y Coordinate Converter. The data was reduced with the UNIVAC 1107 Digital Computer. All static pressures were normalized with the nozzle total pressure (atmospheric pressure) and plotted by a Cal-Comp plotter. This technique

provided data which had a maximum error on the order of 2%.

DISCUSSION OF PLANAR NOZZLE RESULTS

The discussion of the experimental results will proceed in essentially two phases. The first phase will pertain to the general operating characteristics of the facility and the establishment of the conditions under which reliable data can be obtained. The second phase will concentrate on a presentation of the results which provided insight into the analytical calculation of the nozzle flow field.

Water Vapor Condensation

Since the nozzle was supplied with air from the laboratory, and since no equipment was available to dry or heat the air, condensation of water vapor in the nozzle flow must be considered before interpreting the data. Static pressures including the base pressure can deviate substantially from their true values (Ref. 1) due to the effect of condensation. The base pressure ratio, P_b/P_{o1}, for various dew point temperature is presented in Fig. 8. These results show that P_b/P_{o1} remains constant up to a dew point of at least $30^{\circ}F$. Due to the degree of subcooling, condensation was present under all operating conditions. However, the data demonstrate that, up to a dew point of $30^{\circ}F$, the amount of water vapor in the air is small enough that it does not effect the results. The few values of P_b/P_{o1} above 30° indicate that, initially at least, the increase in base pressure with dew point is rather gradual. This information provides general guidelines as to when the effects of condensation must be considered. A more detailed discussion of this problem is given in Ref. 1.

Operating Characteristics and Diffuser Effects

Before proceeding with a detailed discussion of the operating characteristics and diffuser effects, it would be helpful to compare the sidewall centerline static pressure distribution with the geometric center distribution as measured with the sliding tube probe. These data are presented in Fig. 9 for the "open wake" case, and in Fig. 10 for the "closed wake" case. The two sets of data show good agreement with the maximum deviation in the region of interest being less than 9%. The peak in P_{sw}/P_{o1} at about 2.25 inches in Fig. 10 is due to the fact that, although the wake is "closed", the ejector system is unstarted. The pressure peak results from the shock system just downstream of the recompression point in the "closed wake". This figure demonstrates the accuracy with which the sidewall static pressure taps are able to record static pressure distributions with significant gradients. It is, therefore, possible to proceed using the sidewall centerline static pressure distribution with the confidence that the trends will be accurately recorded and that the values will be within a small percent of the geometric center values.

The truncated plug nozzle test facility is basically an ejector-

diffuser configuration commonly used in altitude test facilities.
(Ref. 5). In this type of facility it is extremely important to know
the starting characteristics as represented in Fig. 11. This figure
shows that the cell pressure ratio (point of measurement shown in Fig. 6)
decreases with decreasing overall pressure ratio (P_{ex}/P_{ol}) until $P_{ex}/P_{ol}=$
0.325. Further decreases in overall pressure ratio produce no change
in the cell pressure. The pressure ratio at which the cell pressure
first reaches its minimum value is the starting pressure ratio. As
long as the over-all pressure ratio is at or below the starting pressure
ratio, downstream pressure fluctuation cannot effect the nozzle flow
field. The starting point for the configuration also establishes the
altitude simulation limit since the minimum cell pressure represents
the minimum ambient pressure that can be simulated in the ejector-dif-
fuser system.

Figs. 12 and 13 show the variation in base pressure ratio versus
the cell pressure ratio with no diffuser and with a diffuser respec-
tively. Since the cell pressure is equivalent to the ambient operating
pressure of the nozzle, Figs. 12 and 13 are representative of the nozzle
operating characteristics. The presence of the diffuser does not appear
to noticeably affect the "open wake" nozzle operation. Also, in both
cases, with and without the diffuser, the wake "closes" at essentially
the same cell pressure ratio. However the data indicates a 10% decrease
in the "closed wake" base pressure with the diffuser present. This de-
crease may be caused in part by diffuser effects being transmitted
upstream through the sidewall boundary layer.

Another feature of the base pressure characteristic data in Fig. 12
is the apparent instability at $P_{cell}/P_{ol} = 0.23$. Schlieren observation
of the flow field at this cell pressure ratio showed that the nozzle
flow is indeed unstable at this point, switching alternately between
the "open wake" and "closed wake" configurations. The instability is
not clearly evident from the data in Fig. 13 taken with the diffuser in
the tunnel. However, the general character of the data is essentially
the same as the case without the diffuser. It seems reasonable that
more detailed data would reveal the same unstable behavior.

The base pressure characteristics for the truncated plug nozzle
with no diffuser and with a diffuser are presented in Figs. 14 and 15,
respectively. Figs. 14 and 15 are representative of the ejector-dif-
fuser system operation as opposed to the nozzle operating character-
istics presented in Figs. 12 and 13. Comparison of these two figures
indicates that the base pressure becomes insensitive to changes in
P_{ex}/P_{ol} at a higher overall pressure ratio with the diffuser than with-
out. Also, as in Fig. 13, the value of the "closed wake" base pressure
ratio is about 10% lower with the diffuser present. The data demon-
strates, in addition, that the "open wake" operation is changed with
the diffuser in the tunnel. The value of P_b/P_{ol} for a given P_{ex}/P_{ol}
being lower with the diffuser present. The difference in base pressure
ratio decreases as P_{ex}/P_{ol} is increased. These diffuser effects on
the ejector-diffuser operating characteristics are important in under-
standing the operation of ground test facilities, since most of these

- 8 -

installations employ some type of diffuser.

The effect of the diffuser on the sidewall centerline static pressure is presented in Figs. 16, 17, and 18. Two different "open wake" operating conditions are shown in Figs. 16 and 17 while Fig. 18 is for "closed wake" operation. In all three cases the largest deviation caused by the diffuser is in the far wake (X' greater than about 1 inch). However, there is also a noticeable change in the near wake static pressure distribution in all three cases with the greatest change being on the order of 5%. This variation may account for part of the decrease in base pressure caused by the diffuser.

The process of transition from "open wake" to "closed wake" operation of a truncated plug nozzle is very important for practical considerations. For example, the overall pressure ratio at which the base pressure reaches its minimum value is very important in performance calculations since, once this point is reached, it is then the difference between base and ambient pressure which determines whether the base pressure produces thrust or drag.

Fig. 19 presents a series of schlieren photographs showing the wake "closure" and the ejector-diffuser starting process. The small letters which label the individual pictures correspond to the labeled points on Fig. 12. For completeness the corresponding top contour and sidewall centerline static pressure distributions are presented in Figs. 20 through 25. The photographic sequence in Fig. 19 shows that in general the mechanism of transition from "open" to "closed" wake operation is a complicated process. The exact nature of this process is not well understood and is a function of the geometric and operating parameters of the nozzle.

As mentioned previously the ejector-diffuser starting process is important to the operation of altitude simulation facilities. Figs. 19e and 19f show the final stages of the starting process. In Fig. 19e the wake is "closed" but the system has not reached the starting pressure ratio. This is evidenced by the fact that the free shear layer emanating from the shroud tip is not attached to the duct wall. In Fig. 19f the free shear layer is attached to the duct wall and the system is started with the cell pressure at its minimum value.

Lip Shock

The appearance of the lip shock or separation shock in separated base flow fields has been well documented by Hama (Ref. 3). If the lip shock is of sufficient strength it can have significant effects on the subsequent development of the free shear layer. In addition, it was shown in Ref. 3 that a strong lip shock could alter the recompression shock. In the schlieren photographs in Figs. 19e and 19f the lip shock is very faint. Also, the intersection of the lip shock with the recompression shock does not appear to produce any noticeable deflection of the recompression shock. In addition to the evidence

presented above, in a smoke-streamline (i.e., steady state streakline)
photograph of the flow field (Fig. 26), the streamlines show no measur-
able deflection on passing through the lip shock. The verification
of this smokeline technique for steady flow has recently been documented
at Notre Dame (Ref. 6). These observations, pertaining to lip shock
strength, were found in both the truncated plug nozzle and expansion-
deflection nozzle flow fields. It appears, therefore, that at least
in the cases presented, the lip shock can be neglected in the analysis
without serious effect on the results.

Sonic Line Shape

For the analytical solution it is important to have information
regarding the shape and location of the sonic line (actually a start-
ing line with M>1 is needed for the method of characteristics) with
respect to the throat region of the nozzle. In order to obtain this
data, 10 static pressure taps were drilled in the aluminum sideplate
on and either side of the geometric throat. Fig. 27 shows the loca-
tion of these taps in the throat region of the truncated plug nozzle.

In Fig. 28 the results are presented in the form of an interpo-
lated sonic line. Included in the figure is a tabulation of the Mach
numbers obtained from the static pressure taps. To calculate the Mach
numbers, the measured static pressure was divided by the nozzle total
pressure (atmospheric) which was assumed constant up to the throat.
The Mach numbers were calculated from the resultant pressure ratios
with the use of standard isentropic relations. To obtain points on
the sonic line, linear interpolation was used between known points.
The sonic line points were plotted on a scale drawing (Fig. 28) which
was 4 times actual size, and a curve was then faired through these
points.

Although the interpolated sonic line appears to be quite close
to the geometric throat, there is a noticeable distortion of the shape.
This distortion is undoubtedly due to the fact that the expansion is
centered at the shroud tip and the fact that the converging channel
upstream of the geometric throat is not symmetrical. The combined
effect of these two factors results in a nonuniform expansion of the
flow across the channel. The distortion could also be the result of
interpolation error because of the spacing of the taps.

Turbulence Effects

In connection with the discussion of turbulence effects it would
be instructive to explain some important observations which led to
a change in geometry of the truncated plug nozzle before any of the
data in this report were taken. The nozzle used in this investigation
was designed for an isentropic expansion to Mach 2.0. However, with
the plug in its original design position a series of λ shocks appeared
on the plug upstream of the geometric throat. This indicated that
the flow had become locally supersonic before the minimum area and

was compressing through a system of λ shocks because of the decreasing area. A saw tooth boundary layer trip was then placed on the leading edge of the plug to produce a turbulent boundary layer. The result was that the shocks were replaced with a single strong shock which appeared as a slightly curved normal shock. Following a discussion given by Schlichting (Ref. 7) on boundary layer, shock wave interaction, these observations would indicate that under normal operating conditions the boundary layer was laminar and that with the trip the plug boundary layer became turbulent. The plug was subsequently translated about 0.5 inches downstream and the λ shocks were eliminated.

To determine the effect of turbulence on the centerline static pressure distribution and the base pressure two methods were employed. The first was to put boundary layer trips (saw tooth) on the plug and contour surfaces and the second was to insert a 1/4 inch wire mesh at the inlet to the nozzle section to induce turbulence in the entire flow. The effect of the induced turbulence on the centerline static pressure distribution is shown in Fig. 29. The largest deviation in the near wake resulting from the turbulence appears in the data for the wire mesh where the largest change is on the order of 8%. The boundary layer trip does not appear to have affected the static pressure distribution in the near wake region. The data also seems to indicate a substantial turbulence effect in the far wake. However, the static pressure variation in this region is very sensitive to small changes in exit pressure, and since the data in Fig. 29 is from three separate runs with possible changes in P_{ex}/P_{ol}, it is not possible to draw conclusions from the data in this region.

The variation in the base pressure demonstrated the same trends as did the centerline static pressure distribution in the near wake. With the wire mesh the base pressure was decreased by about 8%, whereas, with the boundary layer trip, the change in base pressure was within the experimental error. These results do not indicate a transition from laminar to turbulent flow in the free shear layer. Since the value of the base pressure is a strong function of the efficiency of the mixing in the shear layer, and since turbulent mixing rates are on the order of ten times greater than laminar mixing rates, a transition from a laminar to a turbulent shear layer would produce a much more drastic change in the base pressure than indicated above. On the basis of these facts it appears that in the undisturbed case the plug boundary layer is laminar and that transition occurs in the free shear layer a very short distance downstream of the corner, whereas in the case with induced turbulence, both the plug boundary layer and free shear layer are turbulent.

Base Bleed

The use of base bleed in truncated plug nozzles has several very important practical applications. It may be used to increase the base pressure under certain operating conditions and also it could be used as a possible means of cooling the plug.

- 11 -

Opaque-stop schlieren photographs of the planar truncated plug nozzle flow field are presented in Fig. 30 for operation with and without base bleed. Fig. 30b is the case for a bleed rate of 1.0% of the primary flow. It is clear from these photographs that even a small bleed rate produces a marked change in the visual flow pattern. The neck of the wake is noticeably thicker and the wake length appears to be slightly longer. Also the lip shock which is bearly visible in the no bleed case has become clearly defined in the flow field with bleed. In addition to the apparent strengthening of the lip shock, its position has been changed. With no bleed it appears to be parallel to the nozzle centerline and rather straight. With base bleed the lip shock becomes curved and divergent from the centerline, intersecting the recompression shock further downstream. Another interesting feature of Fig. 30 is that base bleed has not significantly changed the location or shape of the recompression shock. It does, however, originate at a point further from the nozzle axis due to the widening of the wake.

Fig. 31 shows the effect of base bleed on the nozzle base pressure ratio. The base pressure increases with bleed rate as expected from physical considerations. The rate of increase of P_b/P_{ol} with increasing base bleed becomes quite small when the bleed rate reaches approximately 1%. Also from this figure it can be seen that, for a bleed rate of 1.0%, P_b/P_{ol} increased about 30% above the no bleed value demonstrating the effectiveness of base bleed for base pressure control.

The effect of base bleed on the centerline static pressure is presented in Fig. 32. The peak pressure on the centerline occurs at approximately the same location for the bleed rates shown, however, the magnitude of the peak pressure is substantially reduced. For the data with a base bleed of 1.0% the peak static pressure is reduced by about 18% from the no bleed value. The data of Fig. 32 also show that a short distance after the location of peak pressure all three curves merge and the effect of base bleed seems to be negligible. The downstream pressure rise for the no bleed case appears to be a result of exit pressure setting and not a base bleed effect. More data is needed to clarify this behavior.

DESCRIPTION OF AXISYMMETRIC NOZZLE THRUST FACILITY

The new University of Notre Dame Nozzle Thrust Facility (NTF) was designed to test conventional and unconventional nozzles with up to one square inch throat area and up to 100 pounds thrust. It is a blowdown type apparatus exhausting to the atmosphere. The nozzle total pressure can be varied from 20 psi to 150 psi allowing the testing of nozzles over a wide range of pressure ratios. The basic components of the system shown in Fig. 33 and described in detail below include: air compressor, storage tank, pressure regulator, orifice flow meter, thrust stand assembly, and instrumentation.

Air Compressor

The air compressor, manufactured by the Gardner-Denver Company, is a 10 HP unit which is capable of delivering 22 SCFM at 250 psig. The air passes through an aftercooler and moisture separator having a constant drain. The compressor unit is also equipped with an oil vapor filter charged with activated alumina and an air dryer charged with a silica gel type desicant. The dryer which supplies air at a dew point between $-20^{\circ}F$ and $-40^{\circ}F$ requires approximately three hours of regeneration for each eight hours of pump-up time. Regeneration is accomplished by heating the charge to between 250° and $400^{\circ}F$ thereby driving the moisture from the silica gel. During regeneration a small amount of air is blown from the storage tank through the dryer to purge the moisture-laden air from the unit.

Storage Tank, Pressure Regulator, Orifice Flow Meter

The 50 cu. ft. storage tank is an ASME coded pressure vessel designed for 265 psig at $450^{\circ}F$ maximum and hydrostatically tested as per ASME code, Section VIII. Into one end of the tank a 6-inch schedule 40 pipe was inserted which contains a 200 pound thermal mass for temperature stabilization. The other end of the tank contains a 12 by 16 inch standard ASME code manhole for required inspection. The tank is bolted to two steel "I" beams mounted on the floor and the interior and exterior have been sand blasted and painted with one coat of zinc chromate. Also included with the tank is a 1/2 inch drain valve and a 265 psig. safety valve. Arrangements have been included for the purpose of manifolding two or more tanks together. The flow passes from the storage tank through a gate valve to a two-inch pilot operated regulator which is used to preset the nozzle total pressure prior to each run. Downstream of the regulator is an orifice flow meter permitting mass flow measurement.

Thrust Stand Assembly

The thrust stand arrangement for the Nozzle Thrust Facility is shown in Fig. 33. This assembly rests on a steel plate which is welded to the storage tank. It consists of a stilling chamber which has internal dimensions of 3 inches in diameter by approximately 15 inches in length. This stilling chamber is constructed from a solid block of aluminum. It includes one perforated plate and four 30 mesh screens to straighten the flow before entering the nozzle which is attached to the end of the chamber. Air enters the stilling chamber from both sides through rigidly mounted pipe separated from the stilling chamber by flexible bellows. The bellows allow the stilling chamber to move axially for thrust measurement. Besides the bellows the chamber is attached to the mounting plate by four aluminum bars utilizing eight flexture hinges. A load cell, rated at 100 pounds nominal, is mounted rigidly to the thrust stand and connected to the stilling chamber by means of an aluminum relaxation flexture to minimize transmission of transverse loads. The load cell has been dead weight calibrated.

- 13 -

The results show that hysteresis is maintained to within ± 0.5%.

Instrumentation

The NTF is equipped with a complete set of instrumentation, including storage tank pressure, stilling chamber preset pressure, and stilling chamber total pressure and temperature. The stilling chamber total pressure and temperature are measured downstream of the screens just before the nozzle entrance. Total temperature is measured with an iron constantan thermocouple. The pressure differential across the orifice flow meter is recorded with a Meriam well-type mercury manometer.

Instrumentation will be installed to measure nozzle contour static pressure and temperature when needed and nozzle total pressure profiles. Provisions can also be made to include pressure transducers into the various nozzle-diffuser configurations. The facility has also been designed to include a schlieren system for visual study of the external nozzle flow.

Axisymmetric Truncated Plug Nozzle

An internal-external-expansion plug nozzle was designed for use with the NTF. This nozzle was designed for a Mach number of 1.90 based on the overall area ratio, A_{ex}/A_{nt}. The plug was conical in shape and converged toward the axis at an angle of 10°. The base diameter was 0.250 inches and the length of the plug from the throat was 0.660 inches, which represents a 48% truncated plug. Fig. 34 shows a schematic drawing of the nozzle. The plug is mounted to a webbed centerbody which is mounted to a buffer section. The tubing from the pressure taps in the plug exits from the NTF through this buffer section. The nozzle throat area was 0.33 square inches which permitted a running time of approximately thirty seconds without any loss in stagnation pressure. The shroud contour was cylindrical and extended a distance of 0.30 inches downstream from the throat.

Experimental Procedure

Standard operating procedure for the NTF consisted of first presetting the desired nozzle total pressure with the regulator and then starting the nozzle flow. After allowing several seconds for the pressures in the system to stabilize, the data was recorded. The nozzle total pressure and temperature were read from standard gauges mounted on the NTF control panel. The base pressure was obtained from a 60" well-type mercury manometer. After the pressure data was read, shadowgraph pictures of the nozzle flow field were taken. This was accomplished by turning off all room lights and exposing a sheet of Kodak Royal Pan film with a single flash from a strob light which was mounted behind a pinhole. The pressure data was reduced using standard techniques.

DISCUSSION OF AXISYMMETRIC NOZZLE RESULTS

The operating characteristics of the axisymmetric, internal-external-expansion truncated plug nozzle are shown in Fig. 35. With the exception of the jump in the data between $P_{at}/P_{ol} \simeq 0.35$ and $P_{at}/P_{ol} \simeq 0.31$, these operating characteristics are typical for all altitude compensating nozzles. During "open wake" ($P_{at}/P_{ol} > 0.16$) operation, the base pressure is essentially equal to the ambient pressure (P_{at}) and the base pressure ratio, P_b/P_{ol} decreases as P_{at}/P_{ol} decreases. The trend continues until the jump in the data is approached. After the jump, the same trend is again continued until the wake "closes", after which the base pressure ratio remains constant with further decreases in P_{at}/P_{ol}.

A possible explanation for the jump in the data at $P_{at}/P_{ol} \simeq 0.35$ can be obtained from Fig. 36. This figure presents a series of shadowgraphs showing the development of the nozzle flow field. The letters identifying the photographs in Fig. 36 correspond to the labeled points in Fig. 35. The jump in the data occurs between Figs. 36b and 36c. In Fig. 36b, the oblique shock which is reflected from the plug surface intersects the free shear layer originating from the shroud tip and is reflected as an expansion which intersects the plug surface a short distance upstream of the base. In Fig. 36c, this reflected expansion does not intersect the plug but instead intersects the free shear layer downstream of the plug base. Apparently this expansion, shown in Fig. 36, accelerates the flow upstream of the base which results in a reduced base pressure as indicated in Fig. 35. Initially the base pressure ratio decreases at the same rate as P_{at}/P_{ol}. As the jump is approached, the upstream acceleration of the flow from the reflected expansion causes P_b/P_{ol} to decrease more rapidly than P_{at}/P_{ol}. Once the reflected expansion has moved downstream of the plug base as in Fig. 36c, the Mach number approaching the base would be lower resulting in a higher base pressure and thus producing the jump shown in Fig. 35. The axisymmetric data presented here is only preliminary and further investigations are necessary for deeper insight into the flow phenomena involved.

ANALYTICAL PHASE

An analytical treatment of plug nozzle flows must contain all of the important flow components and allow for their interaction with each other. The total solution revolves around the analysis of the viscous near wake or base region within the almost inviscid external nozzle flow. Therefore, a near wake analysis which predicts the base pressure and shape of the near wake is necessary.

There have been several published attempts to calculate the pressure on an axisymmetric base in turbulent flow. A recent review of the pertinent base pressure techniques is given in Ref. 8. Almost all of these methods assume a uniform external flow approaching the base. It is apparent at the outset that, in the case of the plug nozzle flow field, the base region is enclosed in a nonuniform external flow field. Therefore, only a method which includes a complete calculation of the inviscid flow field adjacent to the base region will be able to handle the nonuniform plug nozzle case. The method used here is a further extension of the work of Mueller and Hall (Ref. 9).

Two types of plug nozzles were considered in this investigation. The expansion-deflection nozzle shown in Fig. 37a has the plug completely enclosed by the nozzle shroud. In Fig. 37b, the truncated plug nozzle configuration is shown in which the plug extends beyond the nozzle contour. For both nozzle configurations, the methods of solution are for the "closed" wake condition and are similar (although the boundary conditions are somewhat different). Once supersonic flow has been established, i.e., M > 1, the governing equation for the inviscid flow becomes hyperbolic permitting a solution by a method of characteristics. The flow between the near wake and the external jet boundary emanating from the shroud is assumed to be inviscid, although it may be rotational. The recompression shock, for example, may produce an entropy gradient from streamline to streamline. Entropy gradients from any other source are not allowed. This rules out the use of the characteristics in a boundary layer, even though only the supersonic portion may be considered. The nozzle flow has been assumed to exhaust into a region in which the pressure remains constant. This corresponds to a nozzle exhausting into still air. Since the method of characteristics results from a hyperbolic partial differential equation, only the initial conditions and boundary conditions need to be specified. The solution proceeds downstream, and portions of the flow field which have already been determined cannot be affected by conditions downstream. However, a shock wave may intersect regions of characteristics which have been calculated.

The base pressure solution determines the lower boundary condition for the method of characteristics solution above the near wake. On the other hand, the method of characteristics provides the boundary conditions for the near wake analysis. The base pressure solution described below is iterative. Since this solution does provide a boundary condition for the method of characteristics, in effect, the

- 16 -

solution to the whole nozzle flow field after separation becomes iterative.

The shape of the base flow region downstream of the plug is determined by employing an extension of the flow model developed by Zumwalt (Refs. 10 & 11) and later modified by Mueller (Ref. 13 & 14). In addition to obtaining the plug base pressure, the general features of the entire nozzle flow field are obtained.

BASIC FLOW MODEL

The theoretical flow model used in conjunction with the restricted mixing theory of Korst (Ref. 14) and the rotational method of characteristics is shown in Fig. 38. An unrestricted mixing theory was developed to include the initial boundary layer. A complete derivation of the governing equations is presented in Appendix I and II. In this flow model, the flow is divided into three major components:

1. an inviscid free stream
2. a dissipative mixing layer, and
3. a base region.

In addition to using the restricted mixing theory of Korst, the following conditions are imposed on these three flow components:

a) The initial condition in the throat of the nozzle may be either along a left-running characteristic (as in an E-D nozzle), along a right-running characteristic (as in a T-P nozzle), or along a non-characteristic line. The flow need not be uniform at this initial condition line, but must be supersonic. The external nozzle flow is calculated using rotational characteristics.

b) The boundary layer approaching the separation corner is neglected, although fully turbulent mixing is assumed.

c) An isentropic expansion takes place in the free stream from 1 to 2, i.e., a continuation of the method of characteristics for the flow over the plug. The effect of a lip shock is ignored in this analysis.

d) The inviscid flow past a conetail using the rotational method of characteristics is utilized to define the pressure field impressed on the mixing region from (2) to (3). This conetail surface also serves as the "corresponding inviscid jet boundary".

e) The pressure normal to the "corresponding inviscid jet boundary" is assumed to be constant within and near the mixing region at each cross section.

- 17 -

f) Velocity profile similarity is assumed in the mixing region. The error function velocity distribution is located within the intrinsic coordinates x, y, and is represented by $X \simeq x$ and $Y = y - y_m(x)$ where $y_m(0) = 0$. This coordinate shift is a consequence of using the restricted mixing theory of Korst.

g) The geometry of the mixing region is taken into account in the integral representation for momentum and mass flux between (2) and (3).

h) Recompression is assumed to result from an oblique shock turn from (3) to (4) at an empiracally determined trailing wake radius ratio. (Ref. 15).

A streamline, j, can be identified which divides the amount of mass passing over the corner at (1) from that mass flow entrained by the viscous action of the free jet mixing region. A second streamline, d, can be identified which has just sufficient kinetic energy at (3) to negotiate the pressure rise to (4). Streamlines below the d-streamline have lower kinetic energies and cannot pass through recompression, and are turned back to recirculate in the base region. If there is no base bleed, conservation of mass requires that the j- and the d-streamlines be identical. Korst distinguished between these two streamlines, and pictured the space between them as a sort of corridor through which mass could flow into or out of the base region.

The control volume between cross sections (2) and (3) is bounded by streamlines R and -R as shown in Fig. 38. The streamlines, R and -R, were defined by Zumwalt such that the cross sectional area normal to the direction of flow would remain nearly constant, and the PdA pressure force could be neglected in the momentum equation. For the simplified axisymmetric flow field described above, Zumwalt formulated the momentum equation in the axial direction using geometrical relations and the relation between the viscous and inviscid coordinate systems. This equation was solved simultaneously with the combined viscous and inviscid continuity equations written for the control volume between cross sections (2) and (3). For the error function velocity profile $\phi = \frac{1}{2}(1 + \mathrm{erf}\,\eta)$. Where $\phi = u/u_a$ and $\eta = \sigma y/x$, it was found that $\eta_R = 3$ was large enough for ϕ_j to approach its asymptotic value. The result of this analysis is a nonlinear equation which allows one to locate the j-streamline at cross section (3), namely:

$$\left\{ (B-3)^2 + 2(1-C_{3a}^2) \left[I_1 \Big|_{-\infty}^{3} - I_1 \Big|_{-\infty}^{\eta j} \right] B - 2(1-C_{3a}^2) \left[J_1 \Big|_{-\infty}^{3} - J_1 \Big|_{-\infty}^{\eta j} \right] \right\}_{3a} = \left(\frac{\overline{\sigma r}}{x\cos\theta} \right)_{3a} \tag{1}$$

where the integral limits refers to η values, and:

$$B = \frac{J_1 \Big|_{-\infty}^{\eta j} - \left[1 - (C_{3a}/C_{2a})\right] J_1 \Big|_{-\infty}^{3} - (C_{3a}/C_{2a})(J_1 - J_2)\Big|_{-\infty}^{3}}{I_1 \Big|_{-\infty}^{\eta j} - \left[1 - (C_{3a}/C_{2a})\right] I_1 \Big|_{-\infty}^{3} \ (C_{3a}/C_{2a})(I_1 - I_2)\Big|_{-\infty}^{3} + \left[(\gamma-1)/\gamma\right](3/C_{2a}C_{3a})\left[1 - (P_2/P_3)\right]} \tag{2}$$

where:

$$I_1 = \int_{-\infty}^{\eta} \frac{\phi d\eta}{1-c_{3a}^2 \phi^2} \tag{3}$$

$$I_2 = \int_{-\infty}^{\eta} \frac{\phi^2 d\eta}{1-c_{3a}^2 \phi^2} \tag{4}$$

$$J_1 = \int_{-\infty}^{\eta} \frac{\phi \eta d\eta}{1-c_{3a}^2 \phi^2} \tag{5}$$

$$J_2 = \int_{-\infty}^{\eta} \frac{\phi^2 \eta d\eta}{1-c_{3a}^2 \phi^2} \tag{6}$$

It should be noted that since these integrals are expressed only in terms of Crocco number, C, they are independent of the ratio of specific heats, γ, although Equation 1 is a function of γ.

It is evident that, in order to determine ϕ_{j3} from Equations 1 and 2 for a given initial condition, the location of the recompression, $\bar{r}_3/r_b$, the corresponding inviscid condition M_{3a}, and the jet spread parameter, σ_{3a}, must be known. The location of the recompression point, $\bar{r}_3/r_b$, is determined from experimental data. The Mach number along the inviscid jet boundary at (3), M_{3a}, is determined from the axisymmetric rotational method of characteristics solution. The jet spread parameter is determined from the equation given by Channapragada (Ref. 16):

$$\sigma_{3a} = \{R'[1+\beta(1-c_{3a}^2)]\}^{-1} \sigma_{inc} \tag{7}$$

where $\sigma_{inc} = 12.0$ for the error function velocity profile, $\beta = T_{o1}/T_b$ ($\beta = 1.0$ for isoenergetic mixing considered here), and R' is the empirical compressible divergence factor defined by Channapragada as a function of the Crocco number.

The geometric parameter, $(\frac{\sigma \bar{r}}{x \cos \theta})_{3a}^2$, may be calculated since $\theta_{3-4} = \theta_{1-2}$ from the conical wake assumption, and since:

$$\left[\frac{\sigma \bar{r}}{x\cos\theta}\right]_{3a}^2 = \left[\frac{\sigma \tan\theta}{1/(\bar{r}/r_b)-1}\right]_{3a}^2 \tag{8}$$

At this point, $\phi_{j3} = \phi_{d3}$ (i.e., no base bleed) may be obtained from Equations 1 and 2. Therefore, $C_{d3} = \phi_{d3}C_{3a}$ for isoenergetic flow. However, the value of C_{d3} may also be obtained from the assumed isentropic recompression mechanism along the d-streamline (i.e., $P_{od3} = P_4$ from

$$C_{d3} = \left[1 - (P_4/P_3)^{-\frac{\gamma-1}{\gamma}}\right]^{\frac{1}{2}} \tag{9}$$

where P_4/P_3 is the static pressure rise across the two-dimensional oblique shock which results from the turning of the flow with Mach number M_{3a} through the angle θ_{3-4}. When the two values of C_{d3} are equal, then the assumed base pressure ratio is correct for the prescribed initial conditions and nozzle geometry. A typical solution curve is shown in Fig. 39. The values of C_{d3} resulting from the above equations are subtracted from each other such that the solution always occurs at zero.

As mentioned above, the method of characteristics is used to solve the supersonic inviscid (and possibly rotational) portion of the plug nozzle flow field. Fig. 37 shows the extent of this part of the nozzle flow field as applied to the expansion-deflection and truncated plug nozzles. In both configurations, the characteristics solution begins at the initial characteristic line, and may extend beyond the recompression shock. The upper boundary is the nozzle shroud contour (E-D nozzle) or a constant pressure boundary with a pressure equal to the outside (or ambient) pressure. The lower portion of the flow fields terminate on the plug contour, the "corresponding inviscid jet boundary", and finally, the trailing far wake. The trailing wake boundary corresponds to a cylindrical wake with zero streamline angle at its outer edge.

The actual calculation procedure for the method of characteristics is generally straightforward, but the interior flow field points and the boundary points must be distinguished. For an interior point, two upstream points combine to determine the location and conditions at a third point further downstream. This is shown schematically in Fig. 40a. The right-running characteristic from point 1 and the left-running characteristic from point 2 intersect, thus locating point 3 in the flow field. Then the additional variables (streamline angle, Mach number, and entropy) are determined iteratively.

For a solid surface (Fig. 40b), point 1 and the physical boundary combine to locate point 3. The intersection of the right-running characteristic from point 1 and the surface locate the new point. On a prescribed solid surface, the streamline angle is known (or may easily be calculated from the geometry). Thus, it is necessary to iterate

only the Mach number at that point. It should also be noted that, since the solid boundary corresponds to a streamline, the entropy at point 3 is the same as that at any other upstream point on the body surface.

The third type of boundary condition is that of a constant pressure boundary (Fig. 40c). For no shock wave intersections, this implies a constant Mach number on this type of surface. Locating point 3 and determining the flow properties, except entropy, becomes iterative. A first estimate is made on the location by a linear extrapolation from the previous boundary point. The location is then modified accordingly by appropriate averaging of the streamline angles.

The method of characteristics may also be used to locate an oblique shock within the flow field. A characteristic is an infinitesimally weak wave. A shock, on the other hand, may be regarded as a "piling up" of characteristic waves resulting in a coalesced wave which can no longer be regarded as weak. This is illustrated schematically in Fig. 41a. The solution across a shock wave is not hyperbolic, and cannot be treated directly by the method of characteristics. Constructing a shock wave in a characteristic regime becomes an iterative process. Upstream of a shock wave, conditions are known from the method of characteristics. Although the method of characteristics solution is not valid through a shock wave, the characteristics may be continued again downstream of the shock wave. Behind a shock, the left-running waves from a point are always steeper than the shock resulting in further intersections of the characteristic and the shock (see Fig. 41a). Thus conditions are available on the downstream side of the shock wave. The shock wave cubic equation (Ref. 17) provides a supplemental solution across a shock wave which has as its independent variable, the shock wave angle. Thus, when the values of streamline angle and Mach number behind the shock obtained from the characteristics downstream of the shock, and the same variables obtained from the shock wave cubic equation agree, then the shock wave angle is correct for that point. This situation is illustrated in Fig. 41b. It should be noted that the conditions upstream of the shock remain unchanged.

The method of characteristics solution begins near the throat region where the flow is supersonic. This solution is not applicable to subsonic or sonic flows. A complete derivation of a general method of characteristics solution and a derivation of the axisymmetric method of characteristics (rotational) is presented in Appendix I.

EXTENSIONS TO BASIC FLOW MODEL

In order to cover a more complete scope of the parameters involved in studying plug nozzle flow fields, certain extensions of the basic flow model must be made. These include the effects of non-isoenergetic mixing, base bleed, and initial turbulent boundary layers.

Non-Isoenergetic Mixing

The value of $T_b/T_{ol} = 1$ represents the isoenergetic mixing solution, while values not equal to unity imply non-isoenergetic mixing. Non-isoenergetic mixing, therefore, means that the stagnation temperature in the base region differs from that of the adjacent inviscid flow, i.e.:

$$\Lambda = T_{ob}/T_{ol} \neq 1 \tag{10}$$

or in terms of the actual base temperature and velocity ratio, this becomes:

$$\Lambda = \frac{T_b}{T_{ol}} + (1 - \frac{T_b}{T_o})\phi \tag{11}$$

The base pressure solution for non-isoenergetic mixing requires two modifications in the equations described in the previous section. The first concerns the integrals I_1, I_2, J_1, and J_2 which are found in the lengthy integral equation used in locating the j-streamline (Equation 1). These integrals (Equations 3-6) now become (Ref. 18):

$$I_1 = \int_{-\infty}^{\eta} \frac{\phi\, d\eta}{\Lambda - c_{3a}^2 \phi^2} = \int_{-\infty}^{\eta} \frac{\phi\, d\eta}{\phi + T_b/T_{ol}(1-\phi) - c_{3a}^2 \phi^2} \tag{12}$$

$$I_2 = \int_{-\infty}^{\eta} \frac{\phi^2\, d\eta}{\Lambda - c_{3a}^2 \phi^2} = \int_{-\infty}^{\eta} \frac{\phi^2\, d\eta}{\phi + T_b/T_{ol}(1-\phi) - c_{3a}^2 \phi^2} \tag{13}$$

$$J_1 = \int_{-\infty}^{\eta} \frac{\phi\eta\, d\eta}{\Lambda - c_{3a}^2 \phi^2} = \int_{-\infty}^{\eta} \frac{\phi\eta\, d\eta}{\phi + T_b/T_{ol}(1-\phi) - c_{3a}^2 \phi^2} \tag{14}$$

$$J_2 = \int_{-\infty}^{\eta} \frac{\phi^2\eta\, d\eta}{\Lambda - c_{3a}^2 \phi^2} = \int_{-\infty}^{\eta} \frac{\phi^2\eta\, d\eta}{\phi + T_b/T_{ol}(1-\phi) - c_{3a}^2 \phi^2} \tag{15}$$

The temperature ratio originally arises from the density ratio term normal to the mixing region (see Appendix II). It should be noted that for isoenergetic mixing, $T_{ob}/T_{ol} = T_b/T_{ol} = 1$, then Equations 12-15 again are identical to Equations 3-6.

The second change required in discussing non-isoenergetic mixing is that of calculating the Crocco number on the d-streamline. The

expression for C_{d3} now becomes:

$$C_{d3} = \frac{C_{3a}\phi_{j3}}{\left[\frac{T_b}{T_{01}} + (1-\frac{T_b}{T_{01}})\phi_{j3}\right]^{\frac{1}{2}}}$$ (16)

This value of C_{d3} is then compared with that obtained from Equation 9, and when these two values agree, then the assumed base pressure ratio is correct.

Base Bleed

In discussing base flows in which base bleed (i.e., mass addition) is present, modifications of the original flow model must be made. These additional assumptions include:

a) The amount of mass addition is small
b) The momentum associated with this mass addition is negligible
c) For steady mass bleed cases, some amount of mass will be pumped into or out of the base region through the mixing region between the j- and d-streamlines.

The analysis of base bleed is that of Zumwalt and Tang, (Ref. 11), and a brief outline of the governing equations is presented below. Their analysis is valid for an axisymmetric flow, and is an extension of the planar flow model developed by Korst, et al (Ref. 14). For planar flows, the techniques described in Ref. 14 were used, but are not repeated in this report.

In terms of the locations of the j- and d-streamlines for axisymmetric configurations, the mass flow between them may be expressed as:

$$G_d = \frac{\pi r^2}{4} \frac{K P_{01} \cot\theta}{\sigma_{3a}^2 \sqrt{T_0} \sin\theta} (1 - \frac{r_w}{r_b})^2 \left[(J_{1d} - J_{1j}) - B(I_{1d} - I_{1j})\right] 3a$$ (17)

where the integrals I_1 and J_1 refer to the integrals described by Equations 12 and 14. The additional subscript refers to the specific values of η in the upper limit of the integrals. The value of B is determined from Equation 2, and)K is defined as:

$$K = \frac{8 (\frac{2}{\gamma+1})^{\frac{\gamma+1}{2(\gamma-1)}} (1-C_{3a}^2)}{(A_{3a}/A_{nt})\sqrt{\frac{R}{g\gamma}}}$$ (18)

A non-dimensional bleed number, H, may also be defined which relates the amount of bleed to the adjacent flow stagnation conditions:

$$H \equiv \frac{G_d T_{01}}{A_b P_{01}} \sqrt{\frac{R}{g\gamma}}$$ (19)

- 23 -

where A_b is the base area of the plug. Therefore, Equation 19 becomes:

$$\mathcal{H} = \frac{\sqrt{\frac{R}{g\gamma}}\,\mathcal{K}\mathrm{Cot}\theta}{4\sigma_{3a}^2\,\mathrm{Sin}\theta}\left(1-\frac{r_w}{r_b}\right)^2\left[(J_{1d}-J_{1j})-B(I_{1d}-I_{1j})\right]_{3a} \qquad (20)$$

This equation, incidentally, was incorrect in Ref. 11; the integer "4" was missing in the denominator.

Conservation of mass requires that the known mass bleed through the base equal that mass which is entering or exiting between the j- and d-streamlines in the mixing region. Thus, when this condition is achieved (the non-dimensional bleed numbers being identical in magnitude, but opposite in sign), the assumed base pressure ratio is the correct one corresponding to that bleed rate. That is, a solution is reached when:

$$\mathcal{H}/\mathcal{H}' = -1.00 \qquad (21)$$

where $\mathcal{H}'$ is the mass bleed rate through the plug base. The minus sign in this solution shows direction, i.e., mass flow into the base region is positive in sign, while flow out of the base region is negative.

The solution curve for nozzles with base bleed differs from the solution curve of the no-bleed case shown in Fig. 39. Fig. 42 shows a typical solution curve for a nozzle with base bleed into the near wake region. It is noted that this curve has the general shape of a hyperbola with one asymptote at $\mathcal{H}/\mathcal{H}' = +1.00$. The second asymptote is located at the value of the base pressure for which there is no base bleed, i.e., the d-streamline is identical to the j-streamline. For increased bleed rates, the curve "flattens out", thus raising the solution to a higher value of the base pressure ratio. For planar base bleed flows, the solution curve shown in Fig. 42 is "well-behaved" in that the general hyperbolic shape is preserved at all values of the base pressure. However, with axisymmetric configurations, the solution curve may become quite erratic at values of the base pressure not in the vicinity of the solution. Near the solution, the curve does maintain its general hyperbolic shape. This instability is a result of the coupled effects of the nonuniform flow, the variation of the wake radius ratio, and the value of the Mach number at recompression. The value of B described by Equation 2, appears to control this variation of the curve from the norm.

Initial Boundary Layer

In any moving viscous fluid, a boundary layer is present along a solid surface. In plug nozzles the turbulent boundary layer on the plug upstream of separation may have a very significant effect on the remainder of the flow field. In particular, the near wake base pressure solution is affected. One technique for handling such an initial boundary layer is to treat this situation as an equivalent base bleed,

(Refs. 18, 19, 20) To justify this approach, the flow model used in this analysis must be considered. The j-streamline in the mixing solution separates the fluid which originally passes over the plug from that fluid entrained from the near wake. The d-streamline becomes displaced from the j-streamline by a distance which is a direct function of the mass bleed rate. (For no mass bleed, the j- and the d-streamlines are coincident). This separation of the j- and d-streamlines results in a shift of the velocity profile in the near wake region. The existence of a finite boundary layer at the plug tip also produces a shift in the velocity profile in this region. Both the boundary layer and the base bleed may be combined into a "displacement parameter", (Ref. 18), whereby the effect of an initial turbulent boundary layer on the mixing profile is identical to that of base bleed. The actual amount of equivalent base bleed due to the finite boundary layer, $\dot{m}_{BL}$, may be expressed as:

$$\dot{m}_{BL} = 2 \, \rho_1 u_1 \quad \delta^{**} (\pi r_{BL})^{\epsilon} \tag{22}$$

where ρ_1 is the density of the flow immediately adjacent to the boundary layer. For this flow u_1 is the velocity, and δ^{**} is the momentum thickness of the boundary layer; r_{BL} is the average radius of the boundary layer, while $\epsilon = 0$ for planar flow and $\epsilon = 1$ for axisymmetric configurations. It should be noted that the coefficent 2 is present for both axisymmetric and planar geometries. In planar flow a boundary layer occurs on both sides of the plug; for axisymmetric flows the coefficient is then incorporated into the circumference term.

In this analysis, the approaching boundary layer profile has been assumed to take the form of a power law profile, i.e.:

$$u/u_1 = (y/\delta)^{1/n} \tag{23}$$

where $1/n$ is the power law profile exponent. The value of n may be chosen, and need not be restricted to any particular value (e.g., seven). This method was employed because the exponent is a function of Reynolds number and the nozzle geometry (Ref. 21). For two nozzles which are geometrically similar, but differ in size, the velocity profile exponent may vary somewhat.

EMPIRICAL INPUTS

Although the analysis used in this report does have a strong theoretical foundation, empirical or semi-empirical inputs are still required. A lack of knowledge and understanding of certain facets of the flow necessitate these inputs. These include, for example, the mechanism of recompression and the concept of turbulent mixing. Other inputs may be significant when considering the accuracy of a solution. The number of characteristic points in a flow field is an example of this type of input. These inputs are described in the sections below.

Jet Spread Parameter

In order to use the analysis developed by Mueller (Ref. 13), it is necessary to specify the jet spread parameter, σ_{3a}, which describes the rate at which the width of the shear layer is changing in the stream-wise direction. This jet spread parameter has been investigated by many authors and is generally based on empirical or semi-empirical formulations. Throughout this analysis, the jet spread parameter obtained by Channapragada (i.e., Equation 7) was used for axisymmetric flows. For planar flows, the formulation of the jet spread parameter of Korst (Ref. 14) was employed, namely:

$$\sigma = 12.0 + 2.758M \qquad (24)$$

Wake Radius Ratio

Another empirical variable which must be incorporated into the near wake solution is the wake radius ratio, r_w/r_b. This locates the point in the flow field at which recompression is assumed to occur. A study was made to determine the sensitivity of the base pressure to this parameter. Fig. 43 shows the plot of the results of this investigation. The curve shown here is for an axisymmetric expansion-deflection nozzle ($A_{ex}/A_{nt} = 5.602$, $A_b/A_{nt} = 2.448$).

Zumwalt (Ref. 10) assumed that the base pressure for cylindrical bodies in a uniform flow should increase with decreasing wake radius ratio until a value of approximately $r_w/r_b = 0.50$. He compared the wake radius to a solid sting support, and then assumed that as the sting radius approaches zero, the base pressure would remain constant. He further stated that below a wake radius ratio of about 0.50, the base pressure experienced little change. At wake radius ratios less than that at the peak of the curve, a large divergence in the base pressure occurs between Zumwalt's assumption and the actual calculated base pressure. This large difference in the base pressure results from the analytic solution which "forces" the flow to recompress at the particular wake radius ratio. In the physical flow, merely decreasing a solid sting radius does not insure that recompression will occur at that decreased radius. The actual wake radius ratio does, however, occur in the vicinity of the peak of the base pressure curve (Ref. 12) in Fig. 43.

From the shape of the curve in Fig. 43, it is apparent that the solution of the near wake is sensitive to this empirical parameter. Zumwalt and Tang (Ref. 11) have proposed a base bleed flow model which takes into account the variation of the wake radius ratio with the nondimensional bleed number, $\mathcal{H}$. However, due to an algebraic error, their formulation of the wake radius ratio results in values which are too large. The actual wake radius ratio, r_w/r_b, may be related to Zumwalt and Tang's value, $(r_w/r_b)_{ZT}$, by:

$$r_w/r_b = 2(r_w/r_b)_{ZT} - 1.0 \qquad (25)$$

This result was obtained from an algebraic manipulation of the correct and incorrect version of Equation 20. All values of the integrals, Crocco number, and jet spread parameter were assumed identical in both equations. For the no-bleed case their assumed value of the wake radius ratio of approximately 0.67 should be about 0.34 instead. This latter value of the wake radius ratio, in addition to being consistent with the flow model, appears to be much closer to the observed values measured from schlieren photographs.

The base pressure trends with base bleed shown in Ref. 11 appear correct. However, the actual numerical values of the wake radius ratio with base bleed are incorrect. This occurs because the Mach number at recompression, M_{3a}, is determined semi-empirically from available method of characteristics solutions, and is a strong function of the wake radius ratio, i.e.:

$$M_{3a} = M_{2a}e^{-0.209(1 - r_w/r_b)} \qquad \text{(for } \gamma = 1.40) \qquad (26)$$

The base pressure solution, in turn, is highly dependent upon this value of M_{3a}.

These authors (Ref. 11) argue that the wake radius ratio versus $\mathcal{H}$ curve may be valid over a large range of Mach numbers, because of the appropriate non-dimensionalization of the base bleed rate. This concept for no base bleed has been retained, i.e., $r_w/r_b = 0.350$ for all axisymmetric expansion-deflection nozzle configurations. It should be noted that the validity of this premise may be questionable for highly nonuniform flows and/or for large plug angles. A justification for retaining this concept for all nozzle configurations is demonstrated in Fig. 44. This figure shows the pressure variation along the "corresponding inviscid jet boundary". A Mach number increase is noted immediately downstream of separation followed by a region of rising pressure (Mach number decrease). For the curve corresponding to zero base bleed, recompression occurs at a wake radius ratio of 0.350. This results in an additional pressure rise across the recompression shock. For the curve in which base bleed is present, the solution was extended so that recompression also occurred at a wake radius ratio of 0.350. For this curve the pressure again decreases immediately after separation and then begins to rise. At about the same axial distance from the base that recompression occurred for the no-bleed case, the pressures and corresponding Mach numbers for the two cases shown appear relatively close. Slightly downstream from this location, however, the Mach number again begins to increase. This results in a corresponding pressure drop. In fact, the pressure falls below the base pressure, indicating that $M_{3a}/M_{2a} > 1$. A pressure rise then takes place again as the flow passes through the recompression shock. This particular analytical phenomenon (i.e., the Mach number increase after the pressure rise) is not encountered experimentally, (Refs. 12 & 22). Therefore, a modified wake radius ratio at recompression must be incorporated.

It is noted experimentally for non-zero bleed rates that the wake radius ratio increases noticeably with increasing bleed. In this case the recompression point is shifted downstream. Fig. 30 illustrates this situation for a planar truncated plug nozzle. In Fig. 30a there is no base bleed, while in Fig. 30b mass is emanating from the plug base ($\mathcal{H}$ = 0.0120). As may readily be observed, the base bleed increases the wake radius at recompression (assumed to be r_w), and the axial point at which recompression occurs has shifted slightly downstream. The most interesting feature of these photographs is the shape of the recompression shock above the recompression point. In this region the shock shapes for both cases nearly coincide. Although, admittedly, this observation is based on a limited amount of experimental data, a formulation of an empirical wake radius ratio was made on this basis.

A solution is first obtained for the no-bleed case, and a line is constructed perpendicular to the "corresponding inviscid jet boundary" at the recompression point. The intersection of this line and a new "corresponding inviscid jet boundary" obtained from a different base pressure establishes a wake radius ratio. This is illustrated in Fig. 45. This new wake radius ratio is then a function of the change in base pressure due to base bleed. This formulation has the feature that both the increase in the wake radius ratio and the movement of the recompression points are retained for a given base bleed rate.

Recompression Coefficient

One of the more controversial empirical constants which has been used by some authors in the base pressure near wake solution is the recompression coefficient, N. In the original analysis by Korst (Ref. 14) and Zumwalt (Ref. 10), recompression was assumed to occur at the peak pressure. Nash (Ref. 23) stated, however, that recompression along the dividing streamline would occur at only a fraction of this peak pressure. In this case, rather significant changes in the base pressure solution would occur. Fig. 46 demonstrates the effect that the recompression coefficient has on the calculated base pressure. The nozzle used in this investigation is a planar expansion-deflection nozzle with A_{ex}/A_{nt} = 2.007 and A_b/A_{nt} = 0.833. A considerable decrease in the base pressure occurs as the recompression coefficient decreases from unity. For example, the base pressure ratio decreases from 0.1482 when N = 1.00 to a value of 0.0865 at N = 0.670, a decrease in the base pressure of 41%.

It can be argued (Ref. 24) that the use of the recompression coefficient may be unnecessary since the flow model itself is only an approximation (and definitely a simplification) of the actual mixing mechanism. Cancellation of errors often results due to some of the assumptions (e.g., isentropic recompression along the dividing streamline, and zero pressure gradient in the y-direction). Much data supports the use of a recompression coefficient, and an even greater amount shows that it is unnecessary. Should the use of the recompression coefficient

be unnecessary, the situation would be improved, for the reliance on another empirical parameter would be eliminated. In all subsequent calculations in this report, the recompression coefficient has been assumed to be unity, i.e., recompression occurs at the peak pressure downstream of the recompression shock.

Mesh Size Comparison

The ability to obtain a rapid, yet accurate, solution of a pre-scribed flow field was of primary concern. Therefore, a study was made to determine the effect of varying the initial characteristic grid spacing. Results of this comparison are shown in Fig. 47. Fig. 47a shows the flow field of a planar expansion-deflection nozzle whose flow field was calculated with 20 characteristic grid points in the vertical direction. Fig. 46b shows the same nozzle configuration, except that the number of vertical grid points used in this case was 40. A visual comparison of these two flow fields shows negligible changes in the streamline shapes. The recompression shock in both figures does, how-ever, show a very slight deviation. Numerical comparisons of common points within the flow field also demonstrate good agreement. For ex-ample, the Mach number just upstream of the recompression shock along the "corresponding inviscid jet boundary" is 1.9084 in the 20-grid sys-tem, while it is 1.9027 in the 40-grid spacing system. The percent difference in the Mach number at this point is less than 0.3%. Other comparisons made throughout the flow field indicate less than 1 per-cent difference for all variables.

Because of these minimal differences in the flow field variables, confidence was placed in the results obtained using a lower number of characteristic grid points in the vertical direction. In most configu-rations which were investigated, a nominal value of 32 grid spacings were used. This provided sufficient accuracy in the calculation of all variables, and permitted reasonably rapid computer execution times. It should be noted that a maximum number of 40 points to a minimum of 20 points could be used. The upper limit was established by the stor-age limitations of the computer, while the lower limit was prescribed to permit accurate solutions in the vicinity of sharp corners (e.g., the plug tip and the shroud contour exit).

DISCUSSION OF ANALYTICAL RESULTS

A complete study of the parameters involved in plug nozzle con-figurations could easily approach momentous proportions. From a pure-ly geometrical standpoint, there are an infinite number of plug nozzle geometries. It was necessary to limit most of the parameters to one or two nozzle configurations operating in the same environment. The numerical values of the results which were obtained should not be re-garded as absolute for all nozzles of the same configuration. Instead, trends should be evaluated as one parameter is varied.

Initial Throat Conditions

The method of characteristics solution cannot compute the subsonic or sonic portions of plug nozzle flow fields. Therefore, a supersonic starting line must be determined which forms the initial boundary conditions for the method of characteristics. The characteristics downstream of this line may vary considerably depending upon the initial line's shape and the variation of the flow properties along it. Since the base pressure solution is a direct function of the method of characteristics solution, the base pressure cannot remain unaffected by changes in the shape of the sonic line.

Fig. 48 pictures the calculated flow fields of a hypothetical axisymmetric internal-external-expansion nozzle (A_{ex}/A_{nt} = 9.2571, and A_b/A_{nt} = 2.8571). The only variable in these figures is the shape of the sonic line. Fig. 48a was obtained with "uniform" initial conditions. At x/r_p = 0, the Mach number was assumed to be 1.050, and the initial line was vertical. The streamline angle varied linearly from -7.97° on the plug surface to 0° on the shroud contour surface. The base pressure ratio, P_b/P_{ol}, for this initial condition was 0.005144.

Fig. 48b shows the same nozzle configuration using a parabolic initial profile. The plot of the flow field shows a negligible change from the uniform profile initial conditions. The initial Mach number for the parabolic profile was 1.050, and the streamline angle varied linearly as in the previous case. The two end points of the initial line (the plug point and the shroud contour point) again have their locations at x/r_p = 0. The center point, however, is located at an axial distance of x/r_p = 0.010. It should be noted that the total height of the initial line at x/r_p = 0 is 0.100. The base pressure ratio for the parabolic initial profile is P_b/P_{ol} = 0.005124. At least for this nozzle configuration with the parabolic starting line described above, only a small change in the base pressure is noted.

The effects of a linear profile are presented in the flow field shown in Fig. 48c. The starting Mach number was again 1.050, and the streamline angle varied linearly between end points. The lower end point on the plug was located at x/r_p = 0, while the upper end point was positioned at x/r_p = 0.020. The base pressure ratio for this case has dropped significantly. Its value is now P_b/P_{ol} = 0.004382, a decrease of almost 15% in the base pressure from the uniform case. However, the actual changes in the flow field adjacent to the near wake region appear small despite the rather large change in the base pressure. Recompression is moved slightly upstream due to the change in the base pressure, but the streamline patterns indicate that the remainder of the flow field appears almost unchanged. In addition, the recompression shock shapes do not vary appreciably.

The final shape which was investigated was the circular arc initial profile. The initial Mach number and streamline angles were determined as in the previous cases. A starting line was constructed

such that an arc was perpendicular to both the plug surface and the shroud contour surface. This initial profile produced the flow field shown in Fig. 48d. Again the flow field external to the near wake region remains relatively unchanged from the previous cases. The base pressure for this starting condition shows an increase over the uniform profile condition of Fig. 48a. For this case, $P_b/P_{ol} = 0.005673$.
In all cases described above the base pressure changes can be attributed to the nonuniformity of the flow caused by the initial throat conditions. A large amount of finite difference numerical analysis has recently been done in an attempt to calculate the sonic line for nozzles with centerbodies. (Ref. 25). The steady compressible flow of an inviscid fluid through a converging-diverging two-dimensional planar duct with an arbitrarily shaped centerbody was treated using the time-dependent finite difference equations. The arbitrary shape of the duct and centerbody was transformed onto a normal flow plane in which the steady state solution was obtained as an asymptotic finite difference solution.
An incompressible solution was obtained analytically using a geometric transformation and compared with the compressible solution for cases where low velocities were obtained throughout the duct. Inviscid compressible solutions were obtained for various converging-diverging geometries both with and without centerbodies. These solutions covered the compressible range of velocities up to and including transonic. The converged inviscid solution was then used as an initial approximation for the solution of the viscous Navier-Stokes equations in the transformed plane.

The resulting viscous flow solution obtained by using the converged inviscid solution as an initial condition gave good correlation with experimental results in the throat region for a Foelsch nozzle with a large centerbody. Both the experimental data and numerical solutions tend to indicate that in the throat region the higher Mach number occurs near the large centerbody rather than along the outer contour as found from the inviscid solution for the same case. This demonstrated the necessity for investigating the viscous effects in the throat region of compressible nozzles. Although the results have been very encouraging, more work of this type will have to be done before a practical procedure for determining sonic lines will be available.

Shroud Contour Truncation

The results of truncating the shroud of an E-D nozzle contour are presented in Fig. 49. In these plots the ambient pressure remained constant at $P_a/P_{ol} = 0.01020$, while the nozzle shroud was truncated. Fig. 49a presents the full shroud contour ($A_{ex}/A_{nt} = 5.602$). The flow at the end of the shroud undergoes a mild expansion and adjusts rapidly to the ambient conditions. In Fig. 49b the exit area ratio is now 5.580, a reduction in exit area of only 0.39%. A significant change in the flow field is noted. A more noticeable expansion to ambient conditions is detected at the shroud tip. This occurs because the Mach number at the end of the shroud is lower; therefore, a larger change in the streamline angle is required to adjust to the ambient pressure.

A variation in the streamline patterns is also evident. The streamline closest to the near wake remains unchanged, but the next streamline experiences some deviation at approximately $x/r_b = 4.5$. The effects of the expansion have penetrated into the flow field, and give this streamline (and the streamline above it) its additional curvature. The shape of the recompression shock has also been altered slightly. The lower half of the shock remains unaffected, but the upper half becomes somewhat shallower than in the previous configuration.

In Fig. 49c the contour has been further truncated so that $A_{ex}/A_{nt} = 5.513$, a decrease in exit area of 1.59% from the design conditions. The expansion at the shroud tip becomes more pronounced, since the exit Mach number at this point has decreased still further. The streamlines, in turn, reflect the degree of influence of the truncation; the recompression shock shape has been altered significantly. The shock appears nearly straight; however, the initial shock angle at recompression is the same as the previous two cases. This observation is significant because the base pressure for all three cases remains unchanged. The effects of the shroud contour truncation have not yet been felt in the near wake region. Because of the analytical base pressure solution is a function of only conditions up to and including recompression, the base pressure remains constant. Although the analysis does predict a constant base pressure for the cases described above, this result may not hold experimentally for all situations (Ref. 1). It is readily seen in Fig. 49c that the influence of the truncated contour is felt just above the recompression point in the flow field. Downstream of the recompression shock, the effect of the shroud truncation is detected in the far wake very close to recompression. In the actual flow field of such a nozzle configuration, the near wake is affected by disturbances in the far wake (Refs. 22, 1 and 26) at least until the far wake has accelerated to supersonic conditions. Unfortunately experimental data are not available for this contour truncation case.

Another interesting feature of these flow fields may be noted by comparing the Mach numbers just upstream of the recompression shock. The highest Mach numbers ahead of the shock are obtained in Fig. 49b. This is partially due to the amount of "turning back" which the constant pressure boundary undergoes. This may be further explained by comparing the Mach numbers along the second streamline below the constant pressure boundary. In Fig. 49a the Mach number reaches a maximum of 4.04 at the intersection with the recompression shock. The corresponding streamline in Fig. 49b has the same Mach number variation until $x/r_b = 4.5$. At this point the streamline shows additional upward curvature, indicating continued expansion. The Mach number reaches its maximum value of 4.49 again at the intersection with the recompression shock. Although the corresponding streamline in Fig. 49c is incomplete, the reason for the Mach number decrease may be explained by noting the shape of the streamline above the one under consideration. It is seen that the streamline is turned back to the axial direction. This flow situation produces compression waves in that region which correspond

to a decrease in the Mach number. In addition, it is noted in Fig. 49c
that the constant pressure boundary not only becomes horizontal, but
also begins to assume a negative flow direction. The reason for this
change in direction of the constant pressure boundary may be seen by
noting the expansion of the fluid around the plug tip and in the near
wake region. On a solid boundary, a reflected wave is of the same
family as the incident wave, i.e., an incident compression wave reflects
as a compression wave. Whereas, for a constant pressure boundary, waves
are reflected which are of the opposite family as the incident waves
(Ref. 27). Thus the expanding flow within the confines of the nozzle
reflects from the constant pressure boundary as compression waves.

The usefulness of this study may be realized by undertaking an
engineering study to determine the thrust/weight ratio of the vehicle,
since it is most advantageous to have a high thrust/weight ratio for
efficient operation. The total thrust of the nozzle decreases with
truncation as does the weight of the nozzle. Depending on the payload
and the mission, some truncation may prove beneficial.

Nozzle Area Ratio

One technique to increase the velocity and, therefore, the thrust
produced by the gas within a nozzle is to change the overall area ratio,
A_{ex}/A_{nt}, of the nozzle. An internal-external-expansion nozzle having
a shroud contour which was moveable in the vertical direction was in-
vestigated analytically. The plug was a conical surface at an angle
of -7.97°, and the axial length of the plug, x/r_b. was 5.000. The
non-dimensional radius of the plug at the throat, r/r_b, was 1.70.
The results of this analytical investigation are presented in Fig. 50.
Note that an increasing area ratio produces a corresponding decrease
in the base pressure. This result is to be expected, since an increas-
ing overall area ratio implies a higher design Mach number of a nozzle.
It has been well documented (e.g., Refs. 9, 13, 14, & 28) that the base
pressure ratio does decrease with increasing Mach number.

Non-Isoenergetic Mixing

Immediately after ignition the plug base in a plug nozzle flow
field may be at a significantly lower temperature than the stagnation
temperature of the fluid adjacent to the near wake. The base tempera-
tures for both cases then begin to approach the fluid stagnation tempera-
ture asymptotically. In the interim, however, the performance of the
nozzle may vary appreciably; once a thermal equilibrium is approached,
the effects of the temperature difference disappear. The solution
presented in this dissertation cannot predict the actual transient
variation of the base pressure with the rate of increase (or decrease)
of base temperature. The analysis can provide, however, an accurate
representation of the flow field providing the rate of temperature
changing is not too large.

A study was undertaken to determine the effects of base heating

and cooling, and the results are shown in Fig. 51. This base tempera-
ture ratio curve is for an axisymmetric expansion-deflection nozzle,
(A_{ex}/A_{nt} = 5.602, and A_b/A_{nt} = 2.448) with no base bleed and no ini-
tial boundary layer. Note in this figure that for $T_b/T_{o1} > 1$ (base
heating), the base pressure increases. For $T_b/T_{o1} < 1$ (base cooling),
the base pressure drops off. This trend has been demonstrated by other
authors (Refs. 14, 29 & 30) for simple problems.

For base cooling the base pressure decreases quite rapidly, and
the slope of the curve remains relatively constant. With heat addi-
tion the rise of the base pressure is, at first, relatively large.
With increasing heat addition, the rate of increase of the base pres-
sure decreases. This phenomenon may be explained partly by the fact
that there is no upper bound on the temperature ratio in the analysis
used; however, a lower limit does exist, i.e., $T_b/T_{o1} \to 0$. Of course,
this lower limit is physically impossible, just as exceedingly high
base temperatures are also physically unrealistic. The range of the
curve presented in Fig. 51 should, therefore, include the limits of
most base heating and cooling problems which are encountered.

Internal Shock Wave

The shape of the constant pressure boundary downstream of the
nozzle exit is the governing influence in the formation of the internal
shock system. The constant pressure boundary divides the fluid exit-
ing from the nozzle from the quiescent (or still) fluid into which the
nozzle exhausts. The curvature associated with the constant pressure
boundary may be attributed to two primary mechanisms. The first is
associated with the properties of waves reflected from such a boundary.
That is, an expansion wave originating within the nozzle flow field
will be reflected as a compression wave (Ref. 27), thus decreasing
the streamline angle. The second variable is the degree of nonuniform-
ity of the flow at the nozzle exit. It has been noted in many configu-
rations, especially those associated with long truncated plug nozzles,
that the flow may pass through alternating regions of expansion and
compression. This phenomenon has also been encountered by other au-
thors both experimentally and analytically, (Refs. 31 and 32), for
other nozzle geometries.

An internal shock is formed by the coalescence of compression
waves generated at the jet boundary. Much research has been done on
internal shock systems. Most of the analyses (Refs. 27, 33 & 34) have
been restricted to flows in converging-diverging nozzles (bell or coni-
cal) in which the nozzle exit velocity is either uniform or easily
described by some analytic function (e.g., radial flow). Other authors
(Refs. 35 & 36) have included a certain degree of nonuniform flow at
the nozzle exit. Farmer, et al (Ref. 36) have included the actual
flow fields within various C-D nozzles. In these flows chemical kine-
tics, the formation of additional shock waves, and turbulent mixing
were also considered. Reis, et al (Ref. 35) have included the effects
of the initial boundary layer along the nozzle contour in their analysis.

- 34 -

For C-D nozzle configurations, the internal shock plays an import-
ant role in the development of the flow downstream of the nozzle exit.
For overexpanded nozzles ($P_a/P_e > 1$), the internal shocks meet at the
nozzle axis producing the familiar diamond configuration. For under-
expanded nozzles ($P_a/P_e < 1$), the internal shock ends at a Mach disc
(Ref. 27). Since this shock is formed by a gradual coalescence of
compression waves, the shock strength increases with axial distance
downstream.

On many nozzle streamline patterns which were obtained, it was
noted that a sharp discontinuity within the flow field occurred. Such
a situation is shown in Fig. 52 for an axisymmetric expansion-deflection
nozzle. It should be mentioned that the analysis used in this report
does not calculate the boundary shock per se. A "foldback" technique
(Ref. 33) is used which reduces the shock to an isentropic compression.
The validity of isentropic flow may seem to be not entirely valid con-
sidering the large gradients in Mach number over a very short distance.
The foldback procedure allows the calculations to continue despite
the intersection of characteristics of the same family. The charac-
teristic equations, in effect, are allowed to "handle their own dif-
ficulties" by ignoring these intersections. The location of the shock
in the flow field may be determined by the inner envelope of inter-
sections of the characteristics. The flow downstream of the shock is
obtained by deleting the foldback portion of the characteristics solu-
tion. This technique accurately predicts the constant pressure bound-
ary and internal shock locations (Refs. 33 and 34), despite the assump-
tion of an isentropic flow. The use of rotational characteristics to
account for the entropy gradient has also been done (Ref. 35), and the
authors claim improved results. The results obtained using rotational
characteristics undoubtedly do produce a more exact comparison with
the data, but the changes are very slight. At hypersonic Mach numbers
the agreement between both methods would not be as good; therefore,
rotational characteristics would provide some significant improvement.

Referring again to Fig. 52, the location of the internal shock
may be obtained by noting the streamline patterns of the flow field.
Streamline numbers 5, 6, and 7 all are turned abruptly. Although they
remain distinct, they are very close together. On streamline number 8
a gradual compression (i.e., a turning back of the streamline to the
axial direction) is noted at an axial distance, x/r_b, of about 5.0.
The Mach number drops from a value of 4.31 to 3.78, and the streamline
angle decreases from $+12.8^\circ$ to $+3.8^\circ$. Although this is a rather for-
midable change in both Mach number and streamline angle, the formation
of a strong internal shock appears not to have occurred since the axial
distance of this compression is greater than 1.0. For a shock wave to
develop, the compression must take place in a very short distance.

On streamline number 7 at an axial distance of approximately 6.1,
however, a strong compression occurs. At this point the Mach number
decreases from a value of 4.6 to a value of 3.8, and the streamline
angle changes from 13.5° to 4.0°. The axial distance involved is less

than 0.16; there are no intervening points which would indicate a gradual compression as was the case for streamline number 8. Similarly on streamline number 6, the Mach number decreases from 4.6 to 3.7, and the streamline angle decreases from 15.6° to 3.0° at an axial distance of 7.4. Streamline number 5, at a distance of 8.5, demonstrates the same phenomenon. The Mach number decreases from a value of 4.8 to a value of 3.7, and the streamline angle changes from 16.3° to 2.4°.

The locus of these sharp changes in flow direction, then, specifies the location of the internal shock. In addition, note that the strength of the shock appears to increase with axial distance. This is evidenced by the increase in the upstream Mach number and the increase in the total angular deflection through the shock. However, this increase of the strength of the shock with axial distance does not appear to be so large that severe entropy gradients are encountered from streamline to streamline. Thus a "nearly homentropic" flow results from these calculations and permits a solution by an irrotational method of characteristics.

The general features of the flow may be examined along a line drawn perpendicular to the centerline of the nozzle. From outside the near wake, the Mach number of the flow increases with radial distance until the internal shock is encountered. A Mach number decrease occurs across the internal shock such that the downstream Mach number is close to the Mach number along the constant pressure boundary. In some instances it was found that the Mach number downstream of the shock decreased slightly with radial distance, while it increased slightly at other locations. This may be attributed to the nonuniformity of the flow approaching the shock.

Ambient Pressure Variation

As rocket or air-breathing engines are operated at higher and higher altitudes, the ambient pressure decreases while the chamber pressure may remain relatively constant. This variation of ambient pressure has a very pronounced effect on the flow fields of plug nozzle configurations. Figs. 53 and 54 demonstrate the effect of raising the ambient pressure for an expansion-deflection and truncated plug nozzle flow field respectively. Fig. 52 shows a planar E-D nozzle with: $A_{ex}/A_{nt} = 2.007$ and $A_b/A_{nt} = 0.833$, while the geometry of the planar T-P nozzle is: $A_{ex}/A_{nt} = 15.573$ and $A_b/A_{nt} = 13.330$.

In Fig. 53a the ambient pressure ratio, P_a/P_{ol}, is 0.03401; for Fig. 53b, $P_a/P_{ol} = 0.10204$; and in Fig. 53c, $P_a/P_{ol} = 0.17007$. With the increasing ambient pressure ratio, i.e., decreasing altitude, the expansion at the shroud tip decreases noticeably. This is due to the exit pressure undergoing a smaller adjustment to the ambient pressure as the ambient pressure increases. In Fig. 53b a slight down turn of the constant pressure boundary is noted, while in Fig. 53c the negative flow angle becomes quite sharp. This variation in flow direction corresponds to a Mach number decrease within the flow field, i.e., compression

waves are generated at this boundary. Another interesting feature of
this particular study is that the base pressure remains constant for
all three cases shown. This occurs because the effect of the changing
ambient pressure does not affect the near wake solution, i.e., the right-
running characteristic from the contour tip intersects the trailing
wake downstream of recompression.

Fig. 54 describes the planar T-P nozzle where the following am-
bient conditions exist: P_a/P_{o1} = 0.0102 (Fig. 54a); P_a/P_{o1} = 0.02041
(Fig. 54b); and P_a/P_{o1} = 0.02721 (Fig. 54c). Again the negative slope
of the constant pressure boundary becomes increasingly severe with
rising ambient pressure. A mild compression emenates from this bound-
ary because of the shape. In Figs. 54b and 54c, the merging of stream-
lines indicates the possible location of an internal shock within the
flow field. The streamline adjacent to the constant pressure boundary
in Fig. 54a also exhibits a compressive turn at x = 7.7 inches. Thus
the internal shock appears to move more deeply into the flow field with
increasing ambient pressure.

Despite the large effects of the changing ambient pressure on
the actual flow field, the nozzle base pressure remains constant.
Note that an expansion still occurs at the shroud tip. Even at the
highest ambient pressure, the first characteristic from the constant
pressure boundary intersects the wake downstream of recompression.
Thus no change in the base pressure of the analytical model occurs.

Base Bleed

It has been shown that mass addition into the near wake of a blunt
body is an effective means of substantially increasing the base pressure
(Refs. 14 and 37). This increase in the base pressure, in turn, in-
creases the total thrust of the nozzle. An analytical determination
of the base bleed characteristics of an axisymmetric expansion-deflec-
tion nozzle was examined. Fig. 55 presents the plug base pressure
results of this investigation, while Fig. 56 shows the actual effects
of base bleed on the flow field of the nozzle. In this latter figure,
three representative conditions are shown: that of no base bleed;
that in which the non-dimensional bleed number, $\mathcal{H}$, is 0.000258; and
that where the non-dimensional bleed rate is 0.000777.

Referring to Fig. 55, note that a relatively small amount of bleed
produces a substantial increase in the base pressure. For this par-
ticular nozzle the base pressure rises rapidly to a bleed number of
approximately 0.00040. With increasing values of $\mathcal{H}$, the rate of base
pressure increase begins to taper off. For example, at $\mathcal{H}$ = 0.00040,
the base pressure has risen about 27%; increasing the bleed number an
additional 0.00080 produces an additional increase in the base pres-
sure of only 21%. Because of the shape of this curve, it appears rea-
sonable that some optimum bleed rate may be obtained for each par-
ticular nozzle in which the increase in base pressure due to bleed
would be balanced by the decrease in the actual mass flow of the nozzle.

In this analysis, however, the mass flow of the nozzle remained constant and did not reflect any decrease in the stagnation pressure or mass flow due to bleed. The base pressure in all of the cases shown in Fig. 56 contributes to the thrust of the nozzle, i.e., the base pressure is higher than the ambient pressure. Since the base pressure increases with increasing bleed, addditional thrust may be obtained with increasing bleed.

In Fig. 56, the flow fields for the three cases presented do differ markedly because of base bleed. Fig. 56 presents the pressure along the near wake up to and including recompression for the three cases of base bleed discussed above. For no base bleed, the base pressure is the lowest; immediately after separation the pressure decreases slightly indicating a Mach number increase. The pressure then begins to increase once again, and a sharp pressure rise is encountered at recompression. When base bleed is present, the general features of the pressure along the near wake remain the same. Increasing bleed rates produce an increase in the base pressure as shown above. The pressure remains higher until the vicinity of recompression. At that point the pressures are nearly identical. However, the pressure rise at recompression is reduced because of the decreased "corresponding inviscid jet boundary" angle. Thus, increasing the bleed rate produces a less severe pressure rise at recompression.

Initial Boundary Layer

An initial boundary layer just upstream of the separation corner on the plug base may produce significant changes in the plug nozzle flow field. In the other sections of this report, the boundary layer has been assumed to be fully turbulent, although a negligible thickness has been assumed.

Fig. 58a shows the effect of an initial boundary layer on the base pressure of an axisymmetric expansion-deflection nozzle. In addition, the variation of the base pressure with the profile exponent is also presented in that figure. Because the boundary layer is treated as an equivalent bleed, a rise in the base pressure with increasing boundary layer thickness is to be expected. The variation of base pressure in Fig. 58 may be attributed to the change in the momentum thickness for each particular profile. That is, for the same boundary layer thickness, δ, a 1/5 power law profile results in a larger momentum thickness than the 1/7 power law profile. Similarly, the 1/7 power law profile has a greater momentum thickness than the 1/9 power law profile. The amount of equivalent bleed is a direct function of the momentum thickness. Fig. 58b shows this result. Note that this curve very closely resembles the base bleed curve (Fig. 55) which is the expected result. It should also be mentioned that the analysis used here is for a gas with a turbulent Prandtl number of unity. In addition to these assumptions, two additional geometric restrictions of this particular technique of handling an initial boundary layer are:

1) The boundary layer thickness must be relatively small as compared to the base radius (or base half-height for planar nozzles)

2) The boundary layer thickness must be small as compared to the throat height.

This second restriction is necessary since a large boundary layer in the throat would alter the initial profile in the potential flow region by significantly decreasing the mass flow within the nozzle. This problem would become more acute in large expansion ratio nozzles with a small throat area; the effects of this mass deficit would be magnified by the overall large expansion of the nozzle.

COMPARISON OF EXPERIMENTAL AND ANALYTICAL RESULTS

A larger version of the internal-external-expansion nozzle flow field of Fig. 36f is presented in Fig. 59. The free jet boundary begins at the shroud contour exit, and the adjustment to the ambient pressure occurs at this point. The general shape of the boundary resembles that of other T-P nozzle flow fields. The separated flow region is visible, although not sharply defined. The shape of the near wake appears nearly conical, thus supporting the conetail solution concept of the near wake. Furthermore, a lip shock of significant strength does not appear to be present.

Another feature of the flow, which is clearly visible, is the internal shock. This internal shock results from the fact that the flow is underexpanded at the shroud exit (i.e., the Mach number at the shroud exit based on the area ratio is 1.56 and $P_{at}/P_{ol} = 0.136$) and the subsequent overexpansion at the shroud tip causes the flow to recompress by the formation of an internal shock. The shock begins at the shroud contour exit and permeates rather deeply into the flow field. Note that the intersection of this internal shock and the recompression shock produces a sharp change in the wave angle of both shock waves. The internal shock terminates at the Mach disc. This Mach disc is actually a normal shock which produces subsonic flow immediately downstream. A trailing shock emanating from the edge of the Mach disc may also be observed. In general, the flow up to the Mach disc may be predicted analytically using the techniques presented in this report.

A comparison of the experimental and analytical flow fields is made in Fig. 60. Fair qualitative agreement is obtained between the shadowgraph picture and the calculated flow field. The shape of the calculated external jet boundary in Fig. 60 coincides with the external jet boundary of the actual flow very closely. Note that in the analytical solution, only part of the recompression shock and the streamlines are presented. This is because of the analytical difficulties which were encountered with the internal shock. In the analytical solution, a "uniform" sonic line was used to begin the calculations and the wake radius ratio was taken from the data of Chapman. The recompression coefficient was assumed to be unity, i.e., recompression along the d-streamline occurred at the peak pressure downstream of the shock. A negligible boundary layer was assumed.

The base pressure ratio for this nozzle measured in the Nozzle Thrust Facility was: $P_b/P_{ol} = 0.0693$. The calculated base pressure ratio was 0.0878. The discrepancy in the measured and calculated values of the base pressure ratio is most likely a result of the lack of accurate input information as well as the shortcomings of the method. For example, the assumption of a "uniform" sonic line is known to be incorrect. Furthermore, viscous effects may not be negligible considering the relatively small size of the nozzle. The gap in the throat region between the plug and the shroud is only 0.163 inches; therefore, a small boundary layer on both surfaces would decrease the effective

throat area. This would produce a larger overall area ratio, thereby decreasing the base pressure. When these input data are improved, the analytical results will undoubtedly improve. It should be mentioned that exact agreement between the calculated and measured values of base pressure ratio could have been obtained by using a specific value of the recompression coefficient which was less than one. However, since there is no method at present for determining, a priori, the exact value of N which will work, this purely empirical method was not used. The most serious shortcoming of the present calculation procedure which could significantly affect this comparison is the omission of the relatively strong internal shock.

An additional comparison of the analytical method with experimental data was obtained from Ref. 39. Again an internal-external-expansion nozzle (Fig. 61) was used in which $A_{ex}/A_{nt} = 24.0$ and $A_i/A_{nt} = 12.0$. The overall exit diameter of the nozzle was 3.0 inches, and the conical plug had a cone half angle of $-17.0°$. Three plug lengths were investigated: $L/L_{max} = 0.091$; $L/L_{max} = 0.145$; and $L/L_{max} = 0.288$. Base pressure measurements were obtained at each of these plug lengths. In the analytical results, the value of N in this case was assumed equal to unity. The experimental and analytical base pressure measurements compare quite well for the configuration where $L/L_{max} = 0.091$. The experimentally measured value of the base pressure ratio, P_b/P_{ol}, was 0.00346, whereas the analytical prediction was $P_b/P_{ol} = 0.00342$. In the analytical solution a "uniform" Mach number profile just downstream of the throat was assumed. A shadowgraph of the flow field did not show a strong internal shock which might account for the good base pressure agreement. Although shadowgraphs were not available for the other geometries, the base pressure data was available. At a plug length ratio of $L/L_{max} = 0.145$, the experimental base pressure ratio was $P_b/P_{ol} = 0.00385$, and the analytical value was 0.00370, again demonstrating good agreement. At the longest plug length, $L/L_{max} = 0.288$, excellent correlation was obtained. The experimental value of the base pressure ratio was 0.00365, and the analytical value was $P_b/P_{ol} = 0.00366$. One possible explanation for the fact that the comparison between analysis and experiment is much better for the nozzle of Ref. 39 than for the nozzle of Fig. 59 is that the nozzle total pressures were significantly different resulting in different Reynolds numbers for the two cases.

A comparison of analytical and experimental results for an extended contour planar expansion-deflection nozzle is shown in Fig. 62. For this nozzle the overall expansion ratio, A_{ex}/A_{nt}, was 1.965 and the base area ratio, A_b/A_{nt}, was 0.815. Details of this nozzle design and its operating characteristics may be found in Refs. 22 and 38. A simultaneous smokeline-schlieren photograph of the "closed" wake flow field for this nozzle is reproduced in Fig. 62. The measured base pressure ratio for this case was $P_b/P_{ol} = 0.13$. The wake radius ratio* was estimated from Fig. 62 to be about 0.243. The calculated base pressure ratio for this value of the wake radius ratio, a straight sonic line

* In this planar case the analogous wake length ratio was used.

and $N = 1$ is $P_b/P_{ol} = 0.135$. The comparison of the calculated stream-
lines, near wake shape, and recompression shock with the experimental
is reasonably good. This good agreement may be a result of the absence
of internal shock waves in the flow adjacent to the near wake.

CONCLUSIONS AND RECOMMENDATIONS

The experimental base pressure characteristics of truncated plug nozzles provide a convenient means of classifying the nozzle flow as having either an "open" or "closed" wake. It was found for a planar external-expansion truncated plug nozzle with a constant upstream stagnation pressure that as the exhaust pressure decreased, the base pressure of the "open" wake decreased and was approximately equal to the cell pressure (i.e. ambient pressure). The presence of a diffuser did not appear to noticeably affect the "open" wake nozzle operation although it did affect the ejector-diffuser system operation. As the exhaust pressure was further decreased the base pressure continued to decrease until an unstable region was reached in which the wake switched alternately between the "open" and "closed" configurations. A small decrease in exhaust pressure from the value which produced this unstable situation resulted in a "closed" wake. The wake "closed" at essentially the same cell pressure with and without the diffuser. However, the "closed" wake base pressure was about 10% lower with the diffuser present.

For the axisymmetric internal-external-expansion truncated plug nozzle with a constant ambient pressure, base pressure characteristics very similar to the planar case were obtained as the upstream stagnation pressure was increased. In most of the "open" wake region, the base pressure was equal to the ambient pressure. In general this trend continued until the wake "closed". An exception to this general trend occurred in a small region where the shock wave originating at the shroud exit, impinged and was reflected from the plug close enough to the base to produce a decrease and then an increase in the base pressure as the ambient pressure decreased.

Optical investigations of the planar expansion-deflection and truncated plug nozzles as well as the axisymmetric truncated plug nozzle have demonstrated that the lip shock was not of significant strength in the cases studied. The lip shock was therefore not included in the analytical model for the flow field.

The studies on the effects of turbulence seem to indicate that the separated free shear layer is turbulent whether the plug boundary layer is laminar or turbulent. This result justifies the use of turbulent mixing in the base pressure theory. Further experimental data should be obtained to better define the shear layer growth as well as the base recirculation patterns.

Base bleed was shown to have a substantial effect on the base pressure and the nozzle flow field in general. Opaque-stop schlieren photographs of the planar truncated plug nozzle flow field showed a marked increase in the thickness of the wake neck. Also, the base bleed strengthened the lip shock and changed its location. The results of the particular cases studied indicated that even a small amount of base bleed can have a large effect on the base pressure with about 1% bleed producing about a 40% increase in the base pressure. Another

effect of base bleed is that the peak recompression pressure decreases with increasing bleed, and the location of the peak pressure on the nozzle centerline is shifted slightly downstream with increasing bleed. More detailed data on the growth of the turbulent shear layer as well as on the recompression process would be helpful in understanding this complex situation.

The extension of the analytical method of Mueller and Hall (Ref. 9) to include nonuniform plug nozzle configurations produced the correct base pressure trends with overall nozzle area ratio, base temperature ratio, ambient pressure ratio, percent base bleed, and initial boundary layer thickness. Furthermore, the nozzle flow fields from the throat region to and including the recompression shock wave were obtained from this method. Good quantitative agreement was obtained between theory and experiment for a planar and an axisymmetric nozzle flow which did not have strong internal shock waves present. The agreement between theory and experiment for an axisymmeteric nozzle with a strong internal shock was not as good.

The experimental results on the location of the sonic line for the planar truncated plug nozzle have indicated that the sonic line is noticeably distorted. Since the sonic conditions are used in the establishment of the starting conditions for the method of characteristics, the sonic line shape and location could have a significant effect on the analytic solution. For most of the cases studied in the present investigation the sonic line was assumed to be straight and at the geometric throat. Therefore one necessary extension of the present method would be to include a more realistic sonic line in the analytic treatment. A strong internal shock wave can occur for a large number of plug nozzle configurations and operating conditions. Furthermore, the strength and position of this shock wave has a significant effect on the base pressure and flow field solution. Therefore it seems reasonable to expect better base pressure results from the analytical method if the internal shock is included in the inviscid flow field calculations.

APPENDIX I

GENERAL METHOD OF CHARACTERISTICS (Ref. 40)

A second order partial differential equation with two independent variables may be expressed in the following form:

$$A\Phi_{xx} + 2B\Phi_{xy} + C\Phi_{yy} = D \qquad (I-1)$$

where the coeffeicients A, B, C, and D may be functions of x, Φ_x, Φ_y, and Y. Assuming that Φ_x and Φ_y are continuous functions of X and Y, then for arbitrary increments of dX and dY:

$$d\Phi_x = \frac{\partial \Phi x}{\partial x} dx + \frac{\partial \Phi x}{\partial y} dy = \Phi_{xx}dx + \Phi_{xy}dy \qquad (I-2)$$

and:

$$d\Phi_y = \frac{\partial \Phi y}{\partial x} dx + \frac{\partial \Phi y}{\partial y} dy = \Phi_{xx}dx + \Phi_{xy} dy \qquad (I-3)$$

Each solution to Equation (I-1) is a three-dimensional surface in X, Y, Φ space (integral surface) defined by the function:

$$\Phi = \Phi(x,y) \qquad (I-4)$$

On certain curves on the integral surface, the derivitives of Φ_x and Φ_y may be discontinuous. These are known as characteristics curves. These projections on the X-Y plane are the physical characteristics. Note that Equation (I-1) applies to any point on the surface, while Equations (I-2) and (I-3) are applicable to the increments of a curve lying on that surface. Also, it must be stated that Φ_{xx}, Φ_{xy}, and Φ_{yy} may be indeterminate. Rearranging Equations (I-1), (I-2), and (I-3) gives:

$$A\Phi_{xx} + 2B\ \Phi_{xy} + C\Phi_{yy} = D \qquad (I-5a)$$

$$dX\Phi_{xx} + dY\ \Phi_{xy} + 0 = d\Phi_x \qquad (I-5b)$$

$$0 + dX\Phi_{xy} + dY\Phi_{yy} = d\Phi_y \qquad (I-5c)$$

These three equations can now be regarded as simultaneous linear algebraic equations in the variables Φ_{xx}, Φ_{xy}, and Φ_{yy}. Solving for Φ_{xy}:

$$\Phi_{xy} \quad \frac{\begin{vmatrix} A & D & C \\ dX & d\Phi_x & 0 \\ 0 & d\Phi_y & dY \end{vmatrix}}{\begin{vmatrix} A & 2B & C \\ dX & dY & 0 \\ 0 & dX & dY \end{vmatrix}} \qquad (I-6)$$

Since this is an indeterminate quantity, the denominator matrix is zero, i.e.:

$$A(dY)^2 - 2B(dXdY) + C(dX)^2 = 0 \qquad (I-7)$$

or:

$$A\left(\frac{dY}{dX}\right)^2 - 2B\left(\frac{dY}{dX}\right) + C = 0 \qquad (I-8)$$

Solving this quadratic equation results in:

$$\left(\frac{dY}{dX}\right)_{Char} = \frac{B \pm \sqrt{B^2 - AC}}{A} \qquad (I-9)$$

This equation determines the slope of the characteristic in the X-Y (physical) plane.

Since Φ_{xy} is, in general, finite, then the numerator of Equation (I-6) must also be zero, i.e.:

$$A(d\Phi_x dY) - D(dXdY) + C(d\Phi_y dX) = 0 \qquad (I-10)$$

or:

$$\left(\frac{d\Phi_y}{d\Phi_x}\right)_{Char} = \frac{A}{C}\left(\frac{dy}{dx}\right)_{Char} + \frac{D}{C}\left(\frac{dy}{d\Phi_x}\right)_{Char} \qquad (I-11)$$

Substituting the results of Equation (I-9) into Equation (I-11) yields:

$$\left(\frac{d\Phi_x}{d\Phi_y}\right)_{Char} = -\frac{B \pm \sqrt{B^2 - AC}}{C} + \frac{D}{C}\left(\frac{dY}{d\Phi_x}\right)_{Char} \qquad (I-12)$$

Thus Equation (I-12) determines the slope of the characteristics in the $\Phi_x - \Phi_y$ (hodograph) plane.

It is necessary to investigate the types of partial differential equations which may occur. The first will be the elliptic partial differential equation. In this case the quantity $(B^2 - AC)$ is negative resulting in two imaginary roots to the characteristic equations. Thus for an elliptic partial differential equation, the characteristics equations have no physical significance. The second type of partial differential equations, one real root results, but again no physical significance is obtained. The third type is the hyperbolic partial differential equation. Here the quantity $(B^2 - AC)$ is positive resulting in two real roots. For this case, a physical significance may be attached to these roots. Therefore, in order to employ the method of characteristics, the governing partial differential equation must be hyperbolic.

Properties of Characteristic Curves

On a characteristic curve:

1) Fluid properties (Φ_x and Φ_y) are continuous.
2) Derivitives of the fluid properties may be discontinuous.

Thus regions of differing fluid properties may be "patched" together to obtain a new region. Therefore solving the original partial differential equation is now reduced to solving two sets of first order ordinary differential equations.

Method of Solution

Equations (I-9) and (I-12) may be rewritten as:

$$\left(\frac{dy}{dx}\right)_I = \frac{B + \sqrt{B^2-AC}}{A} \tag{I-13a}$$

$$\left(\frac{dy}{dx}\right)_{II} = \frac{B - \sqrt{B^2-AC}}{A} \tag{I-13b}$$

$$\left(\frac{d\Phi_y}{d\Phi_x}\right)_I = -\frac{B + \sqrt{B^2-AC}}{C} - \frac{D}{C}\left(\frac{dy}{d\Phi_x}\right)_I \tag{I-13c}$$

$$\left(\frac{d\Phi_y}{d\Phi_x}\right)_{II} = -\frac{B - \sqrt{B^2-AC}}{C} - \frac{D}{C}\left(\frac{dy}{d\Phi_x}\right)_{II} \tag{I-13d}$$

Along a non-characteristic curve 1-2, Φ_x and Φ_y are known, i.e., given from the initial data curve. Referring to the sketch below, it is now possible to begin constructing the characteristic grid. In the X-Y (physical) plane, the location of point 3 is determined. This is done by applying Equation (I-13b) to point 1, and Equation (I-13a) to point 2.
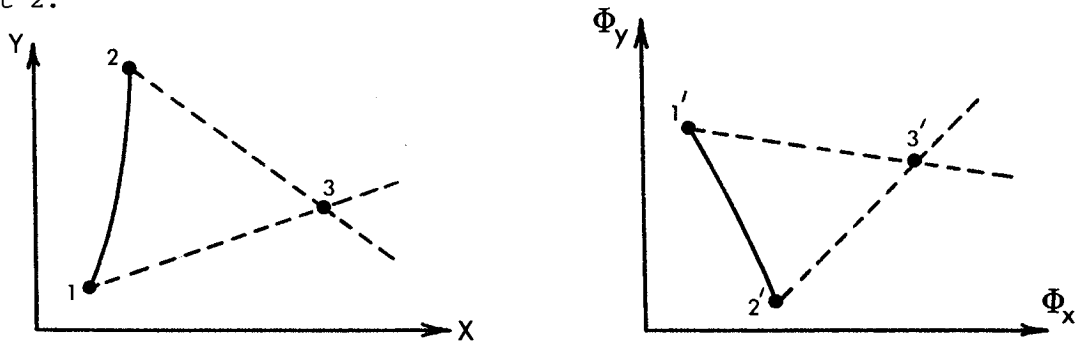
The intersection of these two lines locates in the physical space the position of point 3. It now becomes necessary to locate point 3' in the $\Phi_x - \Phi_y$ (hodograph) plane. Equation (I-13d) is applied to point 1' and Equation (I-13c) to point 2'. The resulting intersection of these two lines locates point 3' in the hodograph plane. It should be noted that the quantity $\left(\frac{dy}{d\Phi_x}\right)$ may be approximated by:

$$\left(\frac{dy}{d\Phi_x}\right)_I = \frac{Y_3 - Y_2}{(\Phi_x)_{3'} - (\Phi_x)_{2'}} \qquad (I-14)$$

where Y_3 is determined from the calculations in the physical plane, and $(\Phi_x)_{3'}$ is estimated. An iteration scheme is then employed using average slopes to obtain accurate solutions.

Rotational Method of Characteristics (Ref. 41)

The axisymmetric continuity equation may be expressed in the following form:

$$\rho V (\Delta n)(2\pi r) = CONSTANT \qquad (I-15)$$

Expanding in the form:

$$\rho V (\Delta n)(2\pi r) = \left[\rho V + \frac{\partial(\rho V)}{\partial s}\Delta s\right]\left[\Delta n + \frac{\partial(\Delta n)}{\partial s}\Delta s\right](2\pi)\left(r + \frac{\partial r}{\partial s}\Delta s\right) \qquad (I-16)$$

Since:

$$\frac{\partial(\Delta n)}{\partial s} = (\Delta n)\frac{\partial \theta}{\partial n} \qquad (I-17a)$$

and:

$$\lim_{\Delta r, \Delta s \to 0} \frac{\Delta r}{\Delta s} = \frac{\partial r}{\partial s} = \sin\theta \qquad (I-17b)$$

and letting $\Delta s \to 0$ results in:

$$\frac{\sin\theta}{r} + \frac{\partial \theta}{\partial n} + \frac{1}{V}\frac{\partial V}{\partial s} + \frac{1}{\rho}\frac{\partial \rho}{\partial s} = 0 \qquad (I-18)$$

The entropy will be assumed constant along a streamline, but will be permitted to vary from streamline to streamline. The enthalpy equation may be expressed as:

$$dh = Td\tilde{s} + \frac{dP}{\rho} \qquad (I-19)$$

In addition the adiabatic energy equation can be written:

$$h_o = h + V^2/2 \qquad (I-20)$$

The n-momentum equation may be expressed in the following form:

$$\frac{\partial P}{\partial n} = -\rho\frac{V^2}{R_s} = -\rho V^2\frac{\partial \theta}{\partial s} \qquad (I-21)$$

Combining Equations (I-19), (I-20) and (I-21) results in the new n-momentum equation:

$$\frac{1}{V}\frac{\partial V}{\partial n} - \frac{\partial \theta}{\partial s} = -\frac{T}{V^2}\frac{d\tilde{s}}{dn} \tag{I-22}$$

Assuming isentropic flow along a streamline, the s-momentum equation may be expressed as:

$$\frac{1}{\rho}\frac{\partial \rho}{\partial s} = -\frac{V}{a^2}\frac{\partial V}{\partial s} \tag{I-23}$$

Combining this s-momentum equation and continuity (I-18) gives:

$$\cot\mu\frac{1}{V}\frac{\partial V}{\partial s} - \tan\mu\frac{\partial \theta}{\partial n} = \tan\mu\frac{\sin\theta}{r} \tag{I-24}$$

Employing the definition of the Prandtl-Meyer function:

$$\nu = \int_{M=1}^{M} -d\theta = \int_{M=1}^{M} (M^2 - 1)^{\frac{1}{2}}\frac{dV}{V} \tag{I-25}$$

Results in two partial differential equations:

$$\frac{\partial \nu}{\partial s} - \tan\mu\frac{\partial \theta}{\partial n} = \tan\mu\frac{\sin\theta}{r} \tag{I-26a}$$

and:

$$\tan\mu\frac{\partial \nu}{\partial n} - \frac{\partial \theta}{\partial s} = -\frac{T}{V^2}\frac{d\tilde{s}}{dn} \tag{I-26b}$$

Adding these two equations results in:

$$\frac{\partial}{\partial s}(\nu-\theta) + \tan\mu\frac{\partial}{\partial n}(\nu-\theta) = \tan\mu\frac{\sin\theta}{r} - \frac{T}{V^2}\frac{d\tilde{s}}{dn}$$

while subtracting gives:

$$\frac{\partial}{\partial s}(\nu+\theta) - \tan\mu\frac{\partial}{\partial n}(\nu+\theta) = \tan\mu\frac{\sin\theta}{r} + \frac{T}{V^2}\frac{d\tilde{s}}{dn} \tag{I-28}$$

It may be shown that for any function, f, the characteristics equations may be written:

$$\frac{\partial f}{\partial s} + \tan\mu\frac{\partial f}{\partial n} = \frac{\partial f}{\partial \eta}\sec\mu \tag{I-29a}$$

and:

$$\frac{\partial f}{\partial s} - \tan\mu \frac{\partial f}{\partial n} = \frac{\partial f}{\partial \xi} \sec\mu \tag{I-29b}$$

Comparing Equations (I-29a) and (I-29b) with Equations (I-27) and (I-28) results in:

$$\frac{\partial (\nu-\theta)}{\partial \eta} = \sin\mu \frac{\sin\theta}{r} - \cos\mu \frac{T}{V^2} \frac{d\tilde{s}}{dn} \tag{I-30}$$

and:

$$\frac{\partial (\nu+\theta)}{\partial \xi} = \sin\mu \frac{\sin\theta}{r} + \cos\mu \frac{T}{V^2} \frac{d\tilde{s}}{dn} \tag{I-31}$$

Referring to the sketch and assuming:

$$\frac{\partial}{\partial \eta}(\nu-\theta) = \frac{d}{d\eta}(\nu-\theta) \text{ along } \eta$$

$$\frac{\partial}{\partial \xi}(\nu+\theta) = \frac{d}{d\xi}(\nu+\theta) \text{ along } \xi$$
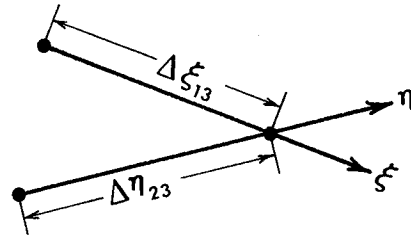
Integrating Equations (I-30) and (I-31) gives:

$$(\nu_3-\theta_3) - (\nu_2-\theta_2) = \int_2^3 (\text{Sin}\mu \frac{\sin\theta}{r}) d\eta - \cot\mu \frac{T}{V^2} (\tilde{s}_3 - \tilde{s}_2) \tag{I-32a}$$

and:

$$(\nu_3+\theta_3) - (\nu_1+\theta_1) = \int_1^3 (\sin\mu \frac{\sin\theta}{r}) d\xi - \cot\mu \frac{T}{V^2} (\tilde{s}_3 - \tilde{s}_1) \tag{I-32b}$$

or:

$$(\nu_3-\theta_3) - (\nu_2-\theta_2) = \overline{C}_{23}\Delta\eta_{23} - \overline{K}_{23} (\frac{\tilde{s}_3}{R} - \frac{\tilde{s}_2}{R}) \tag{I-33a}$$

and:

$$(\nu_3+\theta_3) - (\nu_1+\theta_1) = \overline{C}_{13}\Delta\xi_{13} - \overline{K}_{13}(\frac{\tilde{s}_3}{R} - \frac{\tilde{s}_1}{R}) \tag{I-33b}$$

where $\overline{C}$ denotes the average value of the integrand, i.e.:

$$C = \sin\mu\frac{\sin\theta}{r} \tag{I-34}$$

- 50 -

and where $\overline{K}$ is the average value of the following:

$$K = \frac{\sin\mu \, \cos\mu}{\gamma} \tag{I-35}$$

The resulting computational equations then become:

$$\nu_3 = \frac{F_1 + F_2}{2} \tag{I-36a}$$

and:

$$\theta_3 = \frac{F_1 - F_2}{2} \tag{I-36b}$$

where:

$$F_1 = (\nu_1 + \theta_1) + \overline{C}_{13}\Delta\xi_{13} - \overline{K}_{13}\left(\frac{\tilde{s}_3}{R} - \frac{\tilde{s}_1}{R}\right) \tag{I-37a}$$

and:

$$F_2 = (\nu_2 - \theta_2) + \overline{C}_{23}\Delta\eta_{23} - \overline{K}_{23}\left(\frac{\tilde{s}_3}{R} - \frac{\tilde{s}_2}{R}\right) \tag{I-37b}$$

Boundary Conditions

For simplicity let:

$$F_1 = (\nu_1 + \theta_1) + F_{1i} \tag{I-38a}$$

and

$$F_2 = (\nu_2 - \theta_2) + F_{2i} \tag{I-38b}$$

where:

$$F_{1i} = \overline{C}_{13}\Delta\xi_{13} - \overline{K}_{13}\left(\frac{\tilde{s}_3}{R} - \frac{\tilde{s}_1}{R}\right) \tag{I-39a}$$

and

$$F_{2i} = \overline{C}_{23}\Delta\eta_{23} - \overline{K}_{23}\left(\frac{\tilde{s}_3}{R} - \frac{\tilde{s}_2}{R}\right) \tag{I-39b}$$

For a solid boundary the streamline angle at the point to be calculated is known. Thus, since θ_3 is known, Equation (I-36b) may be solved algebraically for F_2. Upon substituting this result into Equation (I-36a), the following expression for ν_3 is obtained:

$$\nu_3 = \nu_1 + \theta_1 - \theta_3 + F_{1i} \tag{I-40}$$

At a lower constant pressure boundary, the Prandtl-Meyer turn angle, ν_3, may be considered known and constant. Thus solving Equation (I-36a) for F_2 and substituting this result into Equation (I-36b) gives the expression for the streamline angle at that point:

$$\theta_3 = \nu_1 + \theta_1 - \nu_3 + F_{1i} \qquad \text{(I-41)}$$

It should be noted that Equations (I-40) and (I-41) differ when the boundary being calculated is on an upper surface.

APPENDIX II

BASE PRESSURE SOLUTION WITH PRESSURE RISE (Ref. 10)

Referring to Fig. 37, the momentum equation between points (2) and (3) may be expressed as (Note: R and -R are positioned such that the cross-sectional area at any axial station is constant):

$$(PA)_2 + (\rho u^2 A)_2 = (PA)_3 + (\rho u^2 A)_3 \tag{II-1}$$

where:

$$A_2 = \int_{y-R}^{Y_R} 2\pi R_2 \cos\theta_2 dy_2 \tag{II-2a}$$

and:

$$A_3 = \int_{y-R}^{Y_R} 2\pi R_3 \cos\theta_3 dY_3 \tag{II-2b}$$

Substituting results in:

$$P_2\cos\theta_2 \int_{-R}^{R} 2\pi R_2 dy_2 + \cos\theta_2 \int_{-R}^{R} \rho_2 U_2^2 2\pi R_2 dy_2 =$$

$$\tag{II-3}$$

$$P_3\cos\theta_3 \int_{-R}^{R} 2\pi R_3 dY_3 + \cos\theta_3 \int_{-R}^{R} \rho_3 U_3^2 2\pi R_3 dY_3$$

For a conical wake assumption:

$$\theta_2 = \theta_3 \tag{II-4}$$

Therefore:

$$P_2 \int_{y-R}^{Y_R} R_2 dy_2 + \int_{y-R}^{Y_R} \rho_2 U_2^2 R_2 dy_2 = P_3 \int_{Y_{-R}}^{Y_R} R_3 dY_3 + \int_{Y_{-R}}^{Y_R} \rho_3 u_3^2 R_3 dY_3 \tag{II-5}$$

Since at point (2) no flow exists below $y = 0$, and since above $y = 0$, the flow is uniform, then:

$$P_2 \int_{Y_{-R}}^{Y_R} (R_o - y_2\cos\theta) dy_2 + \rho_{2a} u_{2a}^2 \int_{o}^{Y_R} (R_o - y_2\cos\theta_2) dy_2 =$$

$$\tag{II-6}$$

$$P_3 \int_{Y_{-R}}^{Y_R} (\overline{R}_3 - Y_3\cos\theta_3) dY_3 + \rho_{3a} u_{3a}^2 \int_{Y_{-R}}^{Y_R} (\frac{\rho_3}{\rho_{3a}}) (\frac{U_3^2}{U_{3a}^2}) (\overline{R} - Y_3\cos\theta_3) dY_3$$

where R_2 in Equation (II-5) is:

$$R_2 = R_o - y_2\cos\theta_2 \tag{II-7a}$$

and R_3 is defined as:

$$R_3 = \bar{R}_3 - Y_3\cos\theta_3 \tag{II-7b}$$

Since:

$$Y = y - y_m \tag{II-8a}$$

and:

$$dY = dy \tag{II-8b}$$

then:

$$P_2\left[R_o(y_R - y_{-R}) - \tfrac{1}{2}\cos\theta(y_R^2 - y_{-R}^2)\right]_2 + \rho_{2a}u_{2a}^2(R_oy_R - \tfrac{1}{2}\cos\theta y_R^2)_2 =$$

$$P_3\int_{y_{-R}}^{y_R}\left[\bar{R} - (y-y_m)\cos\theta\right]_3 dy_3 + \rho_{3a}u_{3a}^2\int_{y_{-R}}^{y_R}\left(\frac{\rho_3}{\rho_{3a}}\right)\left(\frac{u_3^2}{u_{3a}^2}\right)(R - Y\cos\theta)_3 dY_3 \tag{II-9}$$

Since the pressure normal to the flow is constant, then:

$$\rho_3/\rho_{3a} = (1 - c_{3a}^2)/(1 - c_{3a}^2\phi^2) \tag{II-10}$$

Defining the dimensionless coordinate, η, as:

$$\eta = \sigma\, y/x \tag{II-11}$$

where σ is the jet spread parameter.

Then:

$$Y = y - y_m = \frac{x}{\sigma}(\eta-\eta_m) \tag{II-12a}$$

and:

$$dy = dY = \frac{x}{\sigma}\, d\eta \tag{II-12b}$$

Also noting that:

$$y_R - y_{-R} = 2y_R \tag{II-13a}$$

and:

$$y_R^2 - y_{-R}^2 = 0 \tag{II-13b}$$

Then Equation (II-9) becomes:

$$\frac{P_2}{\rho_{2a}u_{2a}^2}(2R_oy_R)_2 + (R_oy_R - \tfrac{1}{2}\cos\theta y_R^2)_2 = \frac{P_3}{\rho_{2a}u_{2a}^2}\int_{\eta-R}^{\eta_R}\frac{x}{\sigma}\left[\overline{R}- (\eta-\eta_m)\cos\theta\right]_3 d\eta_3$$

$$+ \frac{P_3}{P_2}\frac{P_2}{P_3}\frac{\rho_{3a}u_{3a}^2}{\rho_{3a}u_{3a}^2}(1 - C_{3a}^2)\left[\frac{Rx}{\sigma}I_2\Big|_{\eta_{-R}}^{\eta_R} - (\frac{x}{\sigma})^2\cos\theta (J_2\Big|_{\eta_{-R}}^{\eta_R} -\eta_m I_2\Big|_{\eta_{-R}}^{\eta_R})\right]_3 \qquad (II-14)$$

Since:

$$\frac{P}{\rho u^2} = \frac{1 - C^2}{\frac{2\gamma}{\gamma-1}C^2} \qquad (II-15)$$

It should be noted that:

$$I_2 = \int\frac{\phi^2}{1-C_{3a}^2\phi^2}d\eta \qquad (II-16a)$$

and:

$$J_2 = \int\frac{\phi^2\eta}{1-C_{3a}^2\phi^2}d\eta \qquad (II-16b)$$

and the η-values in Equation (II-14) refer to the limits of integration. By employing Equation (II-15), Equation (II-14) finally reduces to:

$$\frac{1-C_{2a}^2}{\frac{2\gamma}{\gamma-1}C_{2a}^2}(2R_oy_R)_2 + (R_oy_R - \tfrac{1}{2}\cos\theta y_R^2)_2 =$$

$$\frac{P_3(1-C_{2c}^2)}{P_2\ C_{2a}^2}\left\{\frac{\gamma-1}{2\gamma}\left[\frac{\overline{R}x}{\sigma}(2\eta_R) - (\frac{x}{\sigma})^2\cos\theta(-2\eta_m\eta_R)\right] + \right.$$

$$\left. C_{3a}^2\left[\frac{Rx}{\sigma}I_2\Big|_{\eta_{-R}}^{\eta_R} - (\frac{x}{\sigma})^2\cos\theta(J_2\Big|_{\eta_{-R}}^{\eta_R} - \eta_m I_2\Big|_{\eta_{-R}}^{\eta_R})\right]\right\}_3 \qquad (II-17)$$

This equation, then, describes the momentum transfer between stations (2) and (3).

The viscous continuity equation between stations (2) and (3) may be expressed in the following form:

$$\int_0^{y_R}\rho_2 u_2 2\pi R_2 dy_2 = \int_{y_j}^{y_R}\rho_3 u_3 2\pi R_3 dy_3 \qquad (II-18)$$

Using the relations which were employed for the momentum equation, this continuity equation reduces to:

$$(R_0 y_R - \tfrac{1}{2}\cos y_R^2)_2 =$$

$$\frac{P_3 C_{3a}}{P_2 C_{2a}}(1 - c_{2a}^2) \int_{\eta_j}^{\eta_R} \frac{\phi}{1 - c_{3a}^2 \phi^2} \left[\bar{R} - \frac{x}{\sigma}(\eta - \eta_m)\cos\theta\right] \frac{x_3}{3\sigma_3} d\eta_3 \qquad (II\text{-}19)$$

or finally:

$$(R_0 y_R - \tfrac{1}{2}\cos\theta y_R^2)_2 =$$

$$\frac{P_3}{P_2}\frac{C_{3a}}{C_{2a}}(1 - c_{2a}^2)\left\{\frac{\bar{R}x}{\sigma}\left.I_1\right|_{\eta_j}^{\eta_R} - \left(\frac{x}{\sigma}\right)^2\cos\theta\left[\left.J_1\right|_{\eta_j}^{\eta_R} - \eta_m \left.I_1\right|_{\eta_j}^{\eta_R}\right]\right\}_3 \qquad (II\text{-}20)$$

where:

$$I_1 = \int \frac{\phi}{1 - c_{3a}^2 \phi^2} d\eta \qquad (II\text{-}21a)$$

and:

$$J_1 = \int \frac{\phi\eta}{1 - c_{3a}^2 \phi^2} d\eta \qquad (II\text{-}21b)$$

Since the cross sectional area between R and -R is assumed constant, then:

$$(2R_0 y_R)_2 = \frac{\bar{R}x}{\sigma}(2\eta_R) - \left(\frac{x}{\sigma}\right)^2\cos\theta(-2\eta_m\eta_R) \qquad (II\text{-}22)$$

Combining the continuity equation (II-20) and the momentum equation (II-17) results in:

$$\frac{P_3}{P_2}\frac{C_{3a}}{C_{2a}}\left\{\frac{\bar{R}x}{\sigma}\left.I_1\right|_{\eta_j}^{\eta_R} - \left(\frac{x}{\sigma}\right)^2\cos\theta\left[\left.J_1\right|_{\eta_j}^{\eta_R} - \eta_m \left.I_1\right|_{\eta_j}^{\eta_R}\right]\right\}_3 =$$

$$\frac{\gamma-1}{\frac{2\gamma}{c_{2a}^2}}\left(\frac{P_3}{P_2} - 1\right)\left[\frac{\bar{R}x}{\sigma}(2\eta_R) - \left(\frac{x}{\sigma}\right)^2\cos\theta(-2\eta_m\eta_R)\right]_3 +$$

$$\frac{P_3}{P_2}\frac{C_{3a}}{C_{2a}}\left[\frac{\bar{R}x}{\sigma}\left.I_2\right|_{\eta_{-R}}^{\eta_R} - \left(\frac{x}{\sigma}\right)^2\cos\theta\left(\left.J_2\right|_{\eta_{-R}}^{\eta_R} - \eta_m \left.I_2\right|_{\eta_{-R}}^{\eta_R}\right)\right]_3 \qquad (II\text{-}23)$$

Algebraically solving for η_m gives:

$$\eta_m = \frac{J_1\Big|_{\eta_j}^{\eta_R} - \dfrac{C_{3a}}{C_{2a}} J_1\Big|_{\eta-R}^{\eta_R}}{I_1\Big|_{\eta_j}^{\eta_R} - \dfrac{C_{3a}}{C_{2a}} I_2\Big|_{\eta-R}^{\eta_R} - \dfrac{\gamma-1}{\gamma}\dfrac{1}{C_{3a}C_{2a}}(1-\dfrac{P_2}{P_3})} - (\dfrac{\overline{\sigma R}}{x\cos\theta})_3 \qquad \text{(II-24)}$$

An inviscid continuity equation may now be written between stations (2) and (3):

$$\int_0^{Y_R} \rho_2 u_2 2\pi R_2 dy = \int_0^{Y_R} \rho_3 u_3 2\pi R_3 dY_3 \qquad \text{(II-25)}$$

Making the appropriate substitutions and algebraically rearranging results in:

$$(R_o y_R - \tfrac{1}{2}\cos\theta y_R^2)_2 = \frac{P_3}{P_2}\frac{C_{3a}}{C_{2a}}\frac{1-C_{2a}^2}{1-C_{3a}^2}\left\{\frac{\overline{Rx}}{\sigma}(\eta_R - \eta_m) - \right.$$

$$\left. (\frac{x}{\sigma})^2\cos\theta\left[\frac{\eta_R^2-\eta_m^2}{2} - \eta_R\eta_m\right]\right\}_3 \qquad \text{(II-26)}$$

Combining both the viscid (II-19) and the inviscid (II-26) continuity equations gives:

$$\frac{\overline{R_3}\sigma_3}{x_3}\frac{2}{\cos\theta_3}(1 - C_{3a}^2)I_1\Big|_{\eta_j}^{\eta_R} - \frac{\overline{R_3}\sigma_3}{x_3}\frac{2}{\cos\theta_3}\eta_R - 2(1 - C_{3a}^2)J_1\Big|_{\eta_j}^{\eta_R} + \eta_R^2 =$$

$$-\eta_m^2 -\eta_m\left[\frac{\overline{R\sigma}}{x}\frac{2}{\cos\theta} - 2\eta_R + 2(1 - C_{3a}^2)\,I_1\Big|_{\eta_j}^{\eta_R}\right]_3 \qquad \text{(II-27)}$$

Recalling the expression for η_m, and defining B as:

$$B = \frac{J_1\Big|_{\eta-R}^{\eta_R} - \dfrac{C_{3a}}{C_{2a}} J_2\Big|_{\eta-R}^{\eta_R}}{I_1\Big|_{\eta_j}^{\eta_R} - \dfrac{C_{3a}}{C_{2a}} I_2\Big|_{\eta-R}^{\eta_R} - \dfrac{\gamma-1}{\gamma}\dfrac{1}{C_{3a}C_{2a}}(1- \dfrac{P_2}{P_3})\eta_R} \qquad \text{(II-28)}$$

then the expression for η_m becomes:

$$\eta_m = B - (\frac{\overline{\sigma R}}{x\cos\theta})_3 \qquad \text{(II-29)}$$

Substituting this result into Equation (II-27) gives:

$$(B-\eta_R)\frac{2}{3} + 2(1-C_{3a}^2)\left[I_1\Big|_{\eta_{-R}}^{\eta_R} - I_1\Big|_{\eta_{-R}}^{\eta_j}\right]B - 2(1-C_{3a}^2)\left[J_1\Big|_{\eta_{-R}}^{\eta_R} - J_1\Big|_{\eta_{-R}}^{\eta_j}\right]=$$

$$(\frac{\sigma\overline{R}}{x\cos\theta})\frac{2}{3} \hspace{4cm} \text{(II-30)}$$

For $\eta_R = 3$, then:

$$\left\{(B-3)\frac{2}{3} + 2(1-C_{3a}^2)\left[I_1\Big|_{-3}^{3} - I_1\Big|_{-3}^{\eta_j}\right]B - 2(1-C_{3a}^2)\left[J_1\Big|_{-3}^{3} - J_1\Big|_{-3}^{\eta_j}\right]\right\}_3 =$$

$$(\frac{\sigma\overline{R}}{x\cos\theta})\frac{2}{3} \hspace{4cm} \text{(II-31)}$$

Thus the location of the j-streamline may be determined by solving this transcendental equation

Calculation Procedure

For a given (or calculated) flow field up to the plug base, the calculation procedure for determining the base pressure is as follows:

1. Estimate the value of the base pressure ratio, P_b/P_{o1}, and knowing P_1 and M_1, obtain the ratio P_b/P_1. (The terms P_1 and M_1 are the pressure and Mach number at the tip of the plug.)

2. $P_b/P_{o1} = P_2/P_{o1}$ because of the assumption of no pressure gradient in the y-direction. The pressure ratio P_2/P_{o1} determines the Mach number M_{2a} and the corresponding Prandtl-Meyer angle, ν_{2a}. The difference in Prandtl-Meyer angles ($\nu_{2a} - \nu_{1a}$) determines the change in streamline angle at the plug base (ie., $\theta_1 - \theta_2 = \nu_{2a} - \nu_{1a}$).

3. Determine a wake radius ratio, r_w/r_b, and perform a method of characteristics solution to a radius, r_w. This determines the Mach number, M_{3a}, at recompression.

4. Determine the location of the j-streamline by iteratively solving Equation (II-31). The value of the jet spread parameter, σ_{3a}, is that formulated by Channapragada.[29] Also, $\theta_{1-2} = \theta_{3-4}$. The solution to this equation is double-valued, and the upper solution is used for external flows.

5. For no bleed, $\phi_d = \phi_j$ and:

$$C_{d3} = \phi_{d3}C_{3a} = \phi_{j3}C_{3a}$$

6. Also:

$$C_{d3} = \left[1 - \frac{1}{(\frac{P_4}{P_3})^{\frac{\gamma-1}{\gamma}}}\right]^{\frac{1}{2}} \text{ since } P_{o3d} = P_4$$

- 58 -

where P_4/P_3 is the pressure rise across an oblique shock of a stream flowing at a velocity M_{3a} deflected through an angle θ_{3-4}.

7. When the value of C_{d3} obtained from steps 5 and 6 agree, a solution is obtained.

REFERENCES

1. Mueller, T.J. and Sule, W.P.: Condensation and Probe Interference Effects on Planar Expansion-Deflection Nozzle Experiments. J. Spacecraft and Rockets, Vol. 6, No. 7, July 1969, pp. 857-859.

2. Lees, L.: Viscous-Inviscid Flow Interactions at Supersonic Speeds. Lecture Series Presented at University of Notre Dame, April 10-11, 1967.

3. Hama, F.R.: Experimental Investigations of Wedge Base Pressure and Lip Shock. Jet Propulsion Laboratory Technical Report No. 32-1003, Dec. 1966, also NASA-CR-81031.

4. O'Brien, R.L.: Laminarization of Nozzle Wall Boundary Layers as a Means of Reducing Heat Flux. AFRPL-TR-65-40, February, 1965.

5. Taylor, D. and Toline, F.R.: Summary of Exhaust Gas Ejector-Diffuser Research. AEDC Technical Report 68-84, October, 1968.

6. Mueller, T.J.; Hall, C.R., Jr.; and Sule, W.P.: Supersonic Wake Flow Visualization. AIAA Journal, Vol. 7, No. 11, November, 1969, pp. 2151-2153.

7. Schlichting, H.: Boundary-Layer Theory. 6th Edition, McGraw-Hill Book Company, New York, 1968.

8. Hall, C.R., Jr.: An Analytical and Experimental Study of Non-Uniform Plug Nozzle Flow Fields. Ph.D. Dissertation, University of Notre Dame, August, 1970.

9. Mueller, T.J. and Hall, C.R., Jr.: Analytical Prediction of the Turbulent Base Pressure in Supersonic Axisymmetric Flow Including the Effect of Initial Flow Direction. AFFDL-TR-68-132, Air Force Flight Dynamics Laboratory, (AFSC), September, 1968.

10. Zumwalt, G.W.: Analytical and Experimental Study of the Axially-Symmetric Supersonic Base Pressure Problem, Ph.D. Dissertation, Department of Mechanical Engineering, University of Illinois, Urbana, Illinois, 1959. (MIC 59-4589, University Microfilms, Inc., Ann Arbor, Michigan.)

11. Zumwalt, G.W. and Tang, H.H.: Transient Base Pressure Study of an Axisymmetric Missile Flying Head-On Through a Blast Wave, Research Report SBW-6, School of Mechanical Engineering, Oklahoma State University, February, 1964.

12. Mueller, T.J. and Chin, Y.T.: Base Pressure Analysis for Annular Plug Nozzles, Report No. D210889-9, United Aircraft Research Laboratory, East Hartford, Connecticut, February 1965.

13. Mueller, T.J.: Determination of the Turbulent Base Pressure in Supersonic Axisymmetric Flow, Journal of Spacecraft and Rockets, Vol. 5, No. 1, pp. 101-107, January, 1968.

14. Korst, H.H.: Chow, W.L. and Zumwalt, G.W.: Research on Transonic and Supersonic Flow of a Real Fluid at Abrupt Increases in Cross Section (With Special Consideration of Base Drag Problems), ME Technical Report No. 392-5, University of Illinois, Urbana, Illinois, October, 1964.

15. Chapman, D.R.: An Analysis of Base Pressure at Supersonic Velocities and Comparison with Experiment, NACA TR 1051, 1951.

16. Channapragada, R.S.: Compressible Jet Spread Parameter for Mixing Zone Analyses, AIAA Journal, Technical Note, Vol. 1, No. 9, pp. 2188-2190, September, 1963.

17. Ames Research Staff: Equations, Tables, and Charts for Compressible Flow, NACA TR 1135, 1953.

18. Golik, R.J.: On Dissipative Mechanisms Within Separated Flow Regions (With Special Consideration to Energy Transfer Across Turbulent, Compressible, $P_r = 1$, Mixing Regions), Ph.D. Dissertation, University of Illinois, Urbana, Illinois, 1962.

19. Hill, W.G.: Initial Development of Compressible Turbulent Free Shear Layers, Ph.D. Dissertation, Rutgers – The State University, New Brunswick, New Jersey, May, 1966.

20. Carriere, P. and Sirieix, M.: Facteurs d'Influence du Recollement d'un Ecoulement Supersonique, Proc. of the 10th International Congress of Applied Mechanics, Stresa, 1960.

21. Shapiro, A.H.: The Dynamics and Thermodynamics of Compressible Fluid Flow, Vol. II, Ronald Press Company, New York, N. Y., 1954.

22. Hall, C.R., Jr.: Experimental Investigation of the Near Wake of a Planar Expansion-Deflection Nozzle, Masters Thesis, Department of Aerospace and Mechanical Engineering, University of Notre Dame, Notre Dame, Indiana, May, 1967.

23. Nash, J.F.: An Analysis of Two-Dimensional Turbulent Base Flow, Including the Effect of the Approaching Boundary Layer, Report No. 1036, National Physics Laboratory, Aerodynamics Division, July 30, 1962.

24. Carpenter, P.W. and Tabakoff, W.: Survey and Evaluation of Supersonic Base Flow Theories, NASA CR-97129, 1969.

25. Brunell, R.D.: Numerical Solutions for Compressible Flow in Planar Converging-Diverging Ducts. Ph.D. Dissertation, University of Notre Dame, June, 1970.

26.   Hawkins, R. and Trevett, E.G.:   Changes in the Flow at the Base
      of a Bluff Body Due to a Disturbance in its Wake, AGARD Report No.
      539, May, 1966.

27.   Adamson, T.C. and Nicholls, J.A.:   On the Structure of Jets from
      Highly Underexpanded Nozzles into Still Air, Journal of the Aero/
      Space Sciences, Vol. 26, No. 1, pp. 16-24, January, 1959.

28.   McDonald, H.:   An Analysis of the Turbulent Base Pressure Problem
      in Supersonic Axisymmetric Flow, The Aeronautical Quarterly, Vol. XVI,
      pp. 97-121, May, 1965.

29.   McDonald, H. and Hughes, P.F.:   A Correlation of High Subsonic
      Afterbody Drag in the Presence of a Propulsive Jet or Support
      Sting, Journal of Aircraft, Vol. 2, No. 3, pp. 202-207, May-June,
      1965.

30.   Dixon, R.J. and Page, R.H.:   Interdependence of Base Pressure and
      Base Heat Transfer, ARS Journal, No. 12, pp. 1785-1786, December,
      1961.

31.   Conners, J.F.; Cubbison, R.W.; and Mitchell, G.A.:   Annular Internal-
      External-Expansion Rocket Nozzles for Large Booster Applications,
      NASA TN D-1049, September, 1961.

32.   Lee, C.C. and Inman, S.J.:   Numerical Analysis of Plug Nozzles
      by the Method of Characteristics, Technical Note No. R-101, Brown
      Engineering Company, Inc., Huntsville, Alabama, May, 1964.

33.   Love, E.S.; Grigsby, C.E.; Lee, L.P. and Woodling, M.J.:   Experi-
      mental and Theoretical Studies of Axisymmetric Free Jets, NASA TR R-6,
      1959.

34.   Vick, A.R.; Andrews, E.H.; Dennard, J.S. and Craidon, C.B.:   Com-
      parisons of Experimental Free-Jet Boundaries with Theoretical
      Results Obtained with the Method of Characteristics, NASA TN D-2327,
      June, 1964.

35.   Reis, R.J.; Aucoin, P.J. and Stechman, R.C.:   The Prediction of
      Rocket Exhaust Flow Fields with Embedded Shocks and Nozzle Boundary
      Layers, AIAA Paper No. 69-569, Presented at the AIAA 5th Propulsion
      Joint Specialist Conference, U.S. Air Force Academy, Colorado,
      June 9-13, 1969.

36.   Farmer, R.C.; Prozan, R.J.; McGimsey, L.R. and Ratliff, A.W.:
      Verification of a Mathematical Model which Represents Large, Liquid
      Rocket-Engine Exhaust Plumes, AIAA Paper No. 66-650, Presented at
      the AIAA Second Propulsion Joint Specialist Conference, Colorado
      Springs, Colorado, June 13-17, 1966.

37. Collins, D.J.; Lees, L. and Roshko, A.: Near Wake of a Hypersonic Blunt Body with Mass Addition, AIAA Journal, Vol. 8, No. 5, pp. 833-842, May, 1970.

38. Mueller, T.J. and Hall, C.R., Jr.: Separated Flow Region Within a Planar Expansion-Deflection Nozzle. Journal of Spacecraft and Rockets, Vol. 5, No. 6, pp. 738-740, June, 1968.

39. Mueller, T.J.: Unpublished Data. United Aircraft Research Laboratory, East Hartford, Connecticut, 1965.

40. Shapiro, A.H.: "The Dynamics and Thermodynamics of Compressible Fluid Flows," Vol. I, Ronald Press Company, New York, New York, 1953.

41. Liepman, H.W. and Roshko, A.: "Elements of Gasdynamics," John Wiley and Sons, Inc., New York, New York, 1963.

TABLE I

Planar Nozzle Contour Coordinates (inches)

X'	Y'	X'	Y'
0.0000	1.3760	2.7000	1.6058
0.1000	1.3760	2.8000	1.6193
0.2000	1.3760	2.9000	1.6328
0.3000	1.3760	3.0000	1.6463
0.4000	1.3760	3.1000	1.6598
0.5000	1.3760	3.2000	1.6733
0.6000	1.3760	3.3000	1.6869
0.7000	1.3760	3.4000	1.7004
0.8000	1.3760	3.5000	1.7139
0.9000	1.3760	3.6000	1.7274
1.0000	1.3760	3.7000	1.7409
1.1000	1.3895	3.8000	1.7544
1.2000	1.4030	3.9000	1.7680
1.3000	1.4165	4.0000	1.7806
1.4000	1.4301	4.1000	1.7854
1.5000	1.4436	4.2000	1.7853
1.6000	1.4571	4.3000	1.7803
1.7000	1.4716	4.4000	1.7703
1.8000	1.4841	4.5000	1.7553
1.9000	1.4976	4.6000	1.7351
2.0000	1.5112	4.7000	1.7095
2.1000	1.5247	4.8000	1.6781
2.2000	1.5382	4.9000	1.6407
2.3000	1.5517	5.0000	1.5969
2.4000	1.5652	5.1000	1.5459
2.5000	1.5787	5.2000	1.4873
2.6000	1.5922	5.2600	1.4481

TABLE II

Planar Nozzle Plug Coordinates (inches)

X'	Y'	X'	Y'
0.0000	0.0000	2.2700	0.4962
0.0700	0.0166	2.3700	0.5180
0.1700	0.0384	2.4700	0.5398
0.2700	0.0602	2.5700	0.5616
0.3700	0.0820	2.6700	0.5834
0.4700	0.1038	2.7700	0.6052
0.5700	0.1256	2.8700	0.6270
0.6700	0.1474	2.9700	0.6488
0.7700	0.1692	3.0700	0.6706
0.8700	0.1910	3.1700	0.6924
0.9700	0.2128	3.2700	0.7135
1.0700	0.2346	3.3700	0.7262
1.1700	0.2564	3.4700	0.7288
1.2700	0.2782	3.5700	0.7213
1.3700	0.3000	3.6700	0.7036
1.4700	0.3218	3.7700	0.6750
1.5700	0.3436	3.8700	0.6346
1.6700	0.3654	3.9700	0.5853
1.7700	0.3872	4.0700	0.5357
1.8700	0.4090	4.1700	0.4872
1.9700	0.4308	4.2700	0.4395
2.0700	0.4526	4.3700	0.3933
2.1700	0.4744		

TABLE III

Coordinates of Planar Nozzle Top Contour Pressure Taps (inches)

Tap Number	Position From Nozzle Inlet
4	1.0620
5	2.2500
6	2.6250
7	3.0620
8	3.8120
9	4.1250
10	4.5000
11	4.9500
12	5.1870
13	5.6250
14	6.0000
15	6.8120
16	7.1250
17	7.4370
18	8.2500
19	8.6250
20	8.9370
21	9.8120
22	10.2500
23	10.6870
24	11.1250
25	11.5620
26	12.0000
27	12.8120
28	13.2500
29	13.6870
30	14.1250
31	14.5620
32	15.0620
33	16.0000
34	16.3750
35	16.8750
36	18.0000

TABLE IV

Coordinates of Planar Nozzle Sidewall Centerline Pressure Taps (inches)

Tap Number	Position From Plug Base
37	0.1600
38	0.4100
39	0.6600
40	0.9100
41	1.1600
42	1.4100
43	1.6600
44	1.9100
45	2.1600
46	2.4100
47	2.6600
48	2.9100
49	3.1600
50	3.4100
51	3.6600
52	3.9100
53	4.1600
54	4.4100
55	4.6600
56	4.9100
57	5.1600
58	5.4100
59	5.6600
60	5.9100
61	6.1600
62	6.4100
63	6.6600
64	6.9100
65	7.1600
66	7.4100
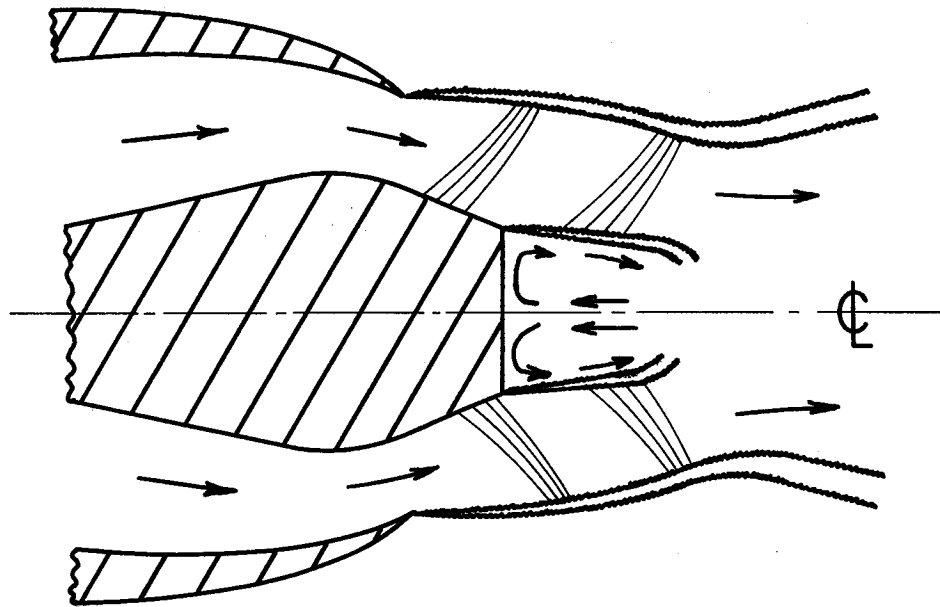
a.) Truncated Plug Nozzle.
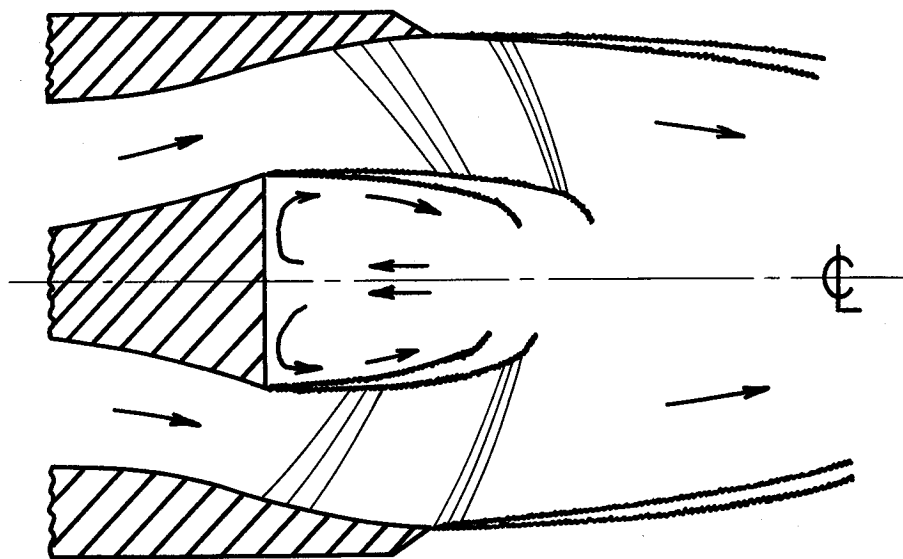
b.) Expansion-Deflection Nozzle.

Fig. 1. Schematic of "Open Wake" Flow Fields for Truncated
Plug and Expansion-Deflection Nozzles.
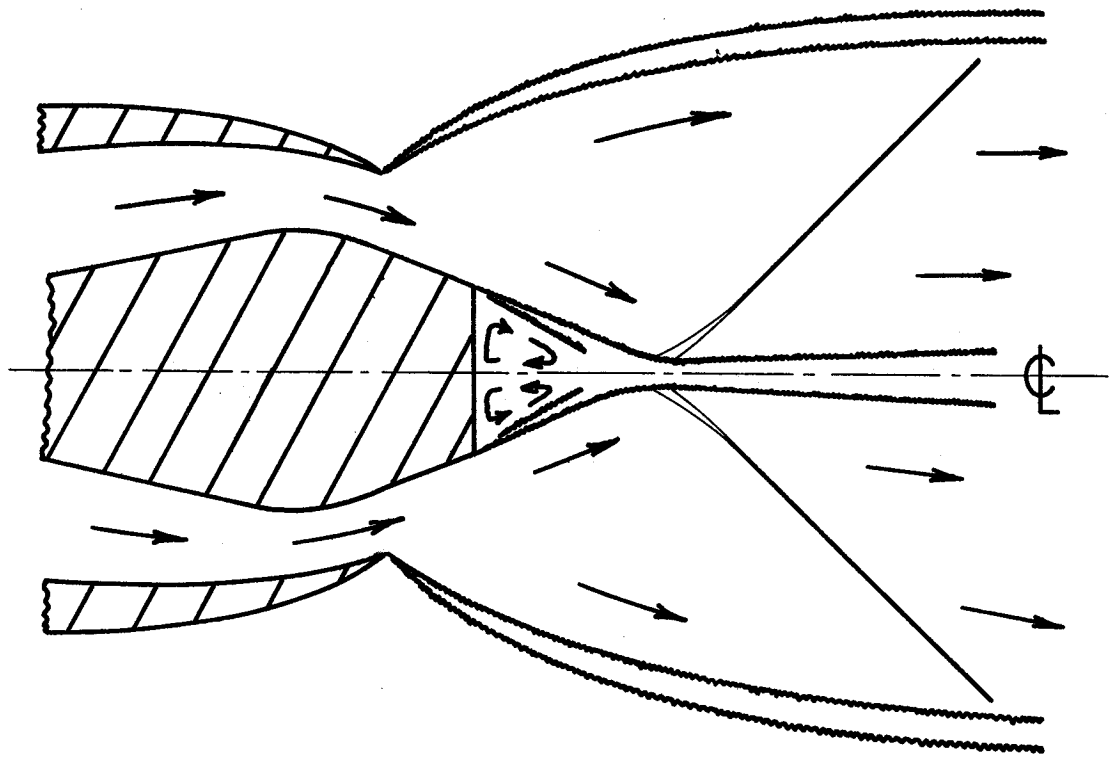
a.)   Truncated Plug Nozzle.
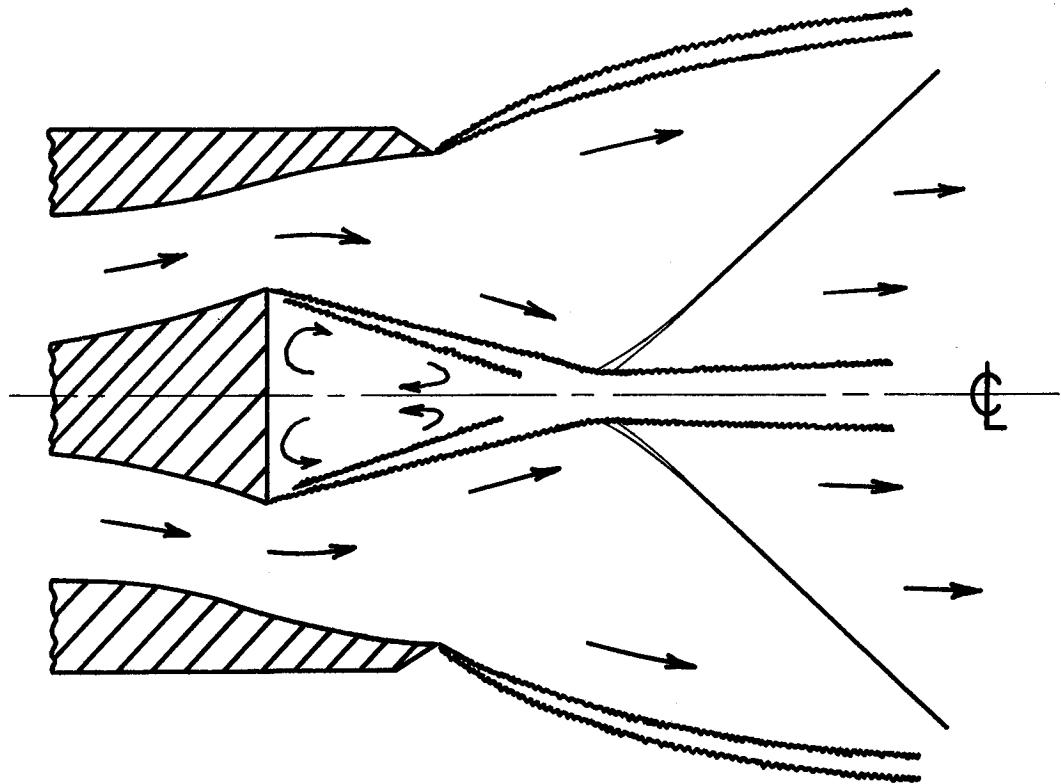
b.)   Expansion-Deflection Nozzle.

Fig. 2.   Schematic of "Closed Wake" Flow Fields for Truncated
Plug and Expansion-Deflection Nozzles.
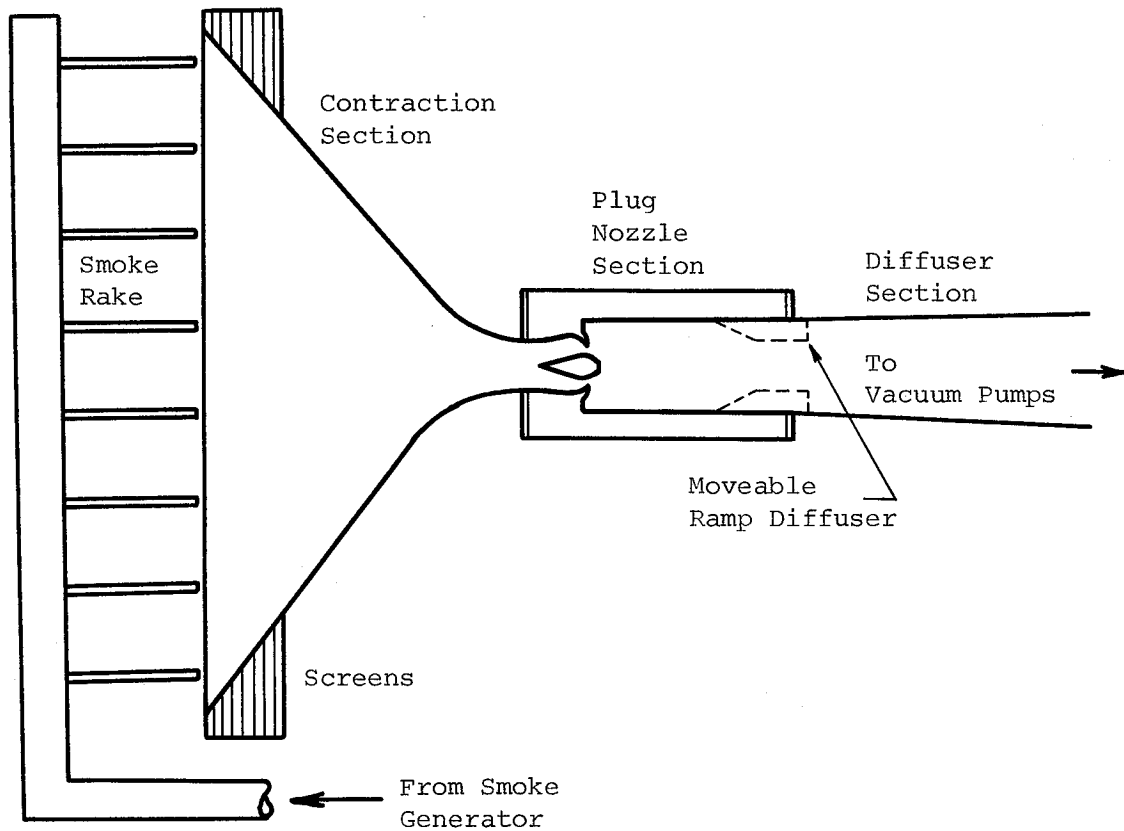
a.) Schematic of Planar Truncated Plug Nozzle Test Facility.
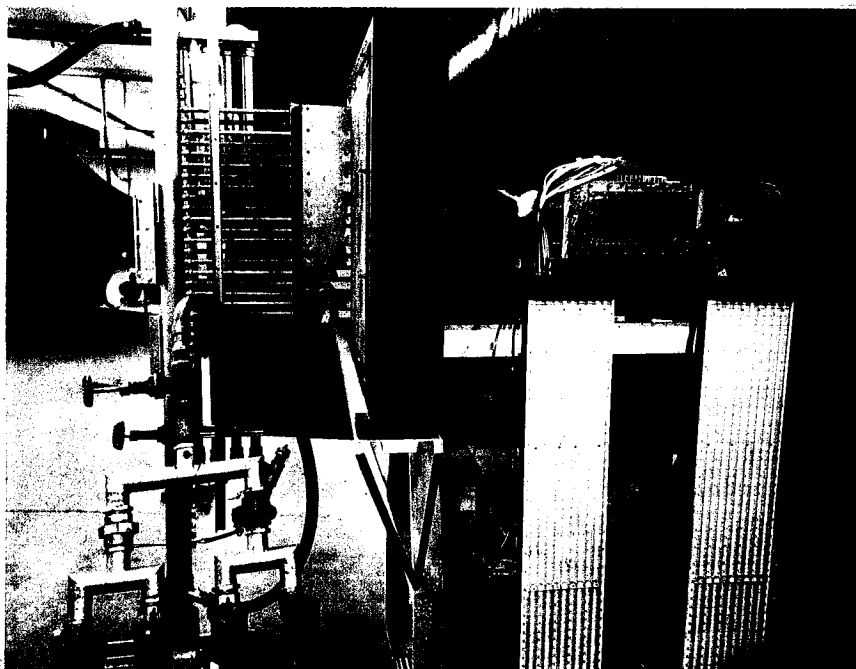
b.) Photograph of Planar Truncated Plug Nozzle Test Facility.

Fig. 3. Planar Truncated Plug Nozzle Test Facility.
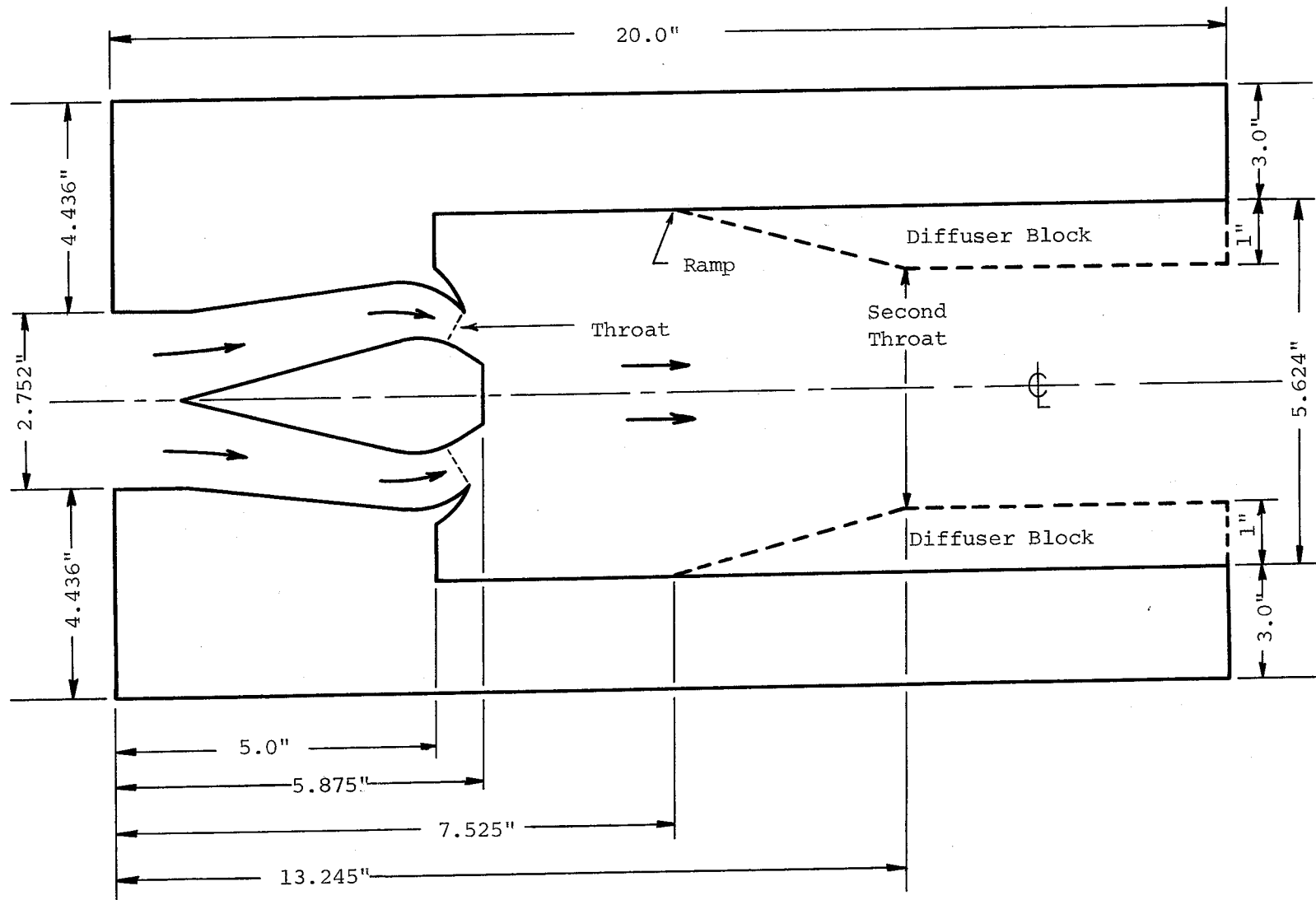
Fig. 4. Plan View of Planar Truncated Plug Nozzle Test Section.

Y'

O

X'

₵

Contour Ends Here
At X' = 5.26"
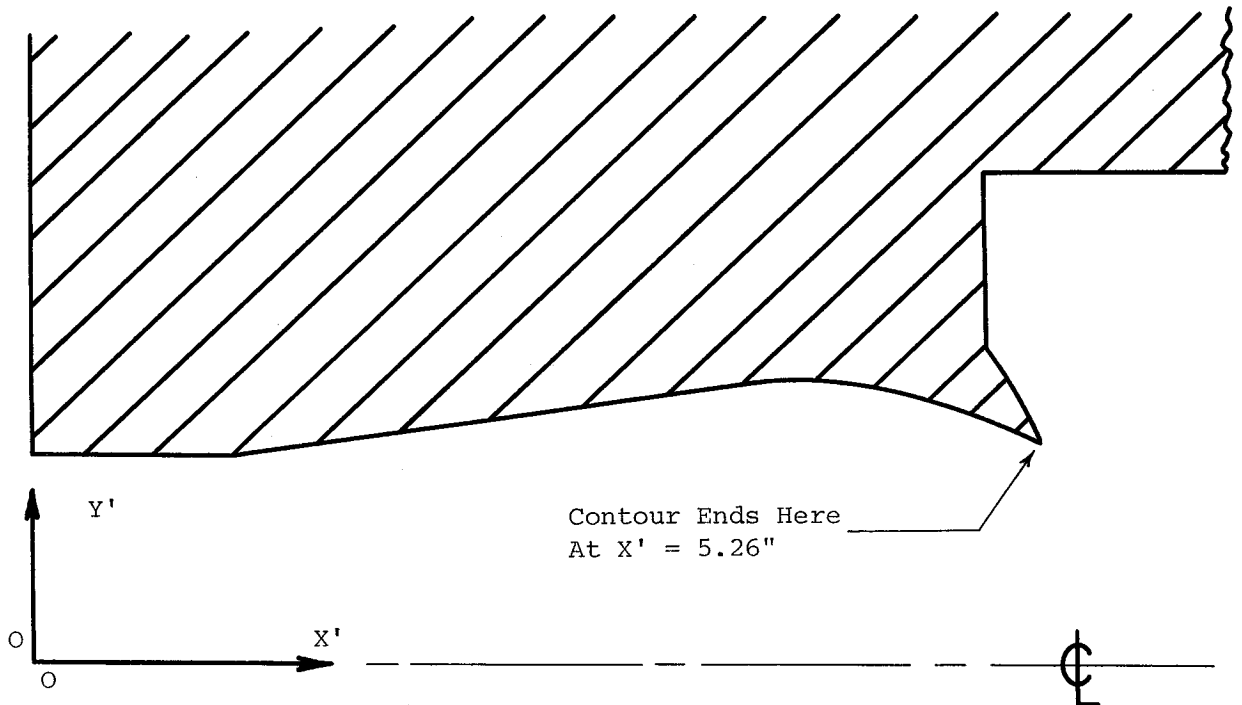
a.) Origin for Nozzle Contour Coordinates.

16% Full Spike

.48"

Y'

O

X'

₵

Mach 2.0
Isentropic Spike
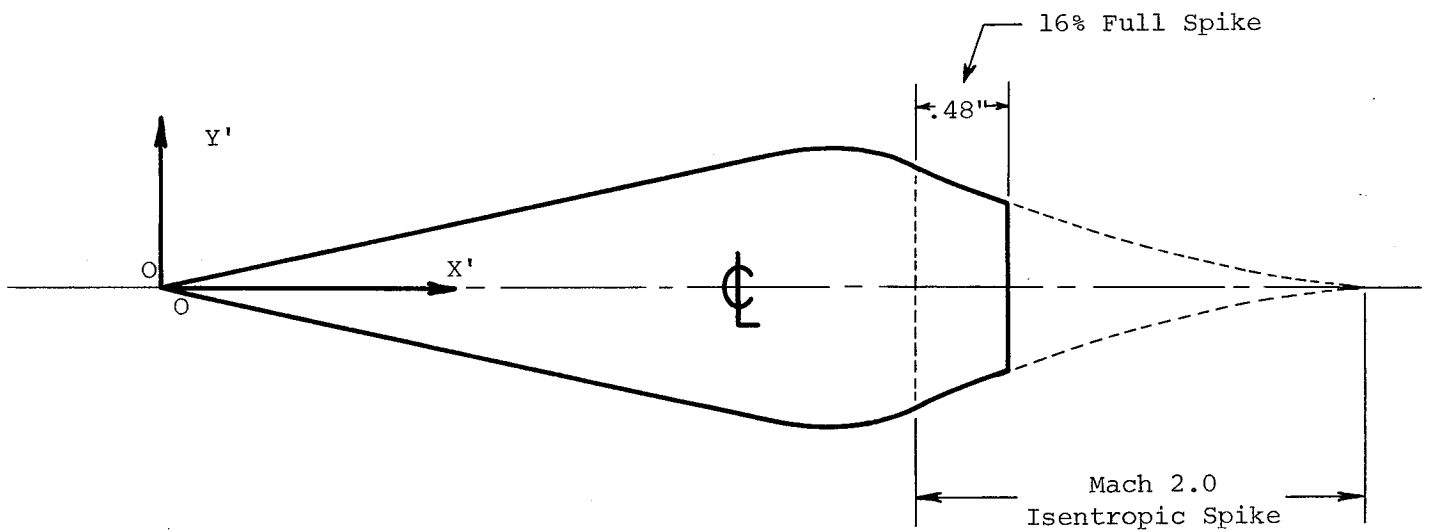
b.) Origin for Plug Coordinates.

Fig. 5. Schematic of Plug and Nozzle Contour Showing Location of
Origins for Coordinate Tabulations.
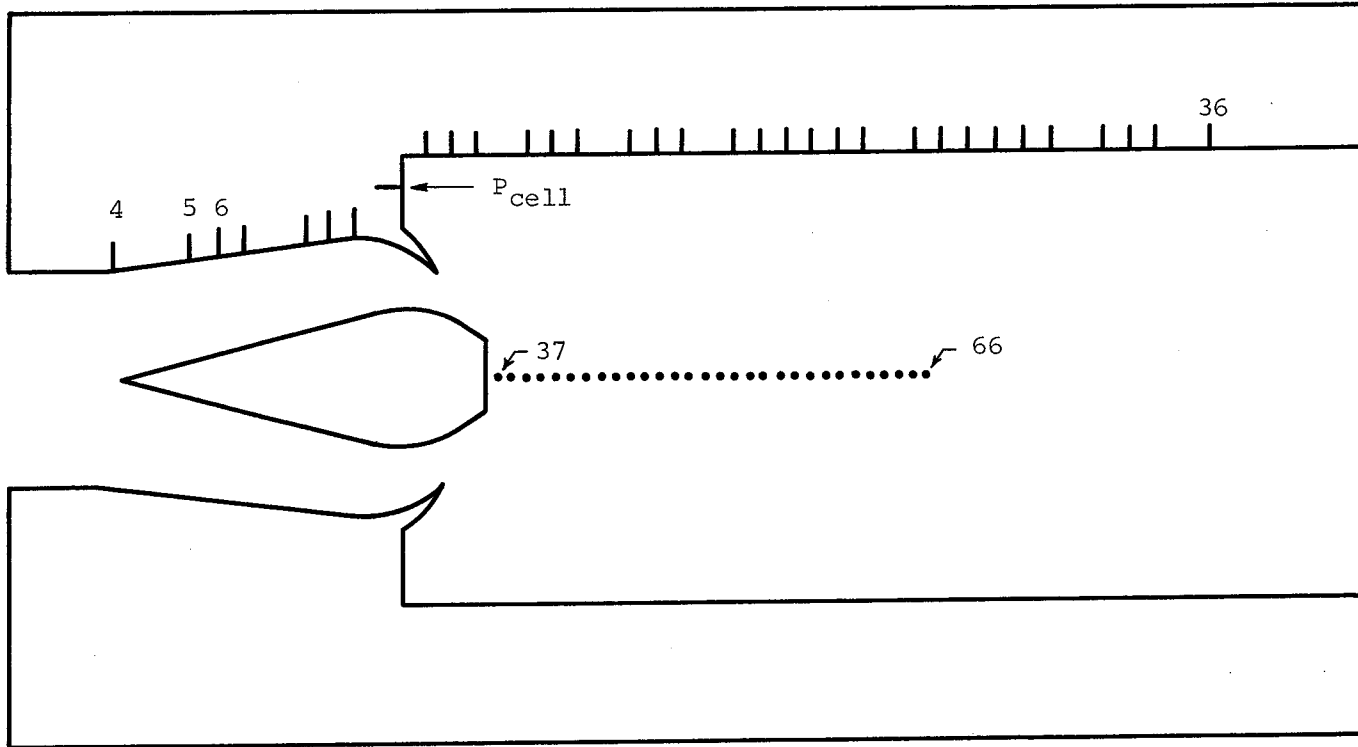
Fig. 6. Relative Location and Numbering System for Static Pressure Taps.

Plug
Base

Static Pressure Orifice

Sliding Tube Probe

Inner, Moveable Hypotube
0.0427" D

Static
Pressure
Orifice

Outer, Fixed Hypotube
0.065" D
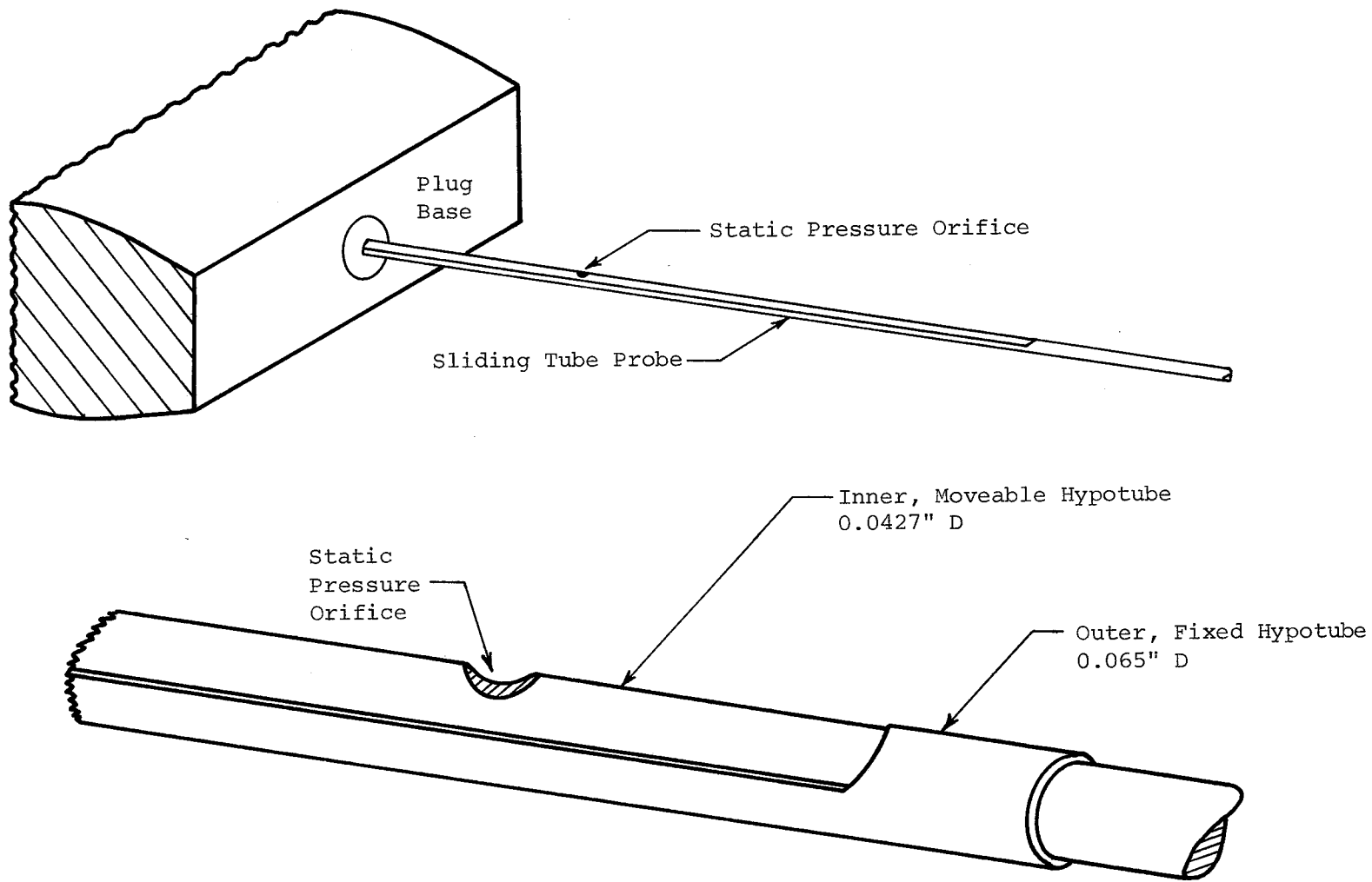
Fig. 7. Schematic of Sliding Tube Static Pressure Probe.
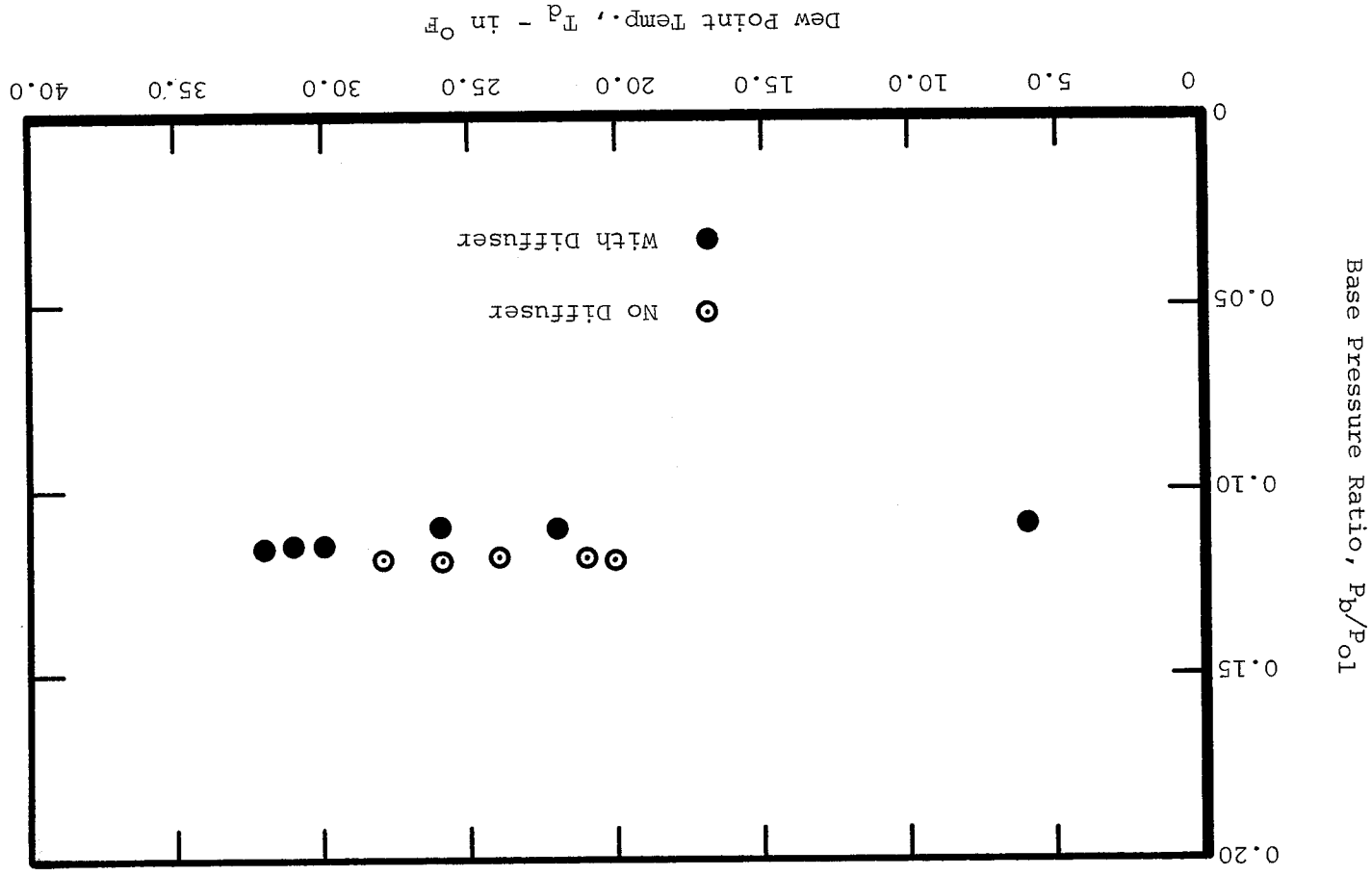
Fig. 8. Effect of Water Vapor Condensation on "Closed Wake" Base Pressure.
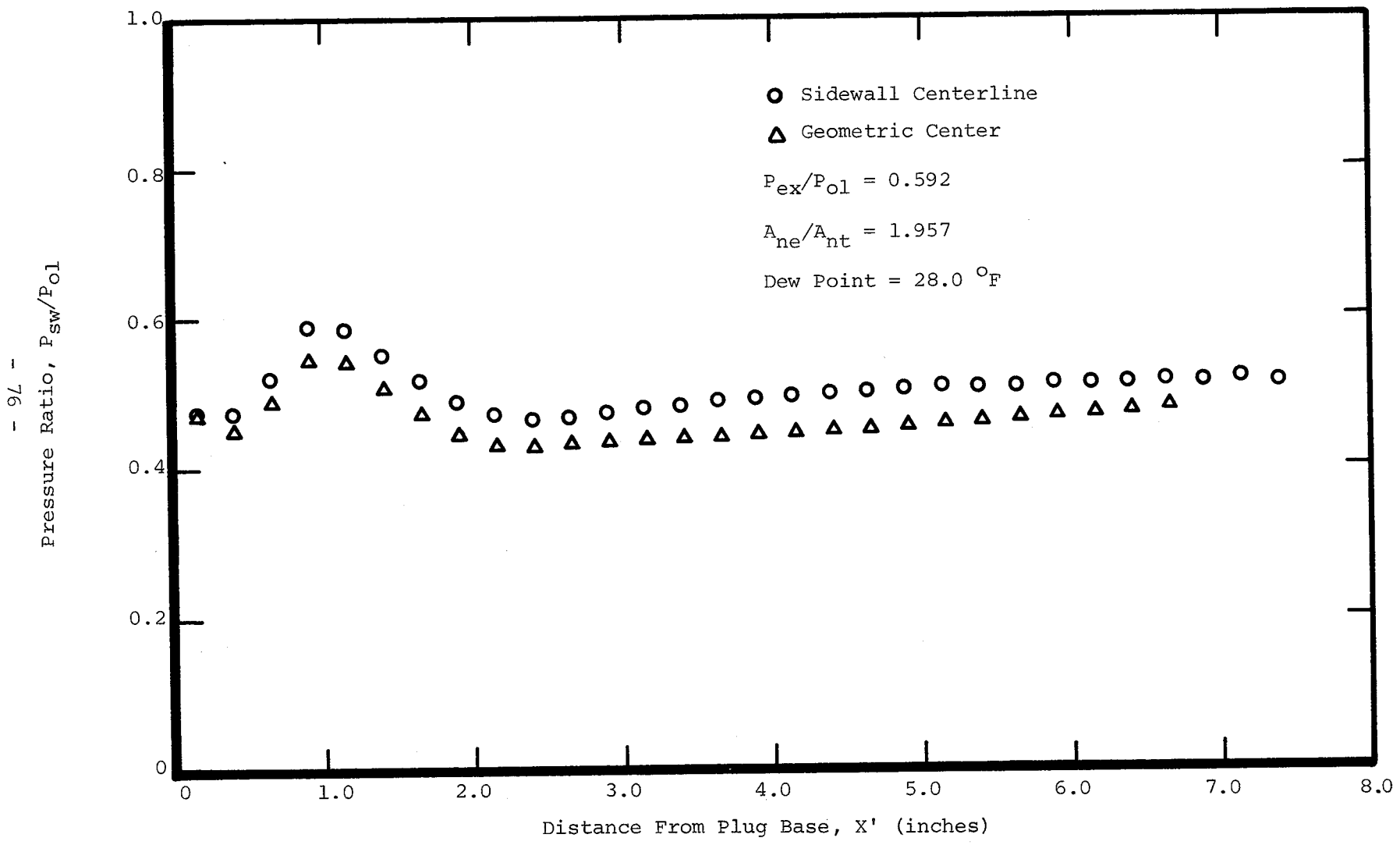
Fig. 9. Comparison of Sidewall Centerline and Geometric Center Static Pressure Distributions ("Open Wake").
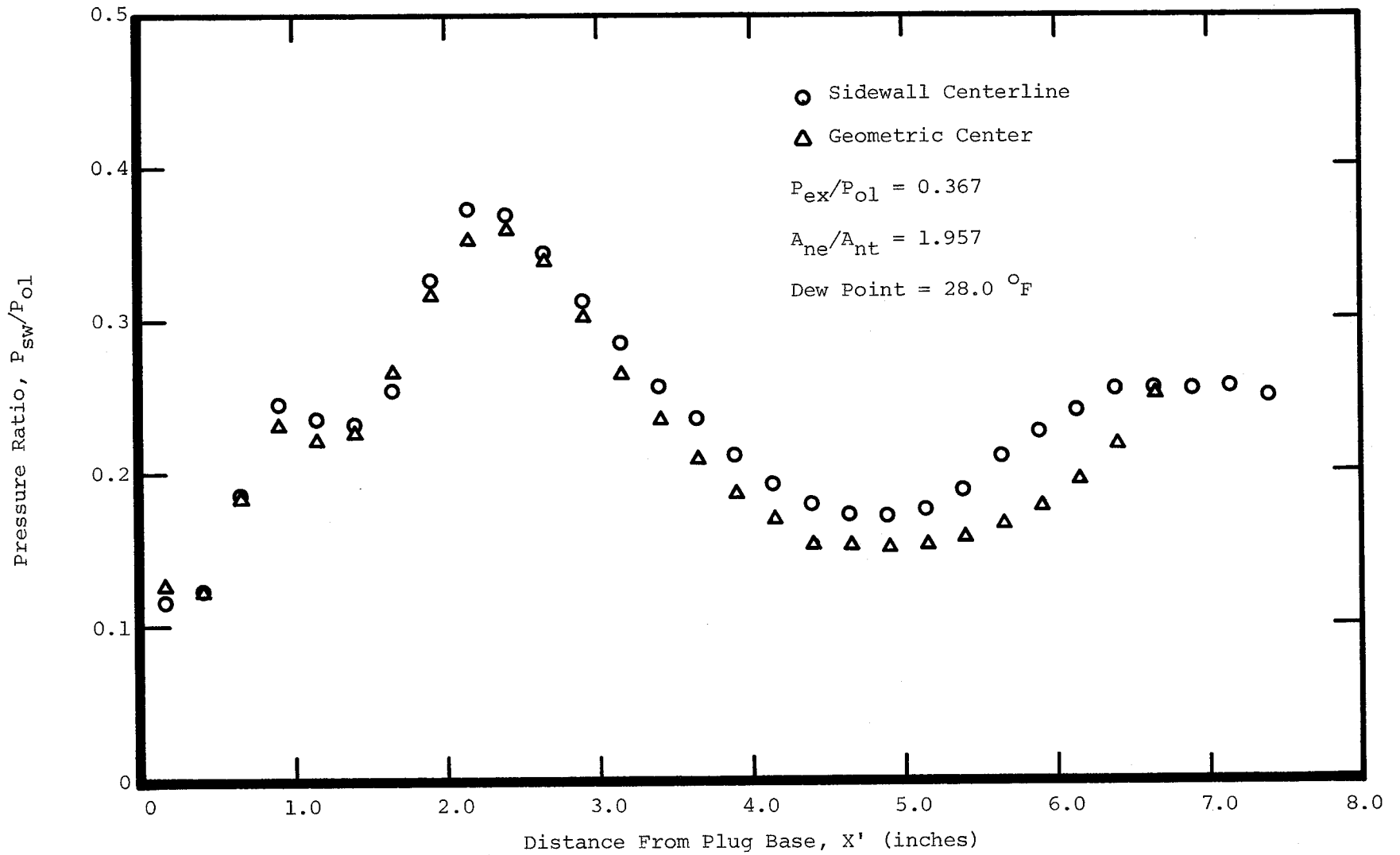
Fig. 10. Comparison of Sidewall Centerline and Geometric Center Static Pressure Distributions ("Closed Wake").
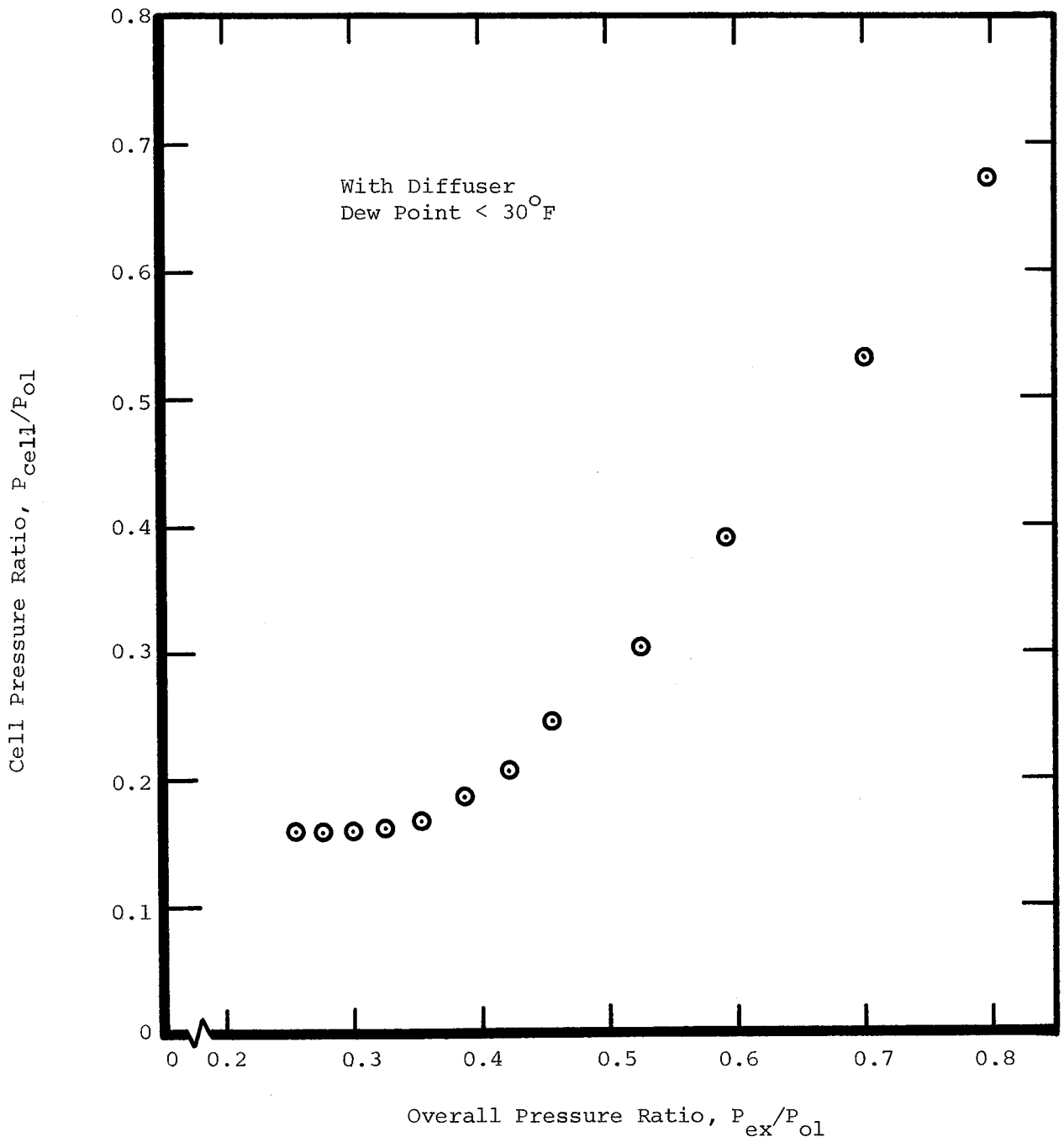
Fig. 11. Planar Truncated Plug Nozzle-Diffuser System Operating
          Characteristics.

No Diffuser
$A_{ne}/A_{nt} = 1.957$

Slope = 1.056

Base Pressure Ratio, P_b/P_{ol}

Cell Pressure Ratio, P_{cell}/P_{ol}
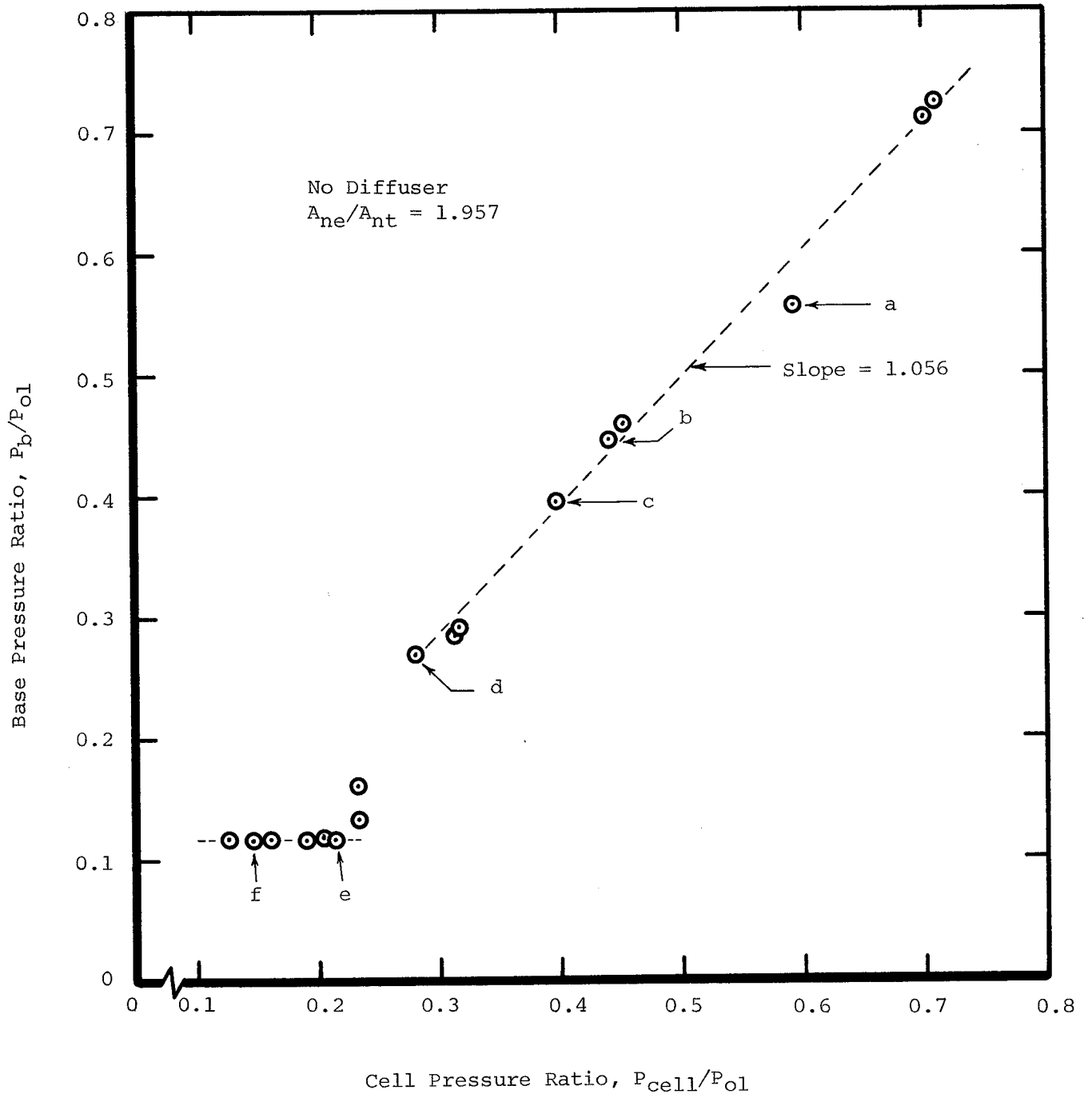
Fig. 12. Variation of Planar Truncated Plug Nozzle Base Pressure Ratio
with Cell Pressure Ratio with No Diffuser.
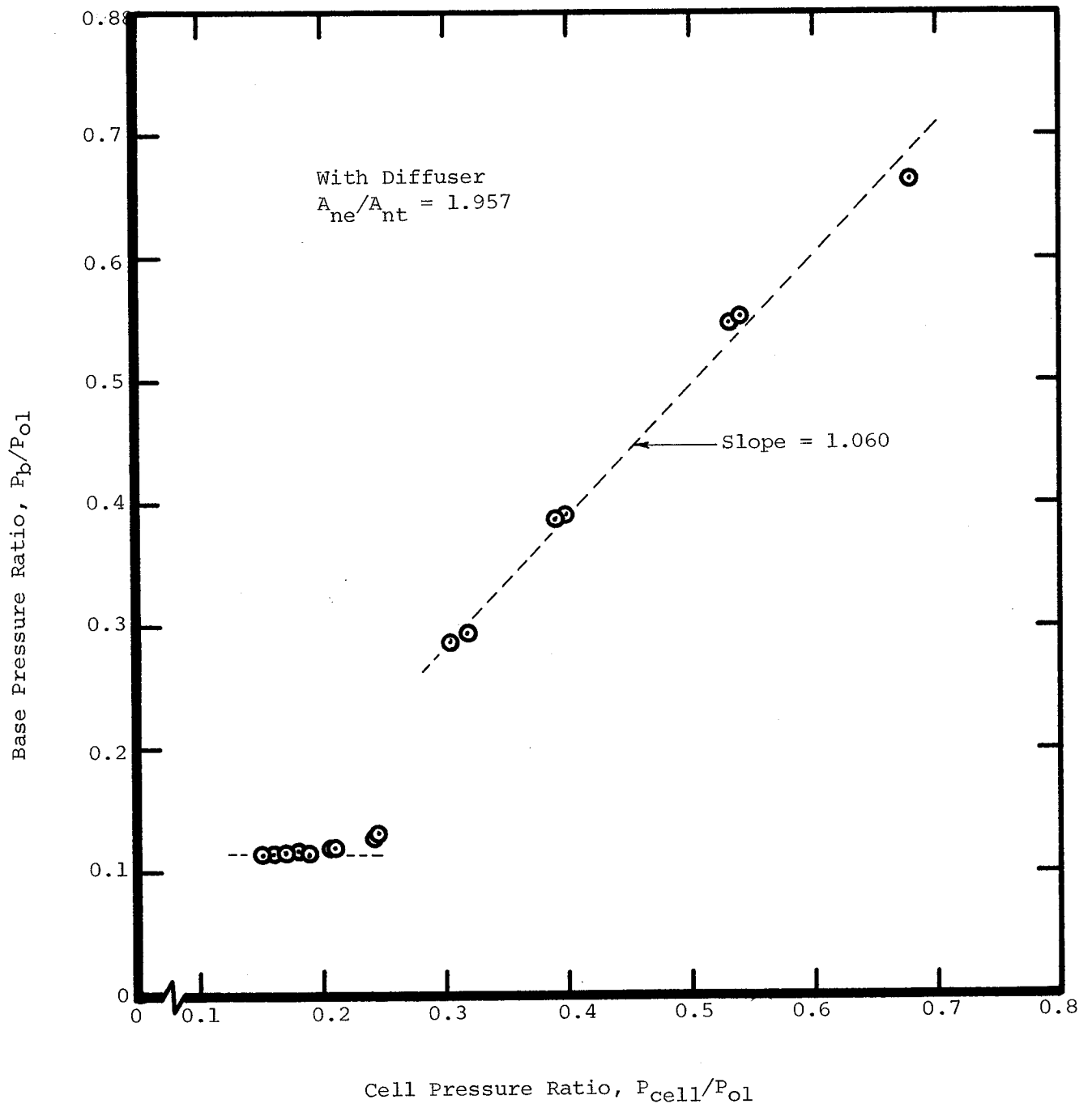
Fig. 13. Variation of Planar Truncated Plug Nozzle Base Pressure Ratio
with Cell Pressure Ratio with Diffuser.
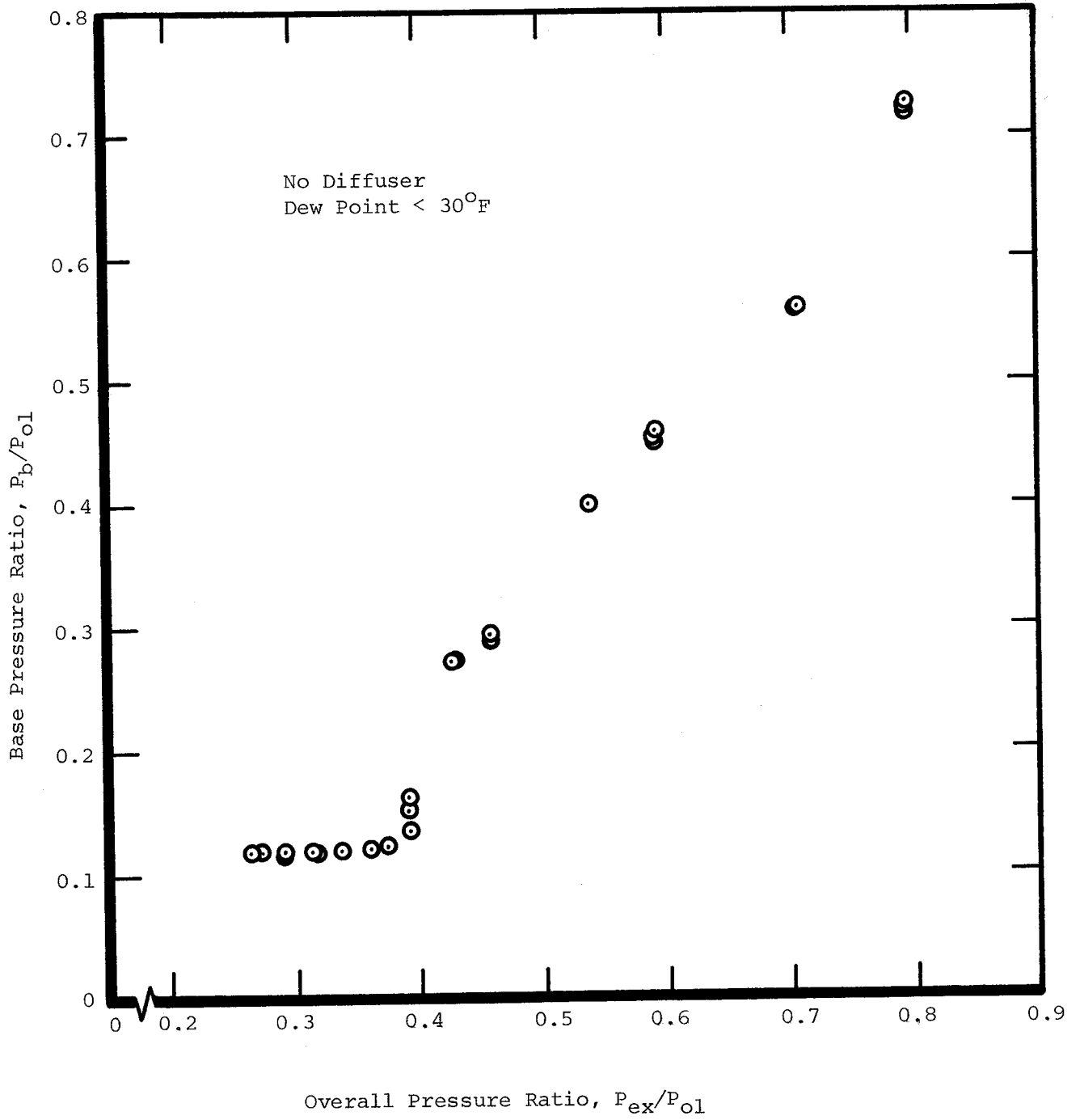
Fig. 14. Planar Truncated Plug Nozzle Base Pressure Characteristics with no Diffuser.
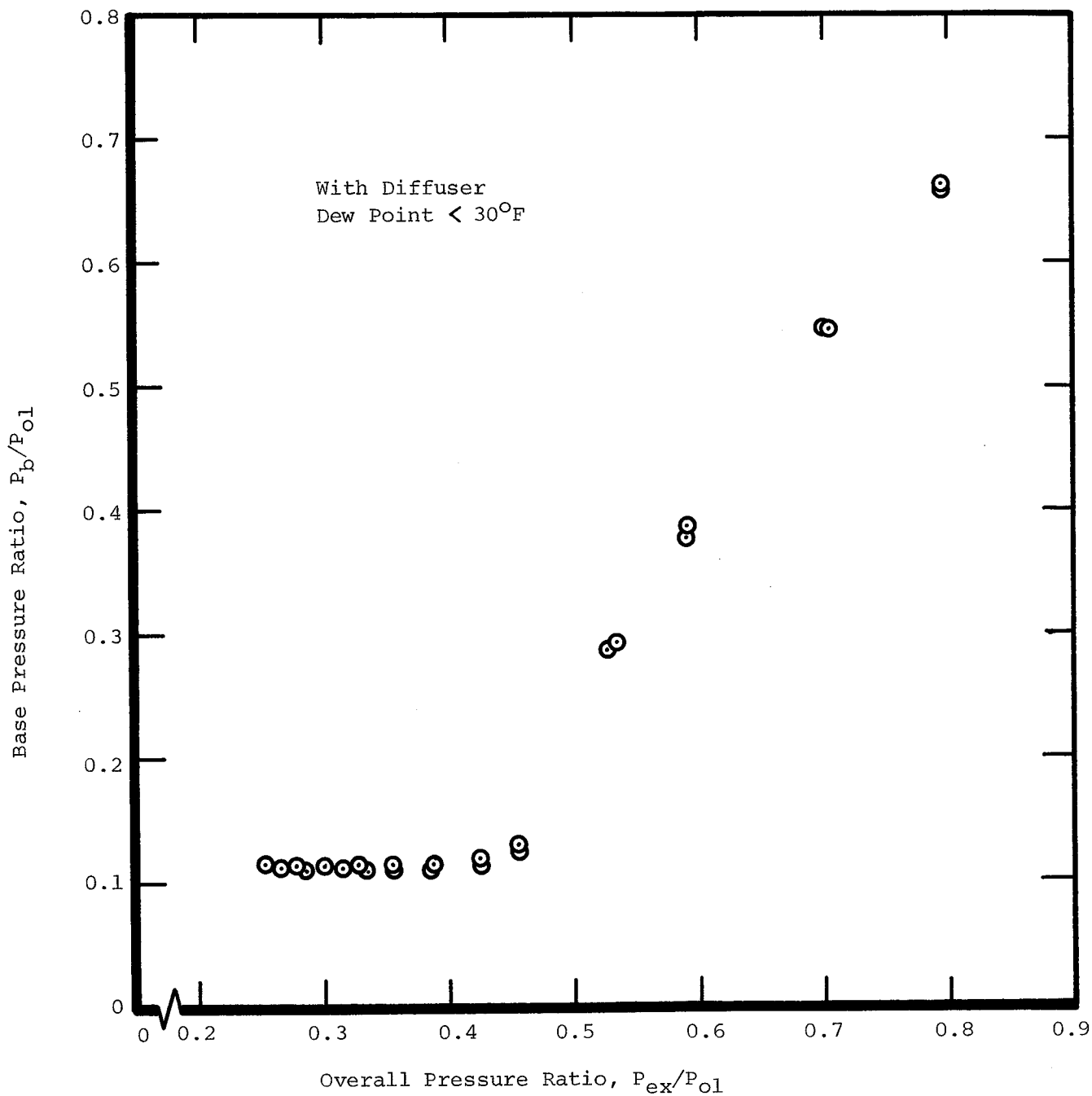
Fig. 15. Planar Truncated Plug Nozzle Base Pressure Characteristics
with Diffuser.
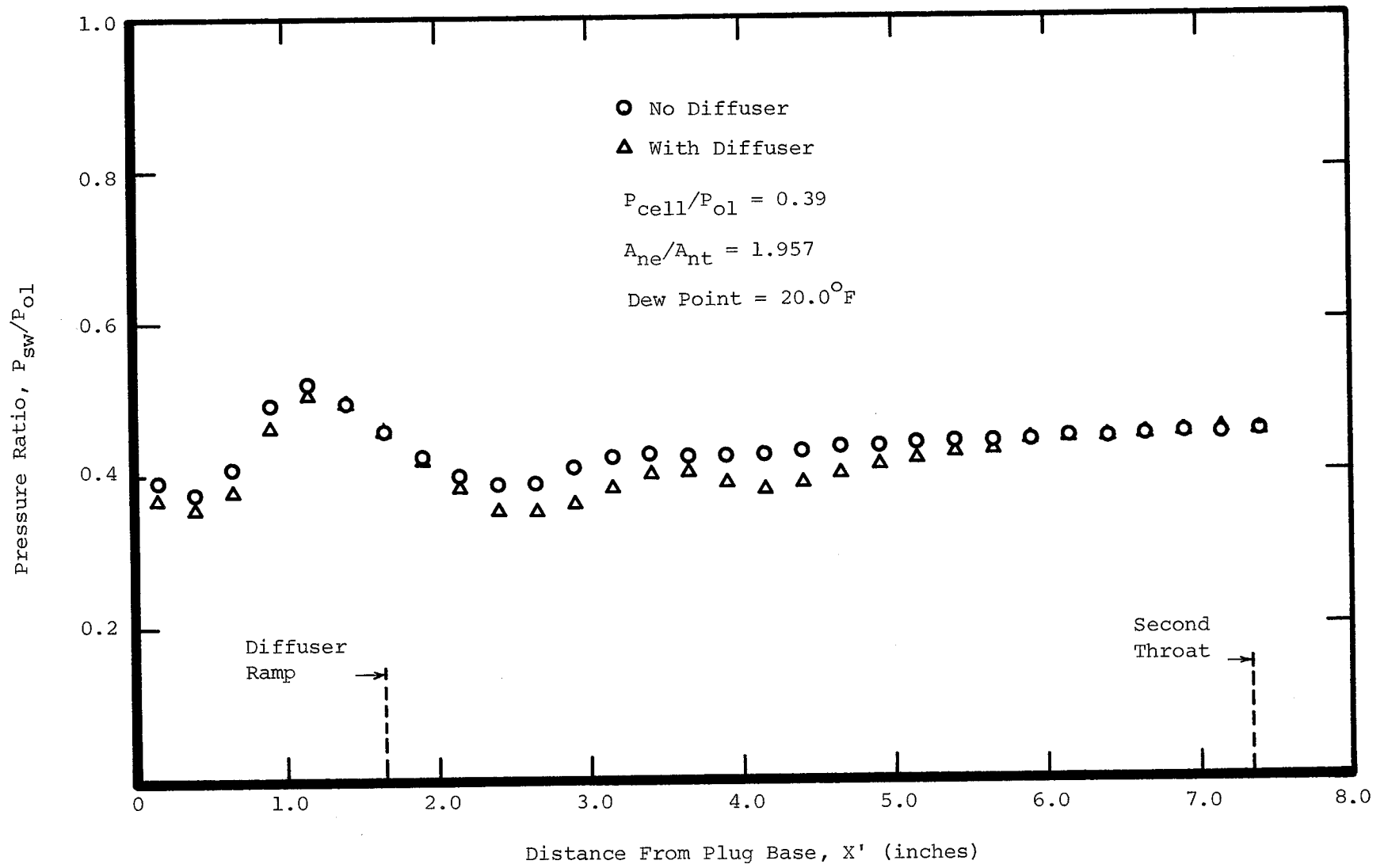
Fig. 16. Diffuser Effect on Sidewall Centerline Static Pressure for "Open Wake" Operation.
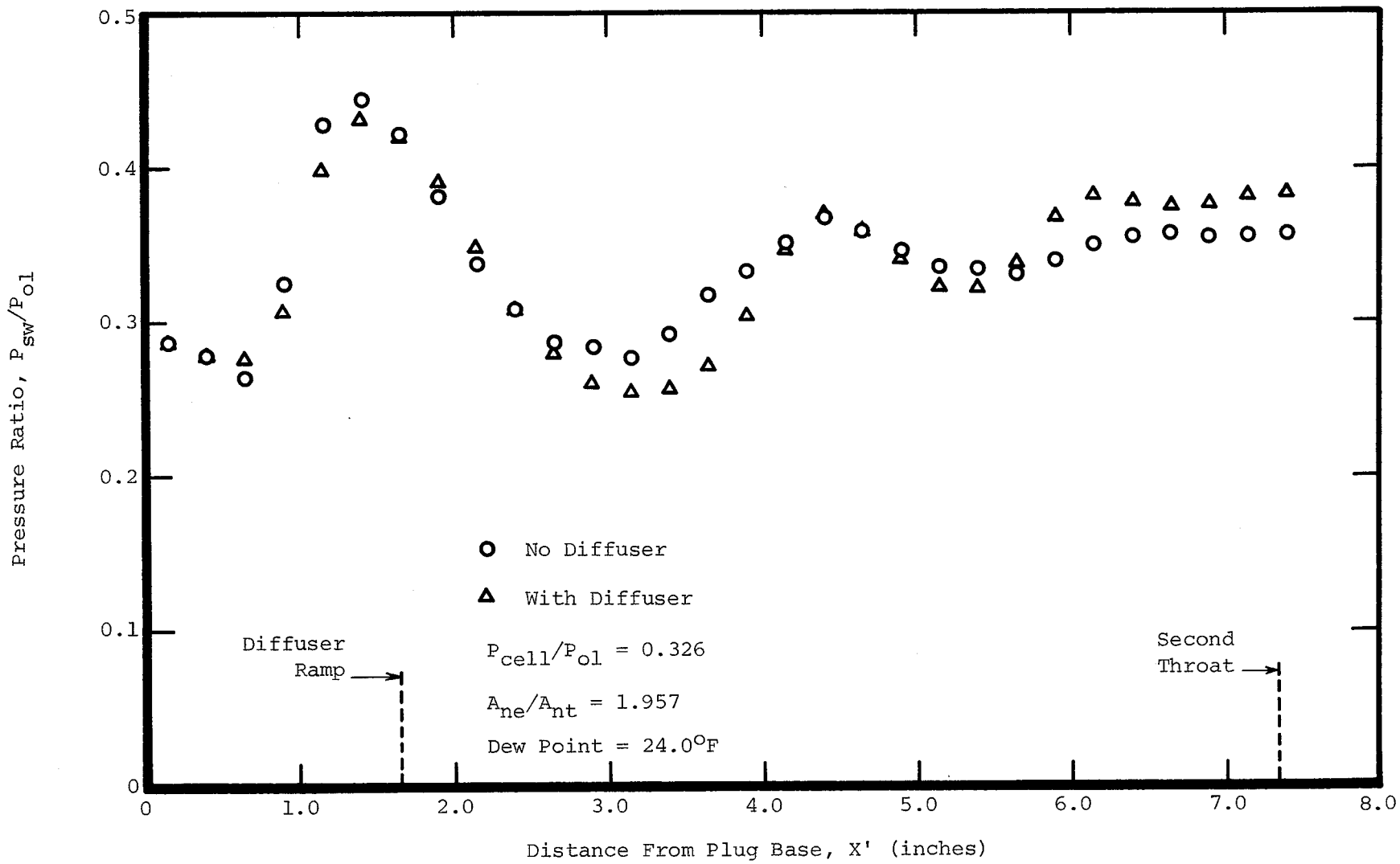
Fig. 17. Diffuser Effect on Sidewall Centerline Static Pressure for "Open Wake" Operation.
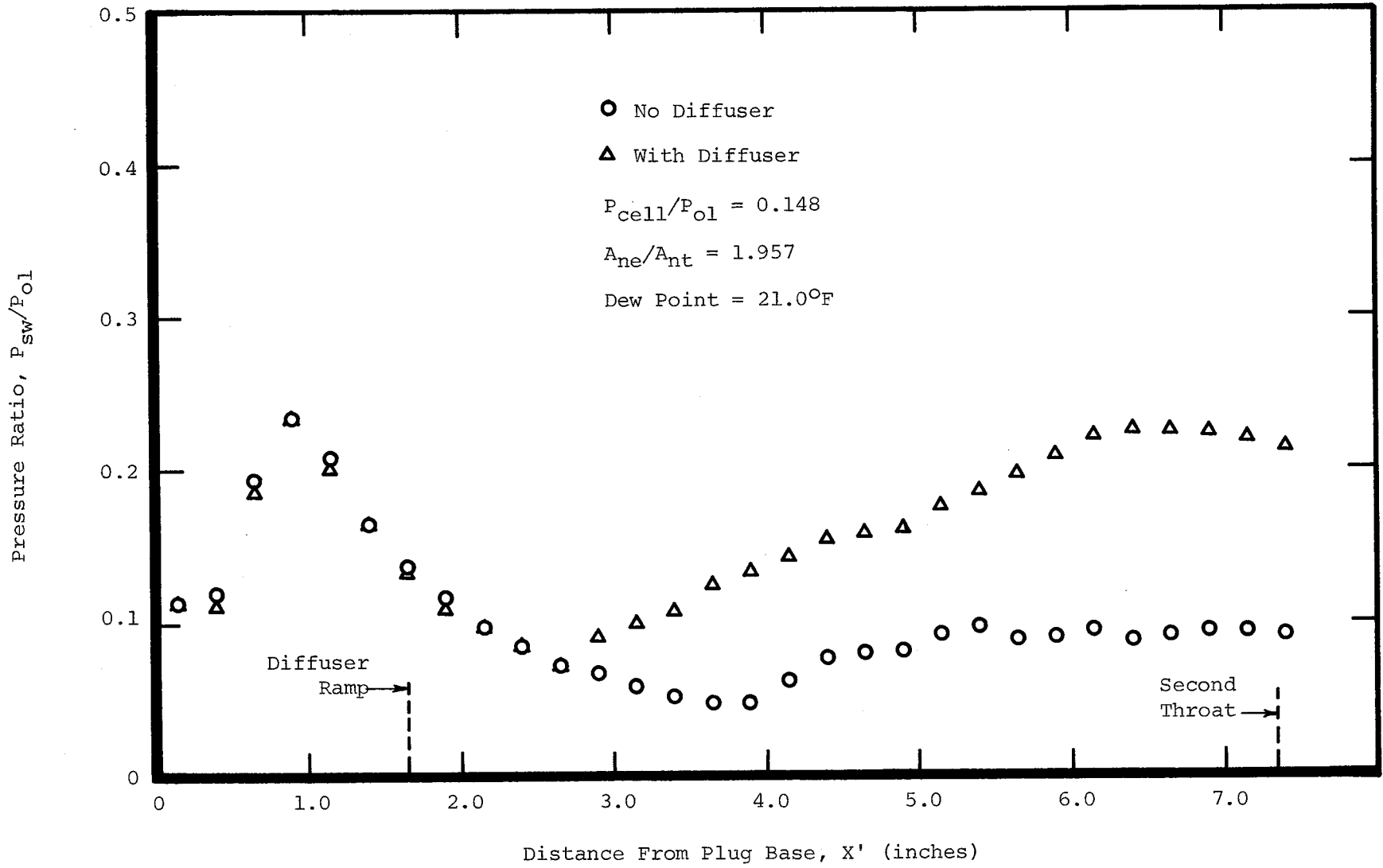
Fig. 18. Diffuser Effect on Sidewall Centerline Static Pressure for "Closed Wake" Operation.
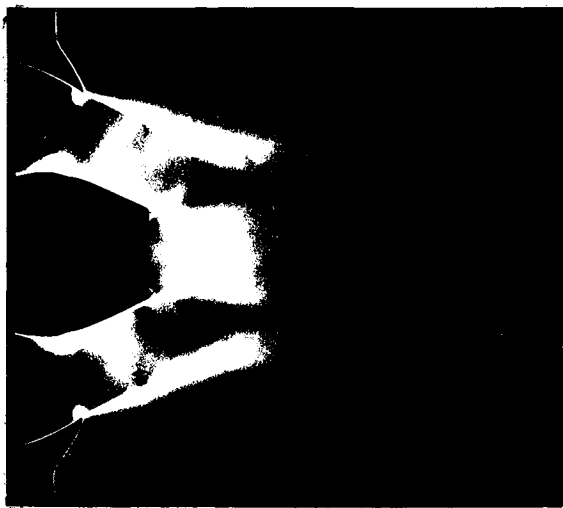
a.) $P_{cell}/P_{ol} = 0.592$
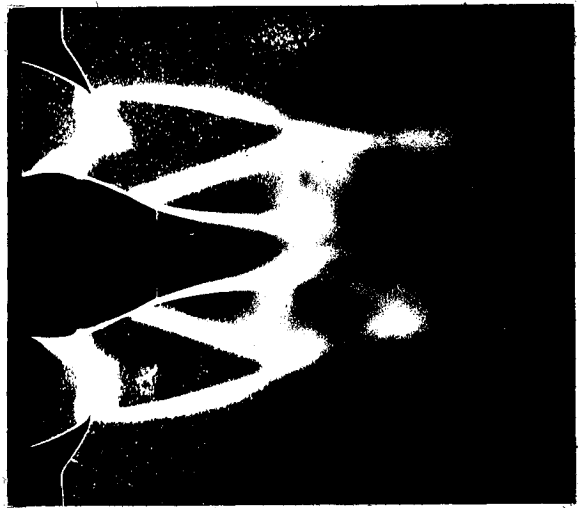
d.) $P_{cell}/P_{ol} = 0.282$

b.) $P_{cell}/P_{ol} = 0.444$

e.) $P_{cell}/P_{ol} = 0.215$

c.) $P_{cell}/P_{ol} = 0.399$
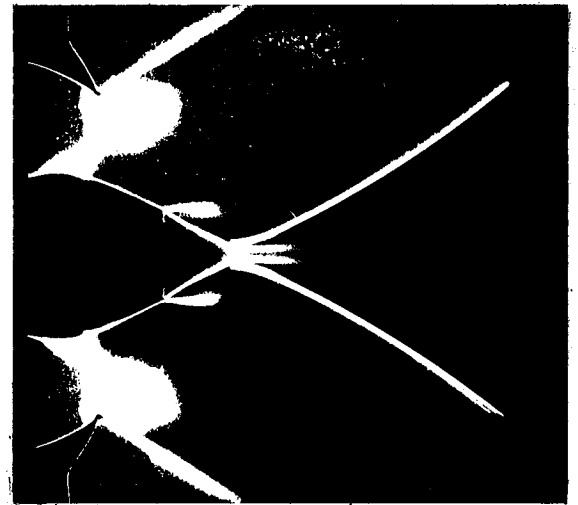
f.) $P_{cell}/P_{ol} = 0.148$

Fig. 19. Schlieren Photographic Sequence for Truncated Plug Nozzle Flow
          Development.
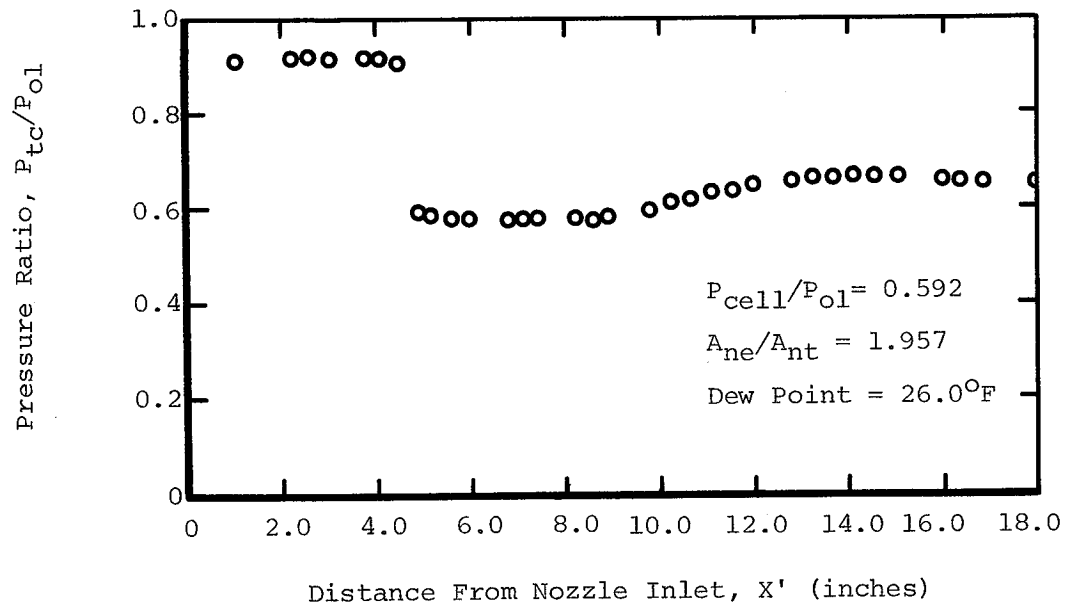
- 86 -

Pressure Ratio, P_{tc}/P_{ol}

Distance From Nozzle Inlet, X' (inches)

$P_{cell}/P_{ol} = 0.592$

$A_{ne}/A_{nt} = 1.957$

Dew Point $= 26.0°F$

a.) Top Contour Static Pressure Variation.

Pressure Ratio, P_{sw}/P_{ol}

Distance From Plug Base, X' (inches)

$P_{cell}/P_{ol} = 0.592$

$A_{ne}/A_{nt} = 1.957$

Dew Point $= 26.0°F$
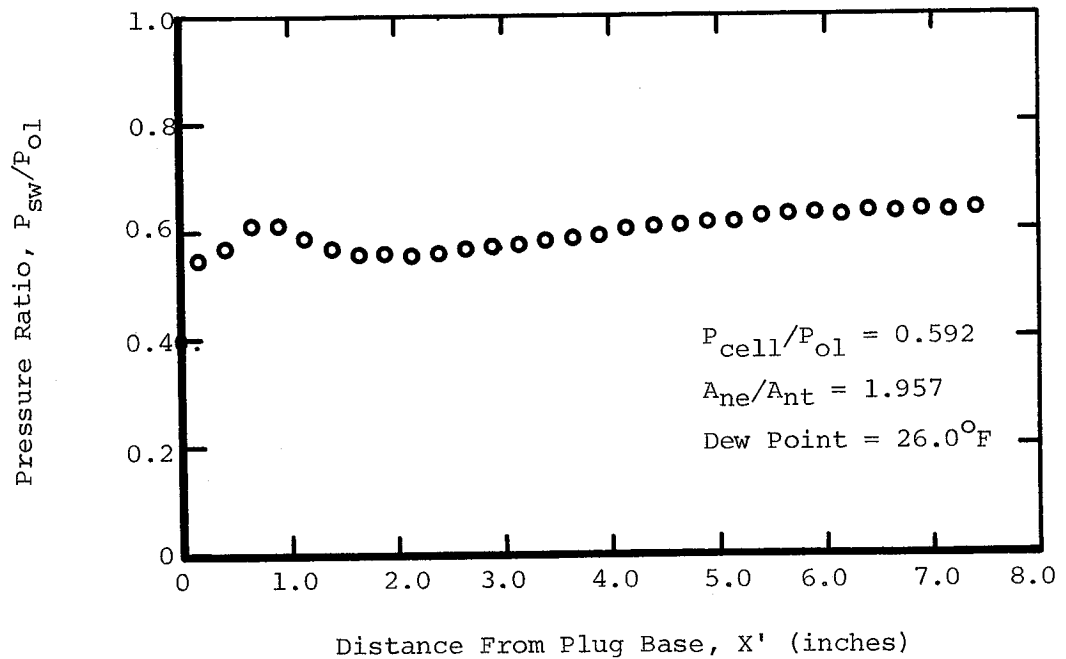
b.) Sidewall Centerline Static Pressure Variation.

Fig. 20. Planar Truncated Plug Nozzle Static Pressure Distributions
Corresponding to Fig. 19a and Point a in Fig. 12.
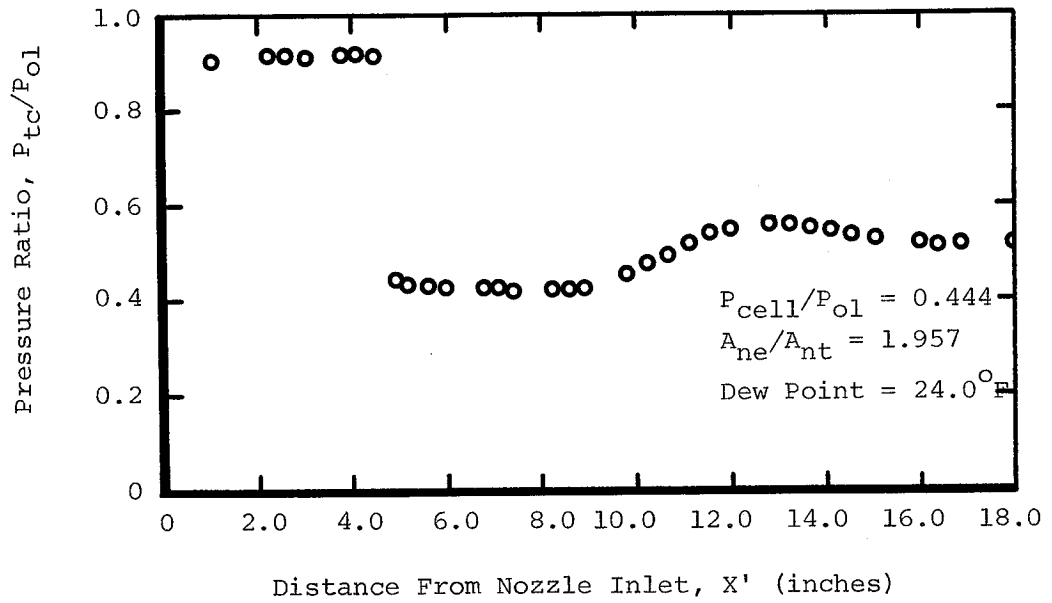
- 87 -

a.) Top Contour Static Pressure Variation.
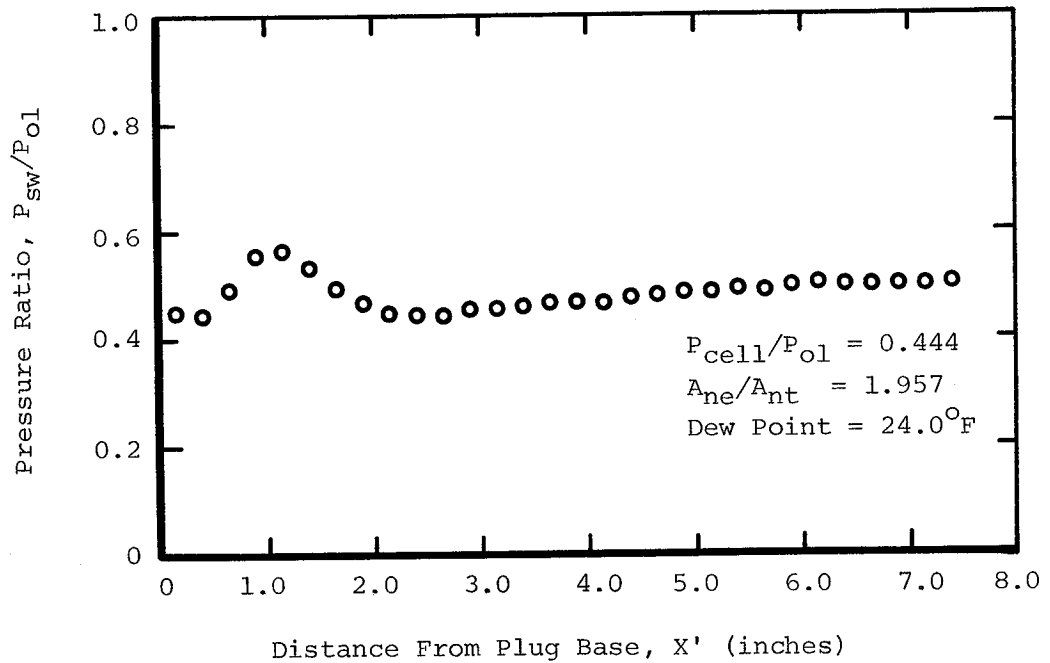
b.) Sidewall Centerline Static Pressure Variation.

Fig. 21. Planar Truncated Plug Nozzle Static Pressure Distributions
Corresponding to Fig. 19b and Point b in Fig. 12.
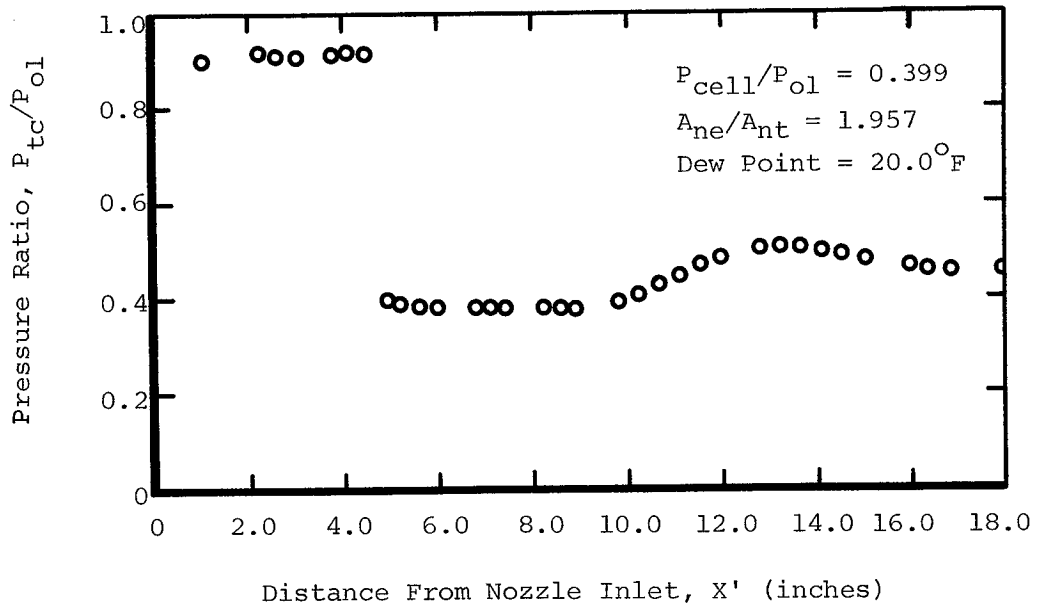
a.) Top Contour Static Pressure Variation.
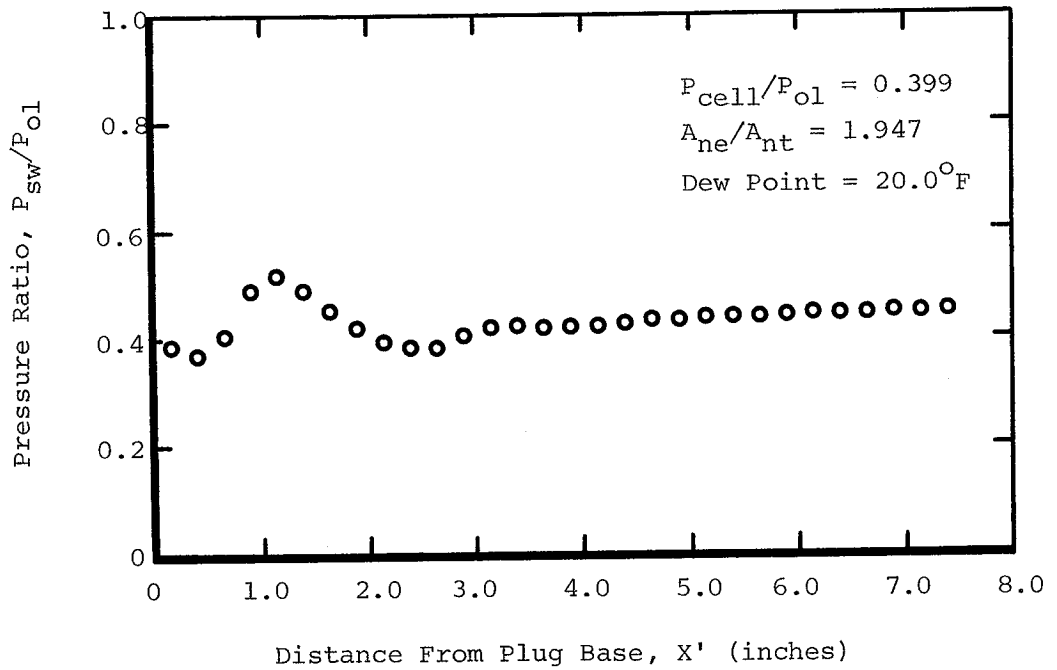
b.) Sidewall Centerline Static Pressure Variation.

Fig. 22. Planar Truncated Plug Nozzle Static Pressure Distributions
Corresponding to Fig. 19c and Point c in Fig. 12.
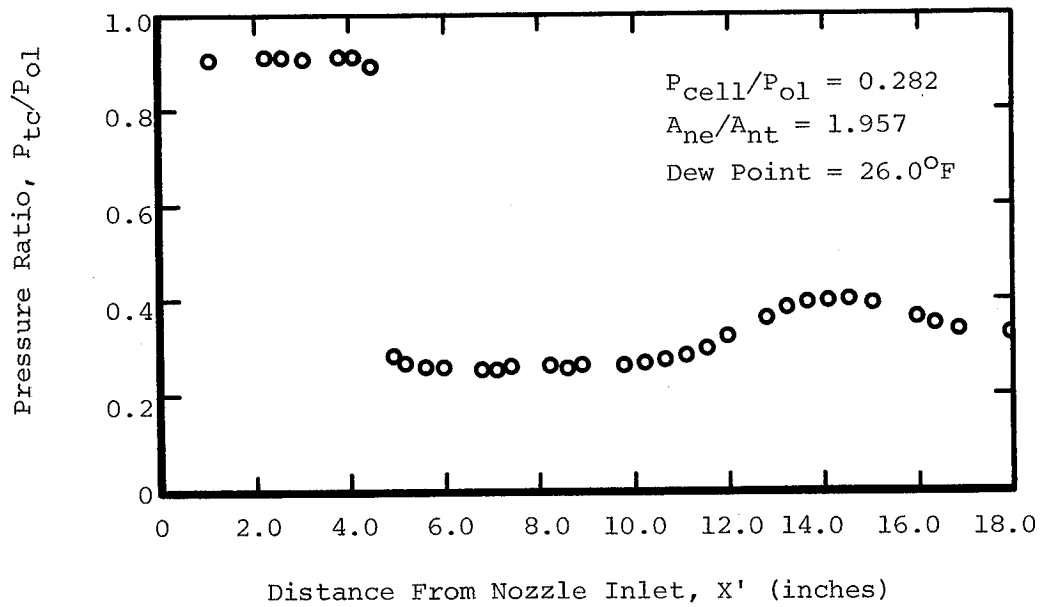
- 89 -

Distance From Nozzle Inlet, X' (inches)

a.) Top Contour Static Pressure Variation.

Distance From Plug Base, X' (inches)
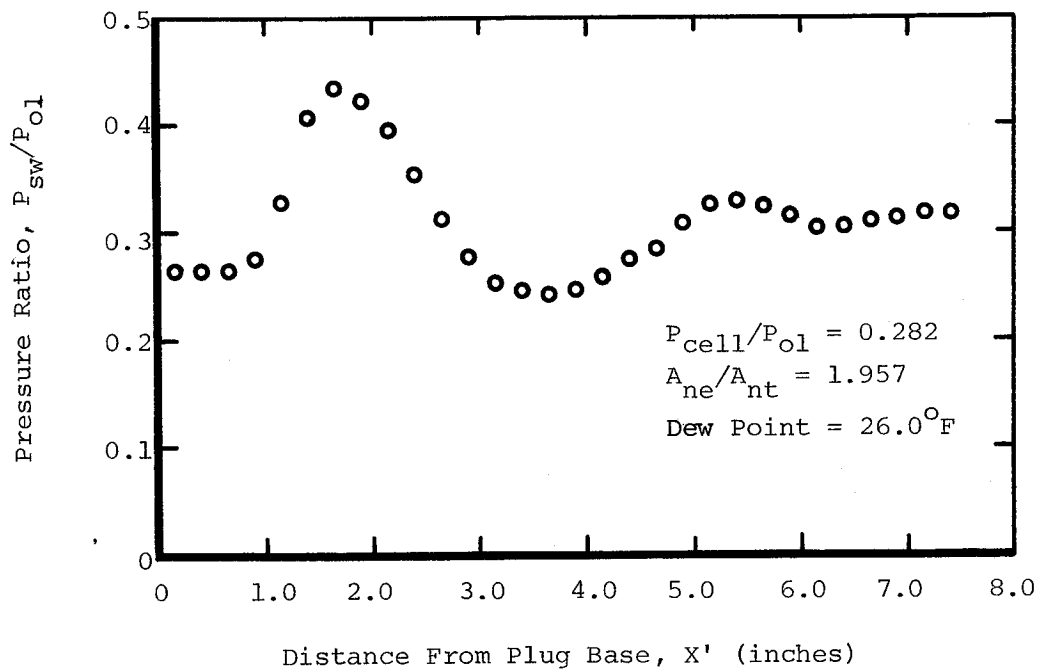
b.) Sidewall Centerline Static Pressure Variation.

Fig. 23. Planar Truncated Plug Nozzle Static Pressure Distributions Corresponding to Fig. 19d and Point d in Fig. 12.
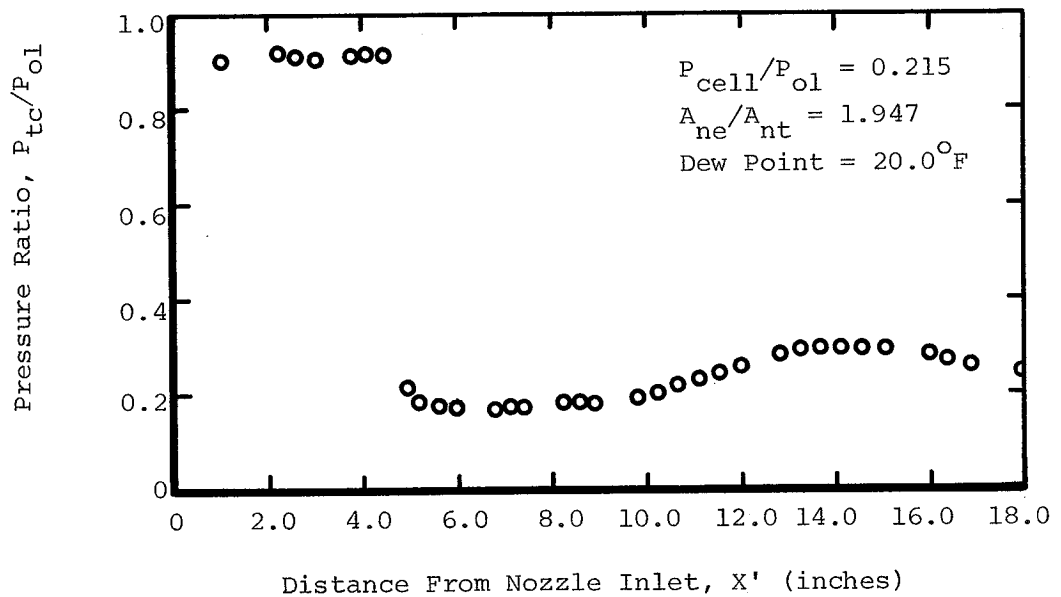
a.) Top Contour Static Pressure Variation.
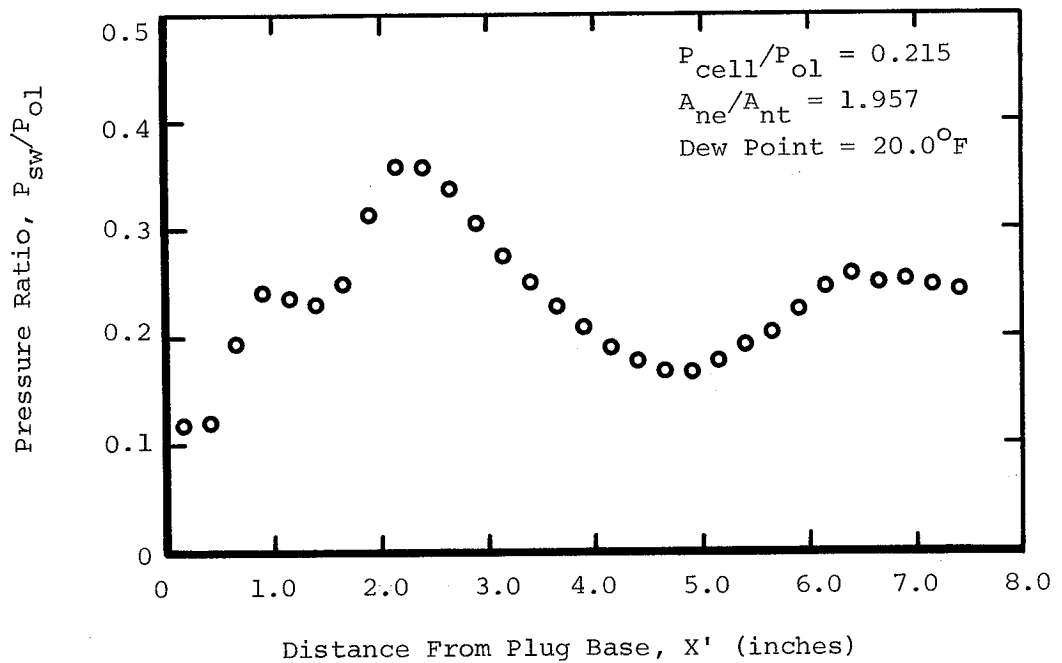
b.) Sidewall Centerline Static Pressure Variation.

Fig. 24. Planar Truncated Plug Nozzle Static Pressure Distributions
Corresponding to Fig. 19e and Point e in Fig. 12.
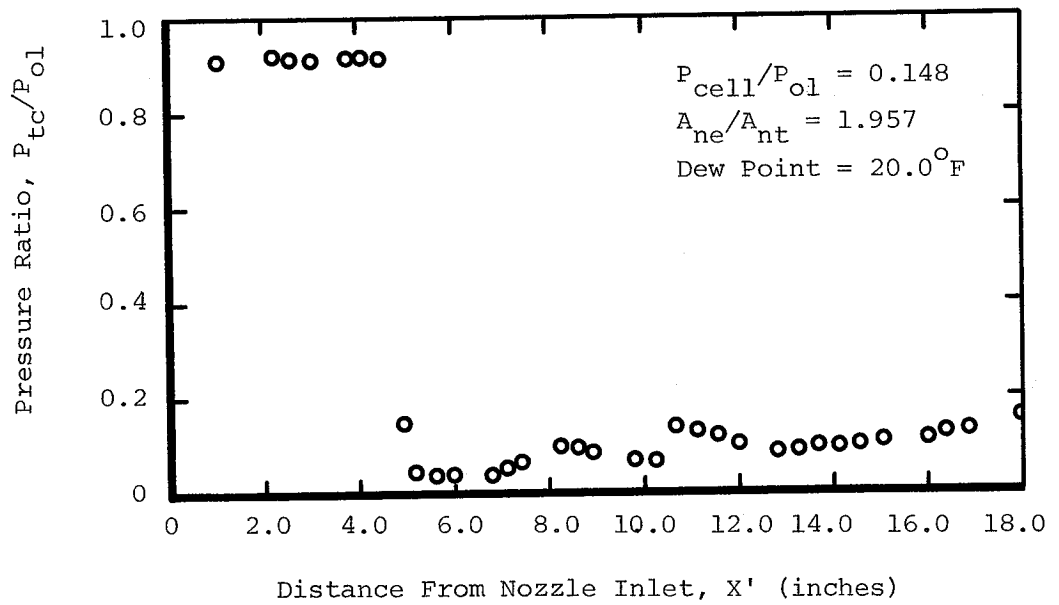
a.) Top Contour Static Pressure Variation.
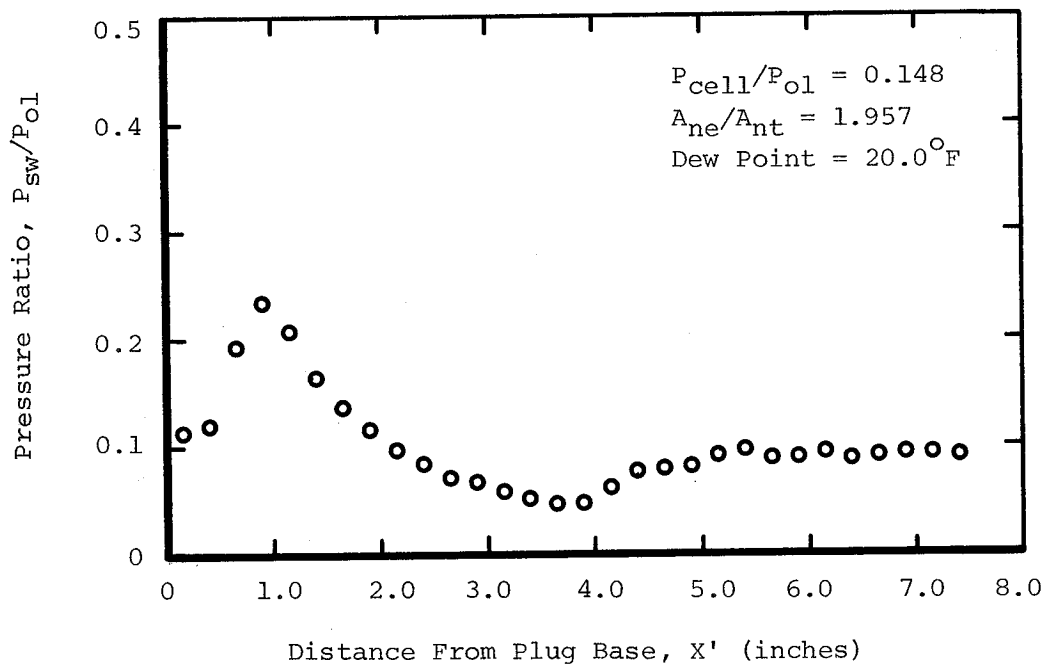
b.) Sidewall Centerline Static Pressure Variation.

Fig. 25. Planar Truncated Plug Nozzle Static Pressure Distributions
Corresponding to Fig. 19f and Point f in Fig. 12.

Fig. 26.   Simultaneous Smokeline-Opaque-Stop Schlieren Photograph
of Planar Truncated Plug Nozzle Flow Field.
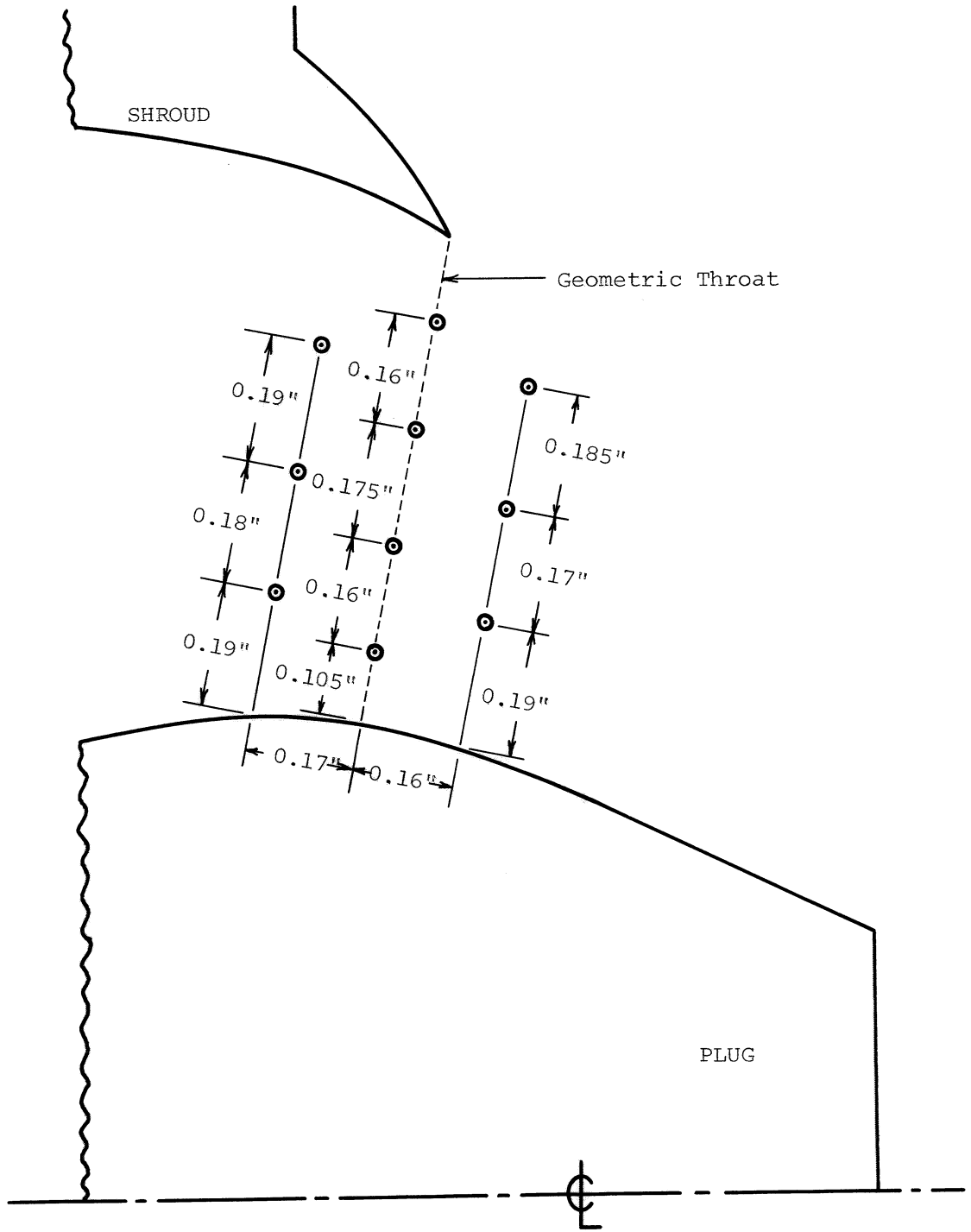
Fig. 27. Location of Sidewall Static Pressure Taps in Throat Region.

SHROUD			
	Interpolated Sonic Line		
4		1	
	8		
5		2	
	9		
6		3	
	10		
7			
Geometric Throat			
PLUG			
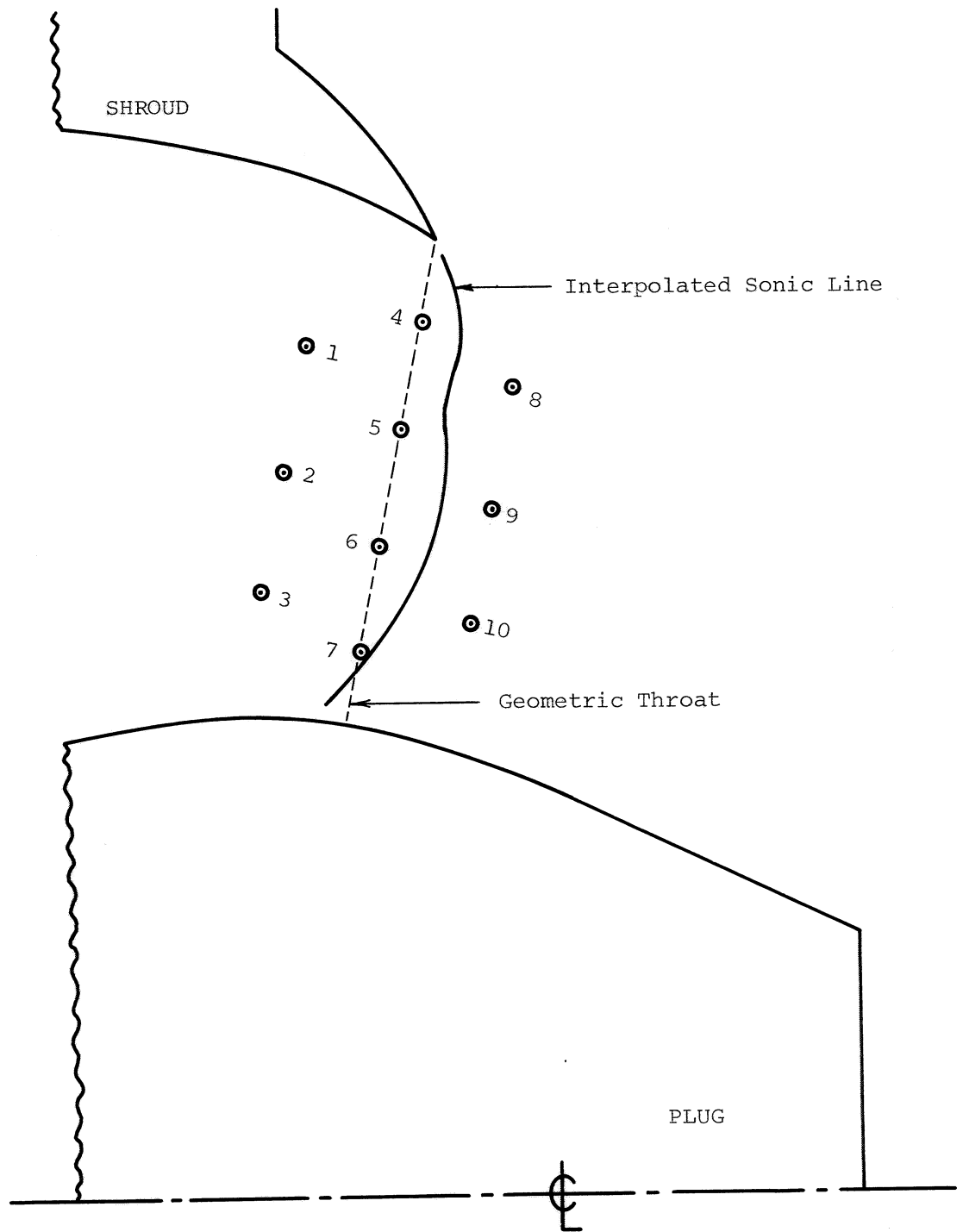
Pressure Tap	Mach No.	Pressure Tap	Mach No.
1	0.66	6	0.91
2	0.72	7	0.99
3	0.81	8	1.18
4	0.88	9	1.10
5	0.90	10	1.12

Fig. 28. Location of Interpolated Sonic Line with Respect to Geometric Throat

Pressure Ratio, P_{sw}/P_{ol}

Undisturbed Flow

1/4" Wire Mesh

Boundary Layer Trip

No Diffuser

$P_{ex}/P_{ol} \simeq 0.266$

$P_{cell}/P_{ol} = 0.148$

$A_{ne}/A_{nt} = 1.957$

Dew Point $< 30^{\circ}F$

0.5

0.4

0.3

0.2

0.1

0

0   1.0   2.0   3.0   4.0   5.0   6.0   7.0   8.0

D

Distance From Plug Base, X' (inches)
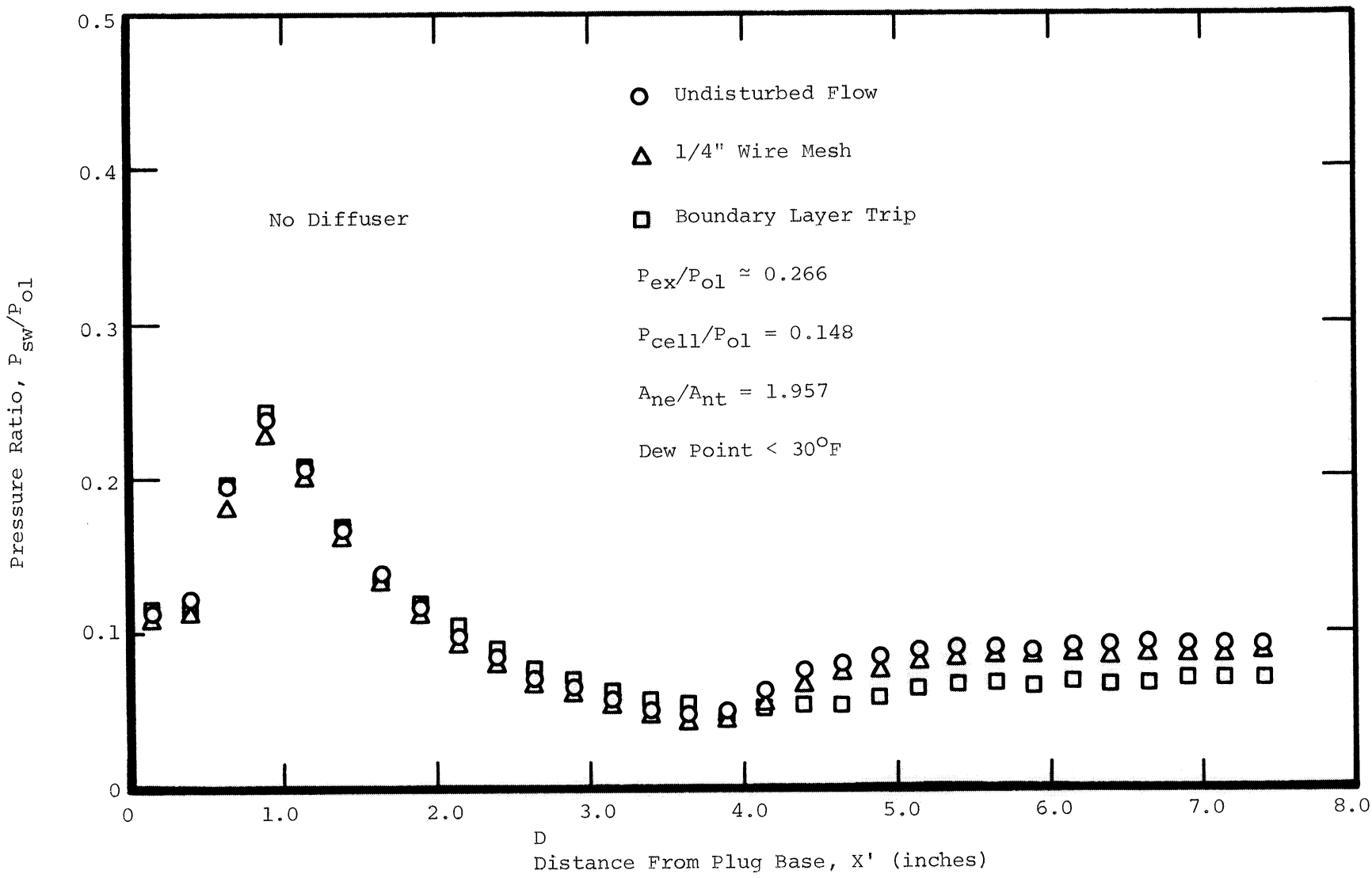
Fig. 29. Induced Turbulence Effects on Sidewall Centerline Static Pressure Variation of Planar Truncated Plug Nozzle.
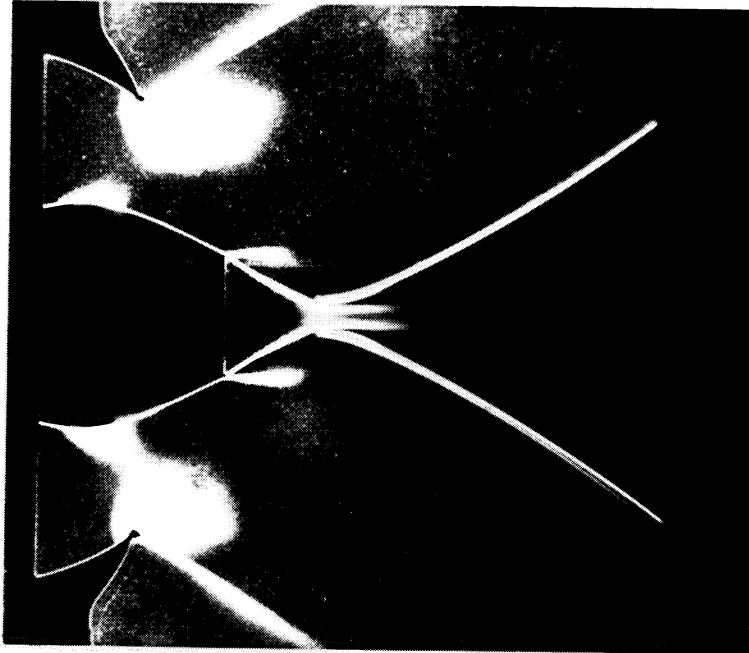
a.)   No Base Bleed.
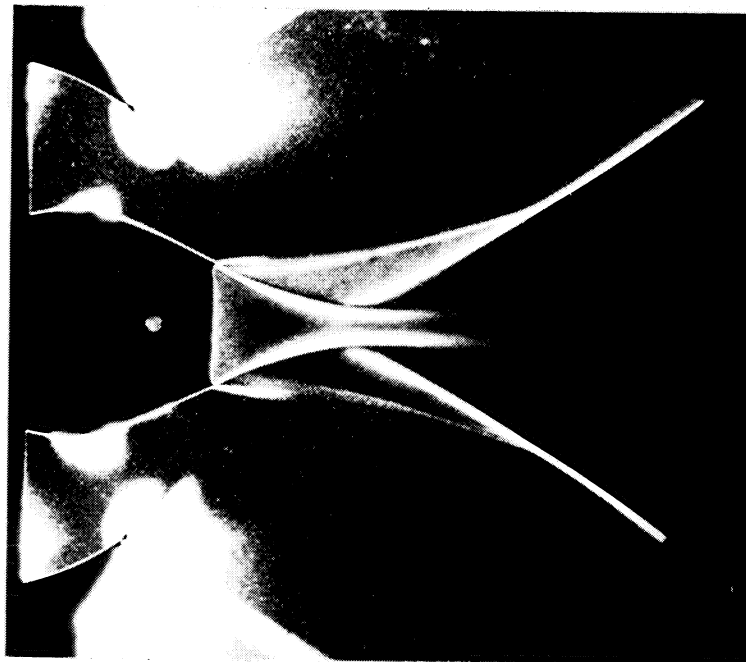
b.)   Base Bleed 1.0% of Nozzle Flow

Fig. 30.   Schlieren Photographs of Planar Truncated Plug Nozzle
With and Without Base Bleed.
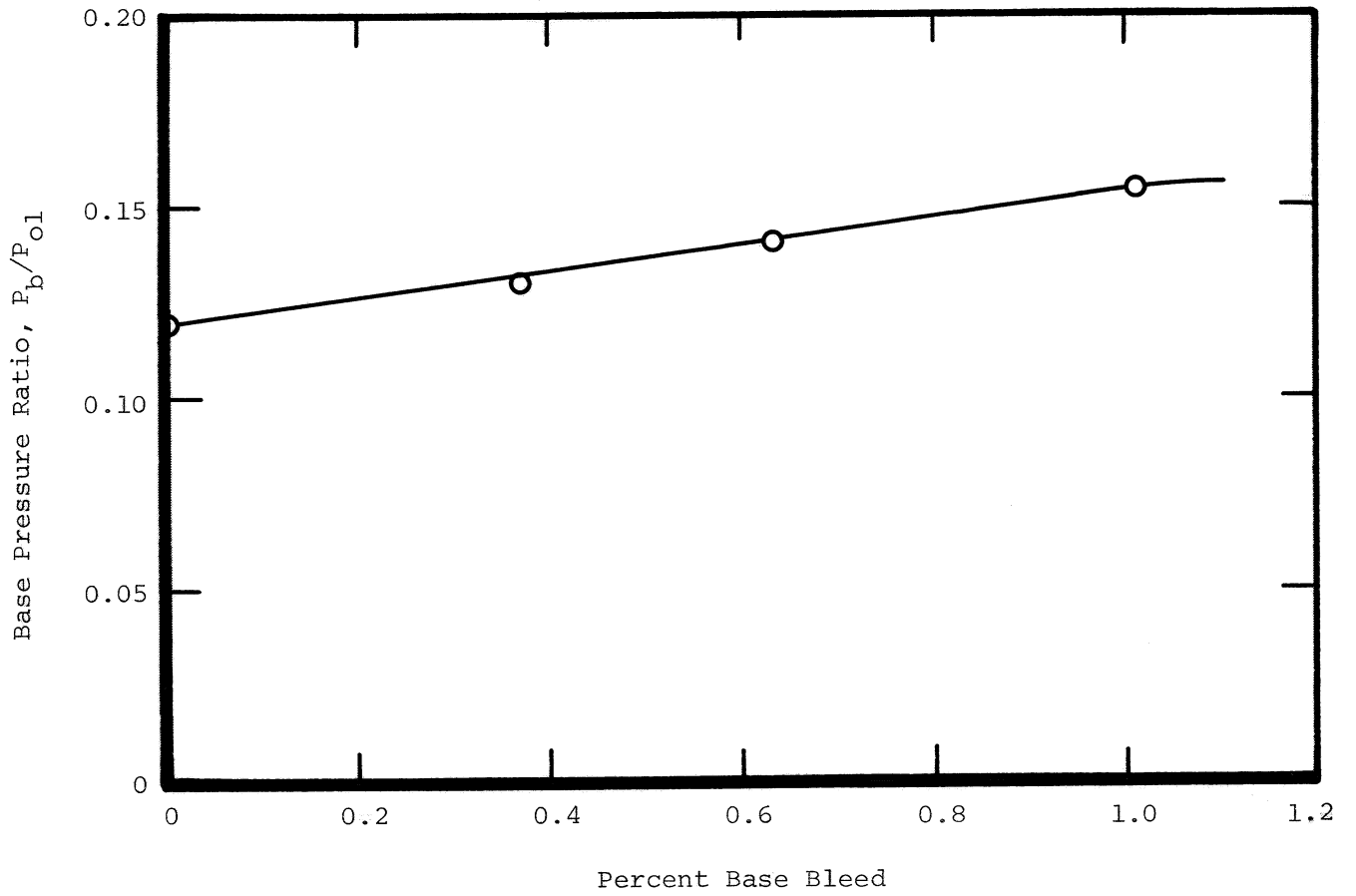
Fig. 31. Effect of Base Bleed on Base Pressure of Truncated Plug Nozzle.
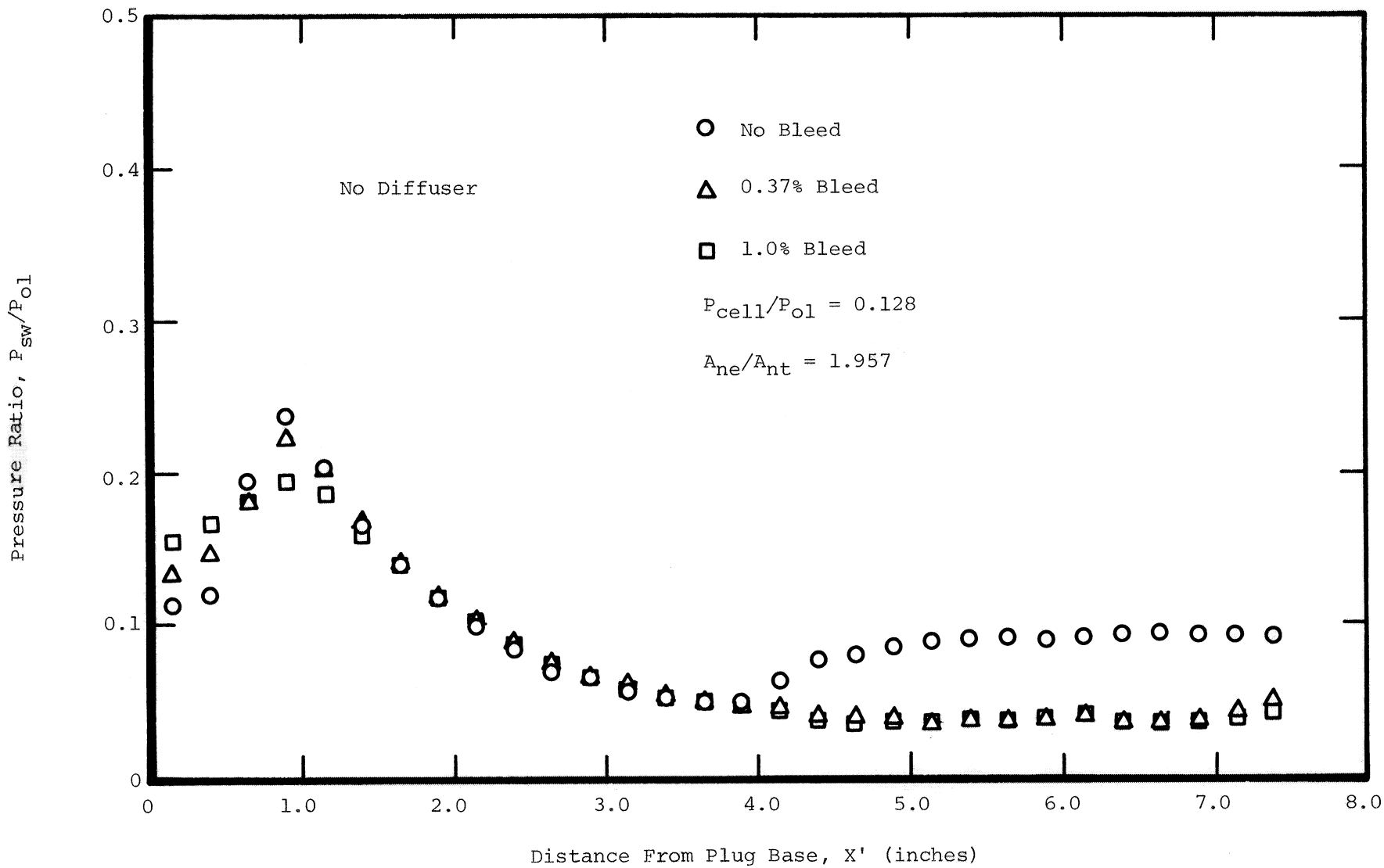
Fig. 32. Effect of Base Bleed on Sidewall Centerline Static Pressure of Planar Truncated Plug Nozzle.

Top View of Thrust Stand
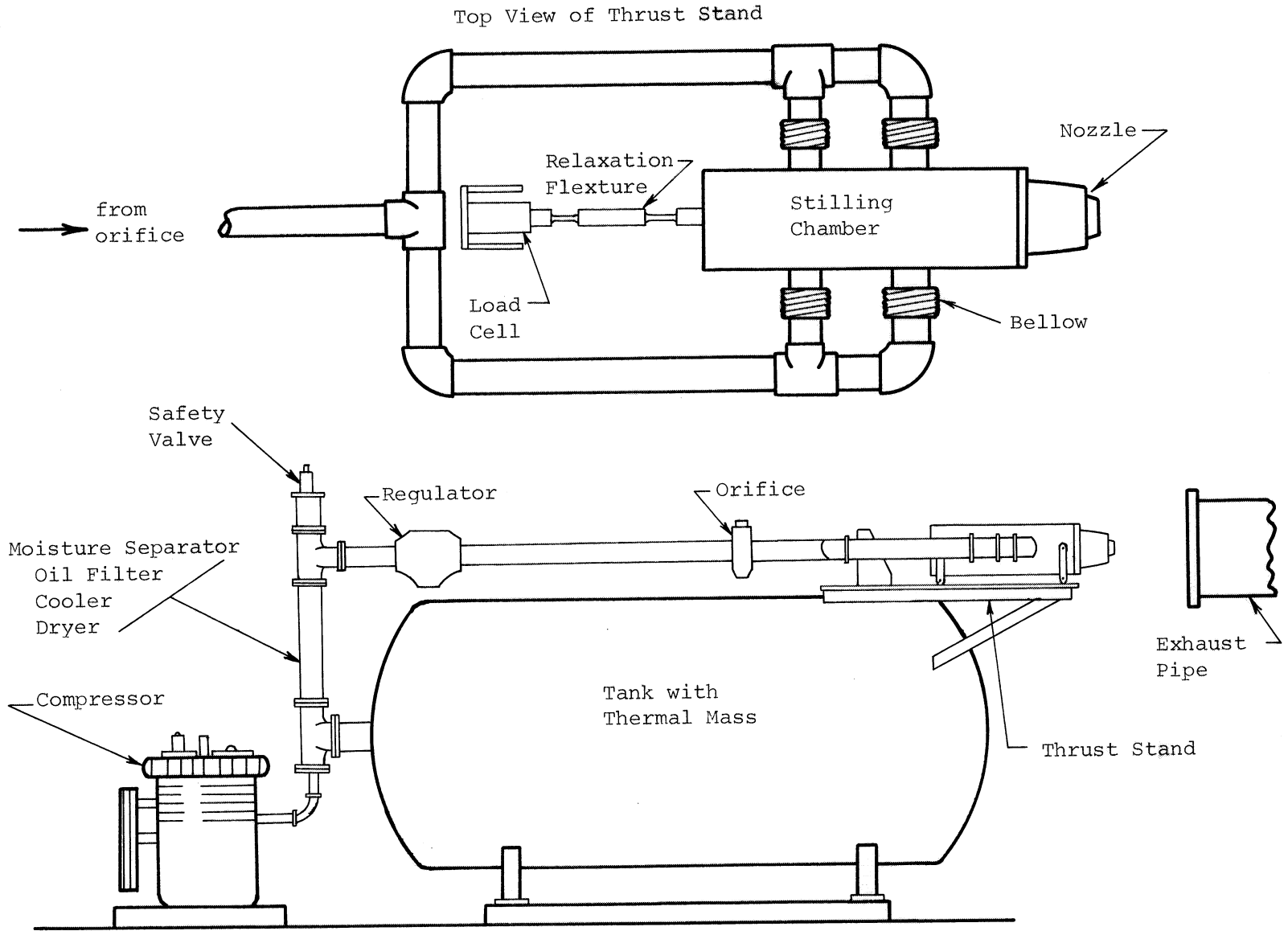
Fig. 33. Sketch of Nozzle Thrust Facility.
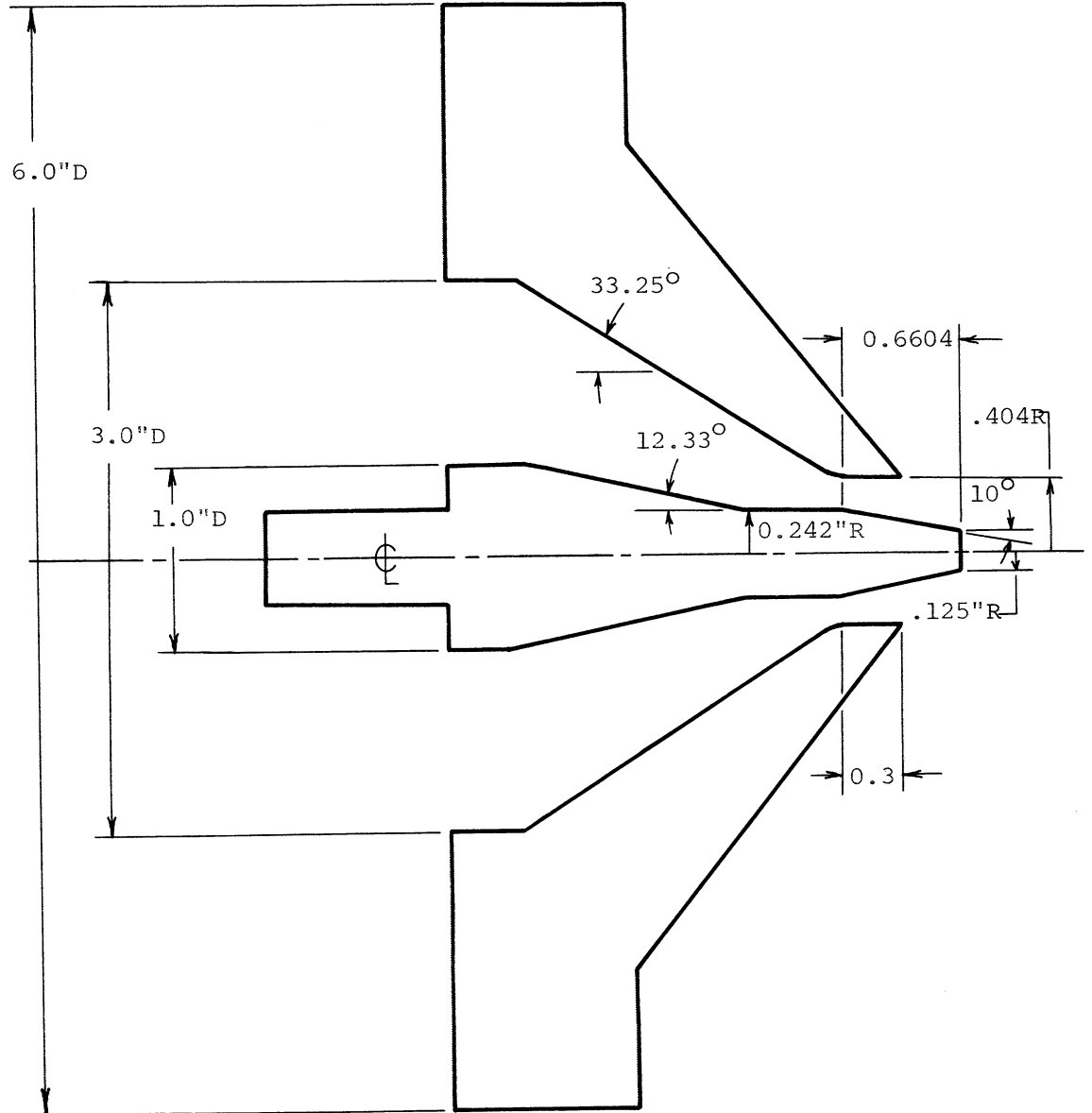
Fig. 34. Schematic of the Internal-External-Expansion Nozzle Designed
for the Nozzle Thrust Facility.
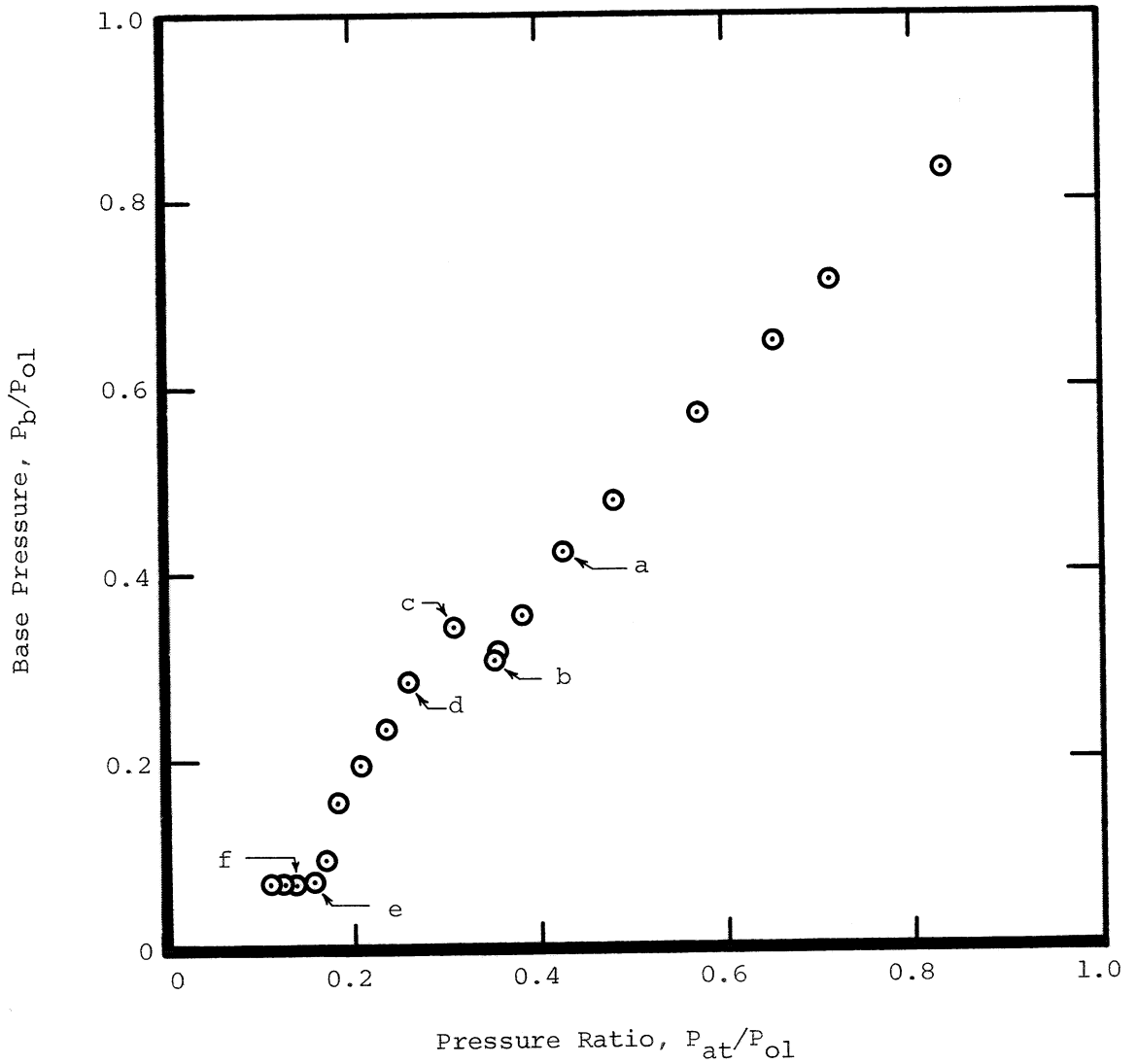
Fig. 35. Axisymmetric Truncated Plug Nozzle Operating Characteristics.
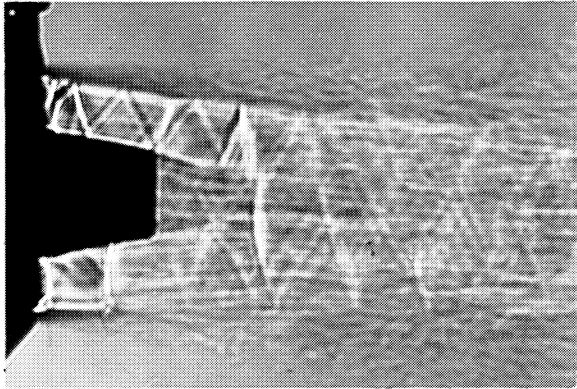
a.) $P_{at}/P_{ol} = 0.425$

d.) $P_{at}/P_{ol} = 0.260$

b.) $P_{at}/P_{ol} = 0.354$

e.) $P_{at}/P_{ol} = 0.157$

c.) $P_{at}/P_{ol} = 0.310$
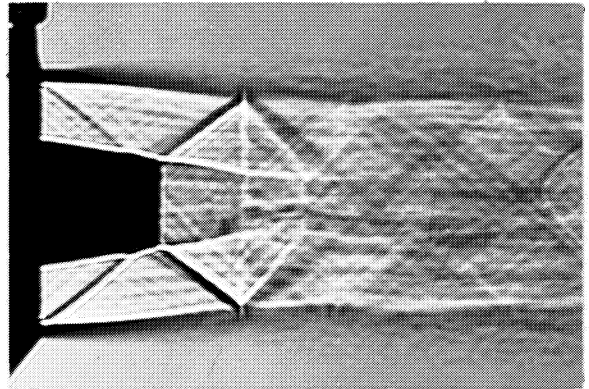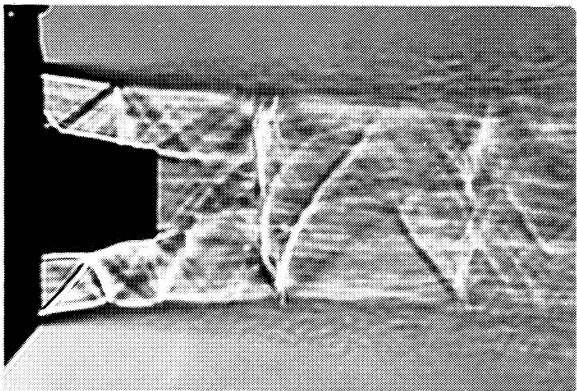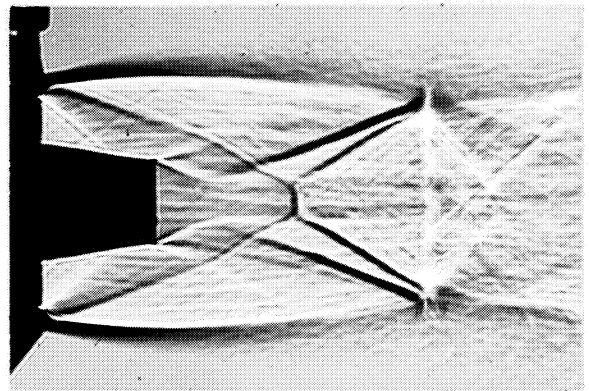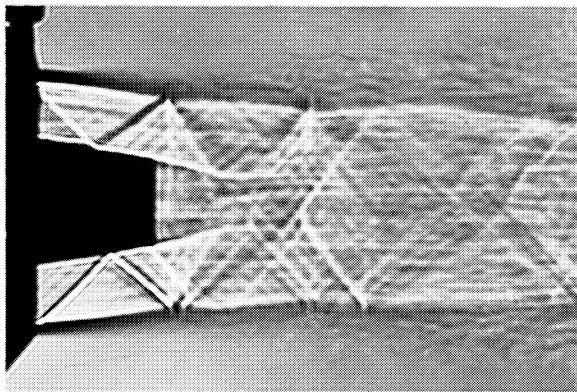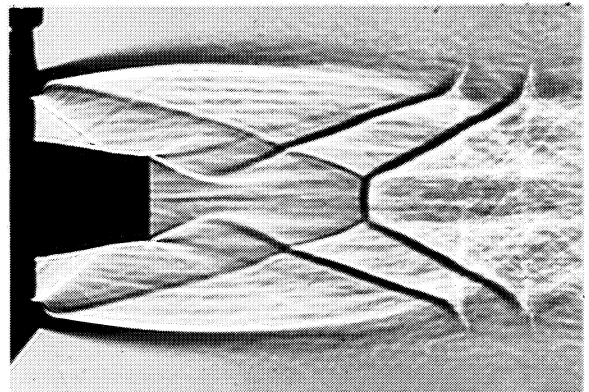
f.) $P_{at}/P_{ol} = 0.135$

Fig. 36.   Shadowgraph Sequence for Axisymmetric Truncated Plug
Nozzle Flow Development.

- 103 -
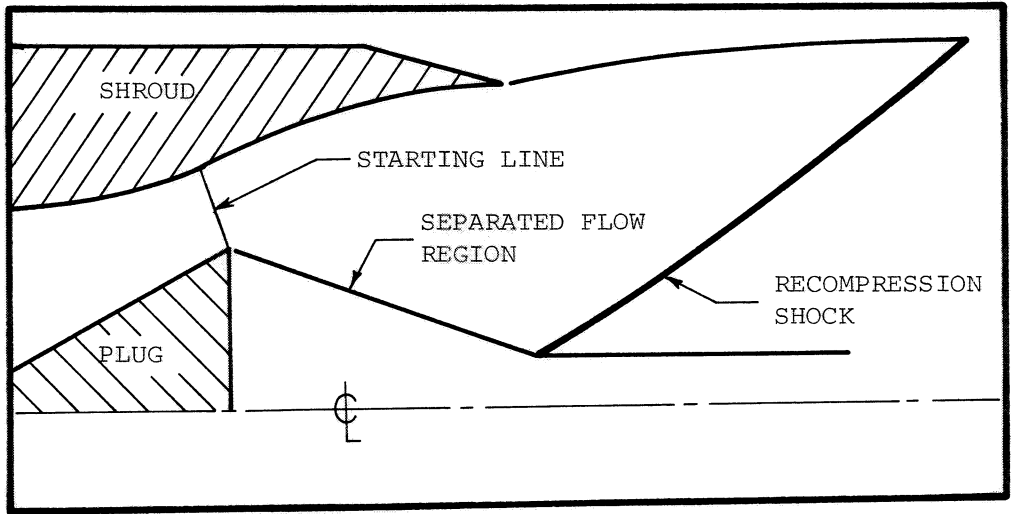
a.) Expansion-Deflection Nozzle Flow Field Model.
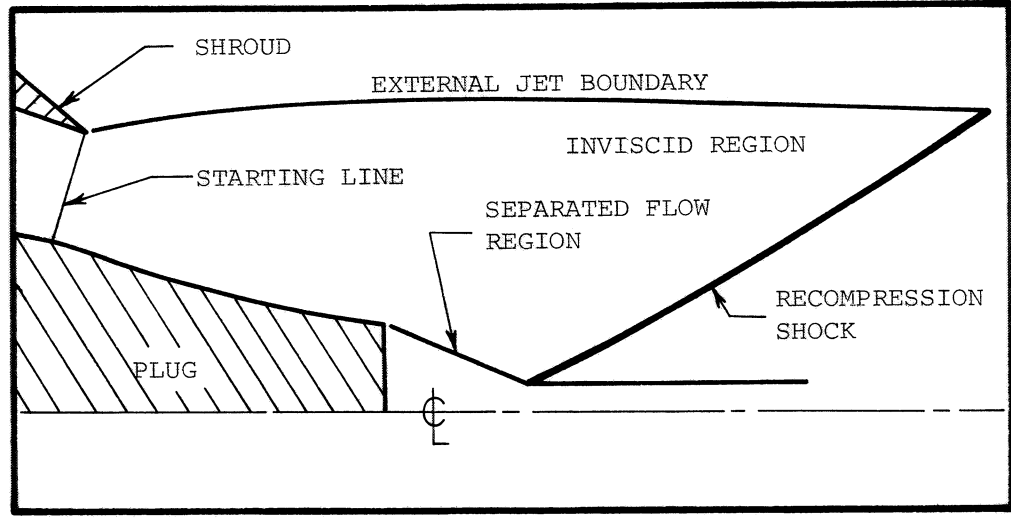
b.) Truncated-Plug Nozzle Flow Field Model.

Fig. 37. Flow Field Models for Plug Nozzle Configurations.
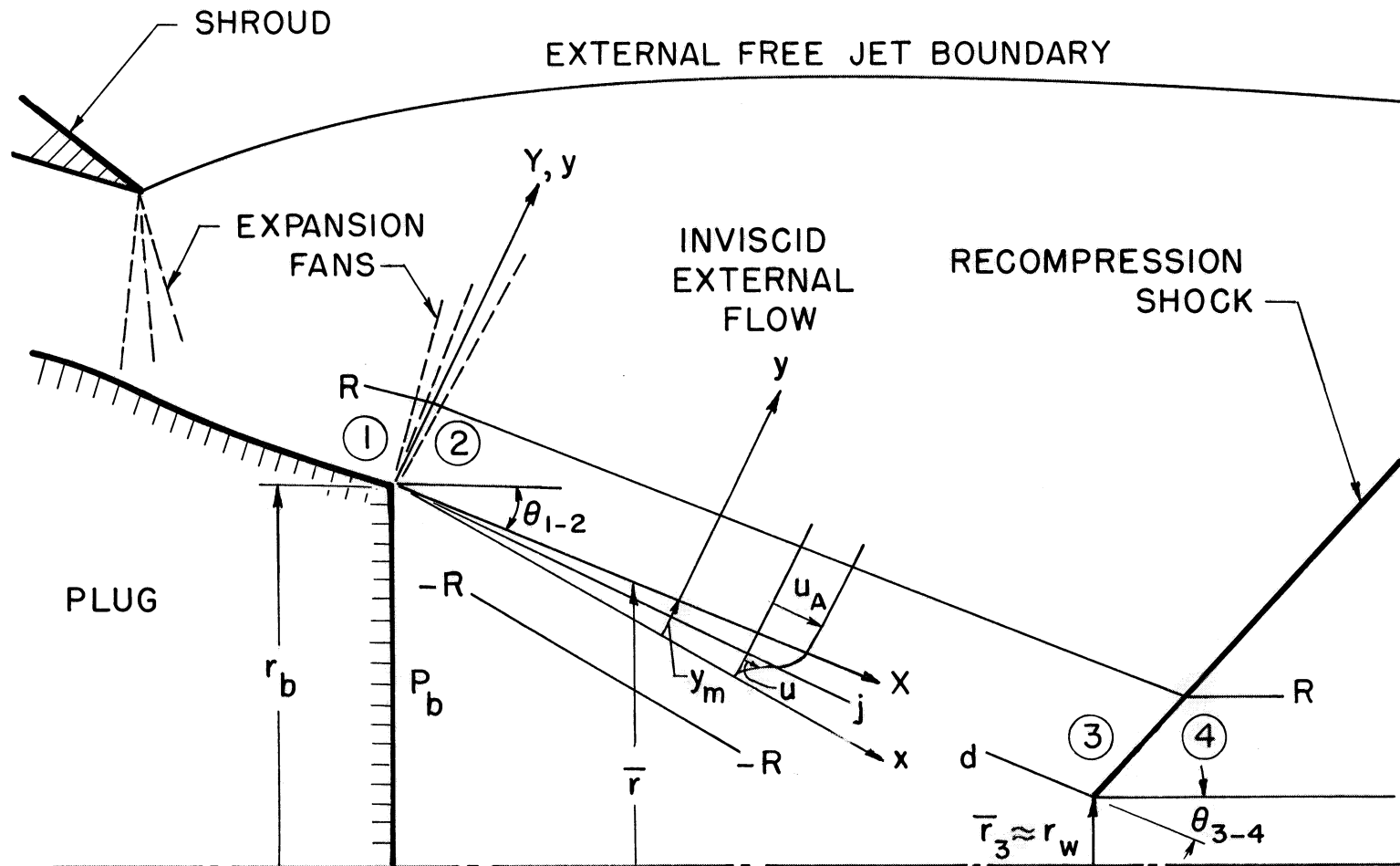
Fig. 38. Flow Model for the Determination of the Turbulent Base Pressure and the External Flow Field for an Axisymmetric Plug Nozzle.
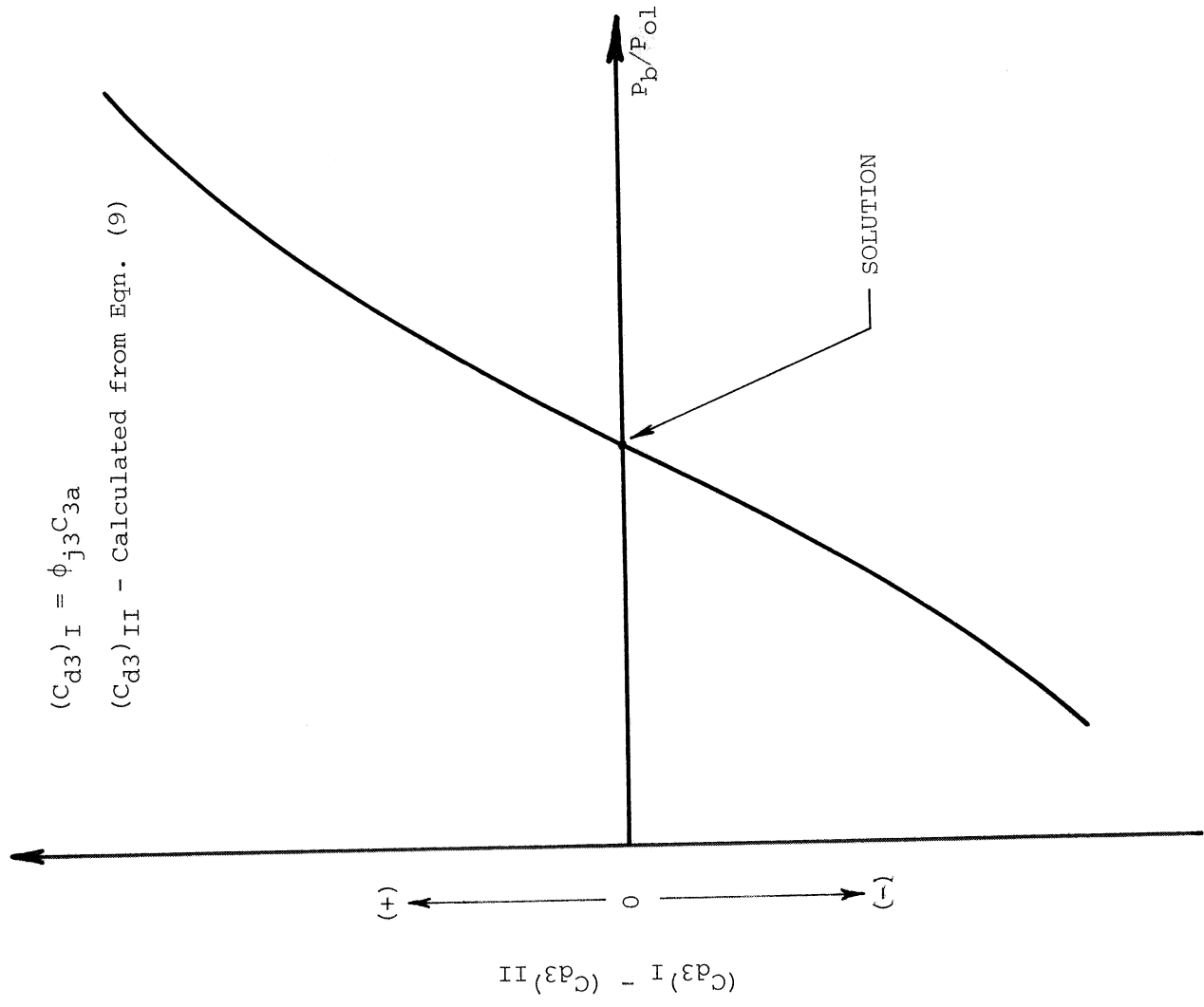
Fig. 39. Base Pressure Solution Curve (No Base Bleed).
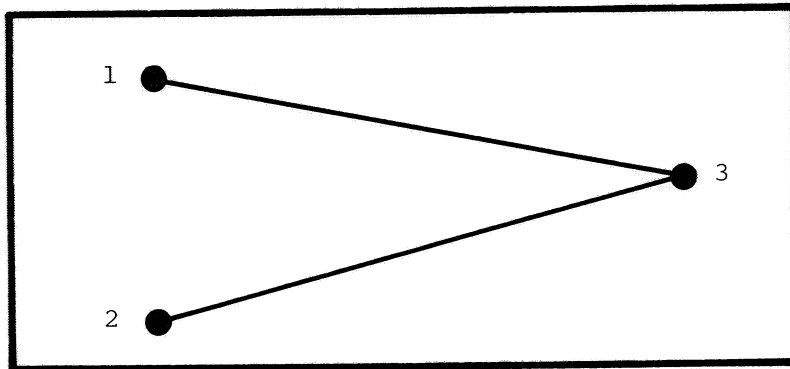
a.) Interior Point
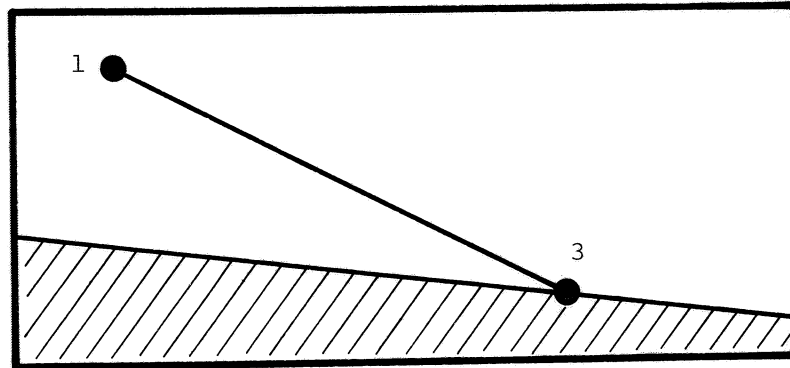
b.) Solid Lower Boundary
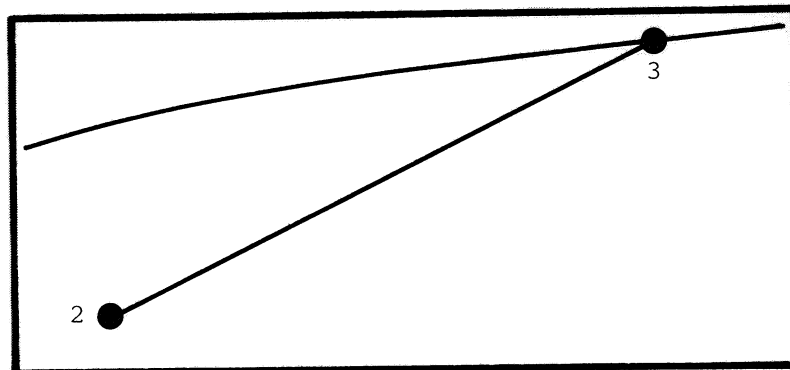
c.) Constant Pressure Upper Boundary

Fig. 40. Method of Characteristics Computation Scheme.
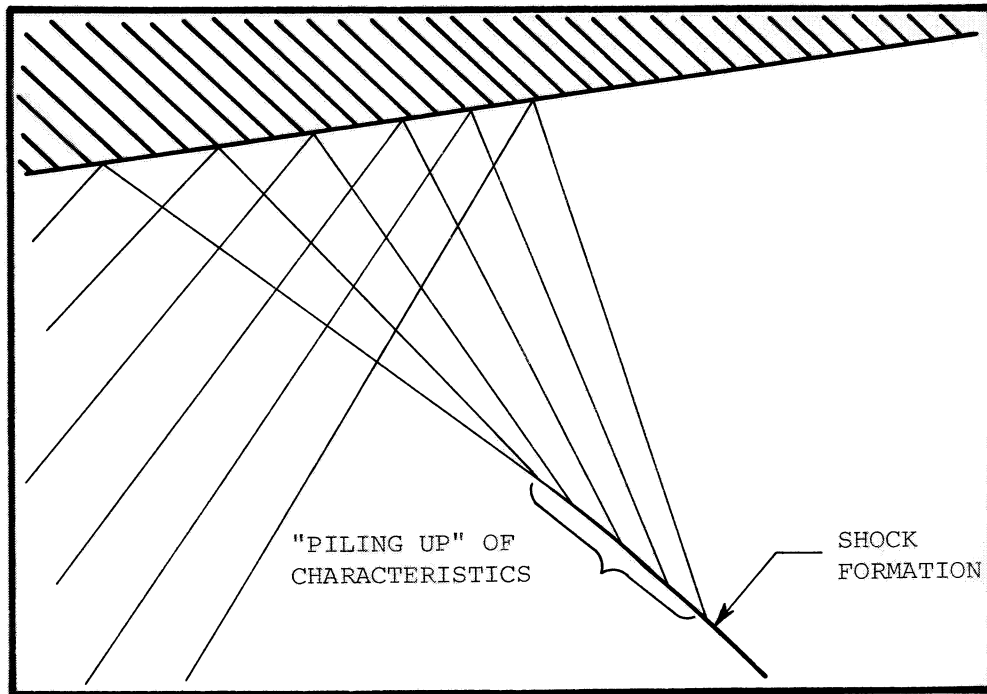
a.)   "Piling Up" of Characteristic Waves
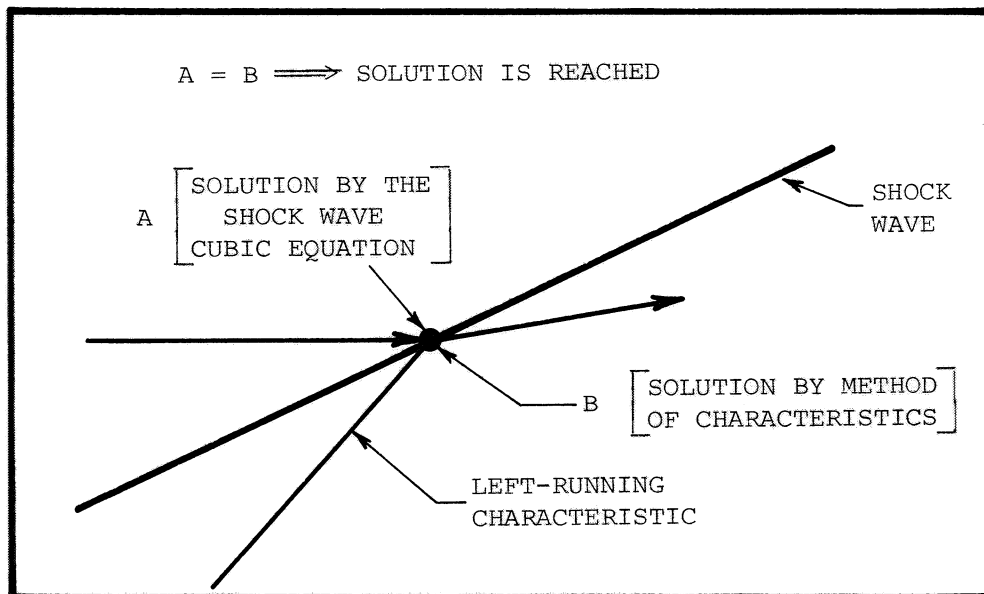
b.)   Shock Wave Solution

Fig. 41.   Method of Characteristics Solution with an Imbedded
           Shock Wave.
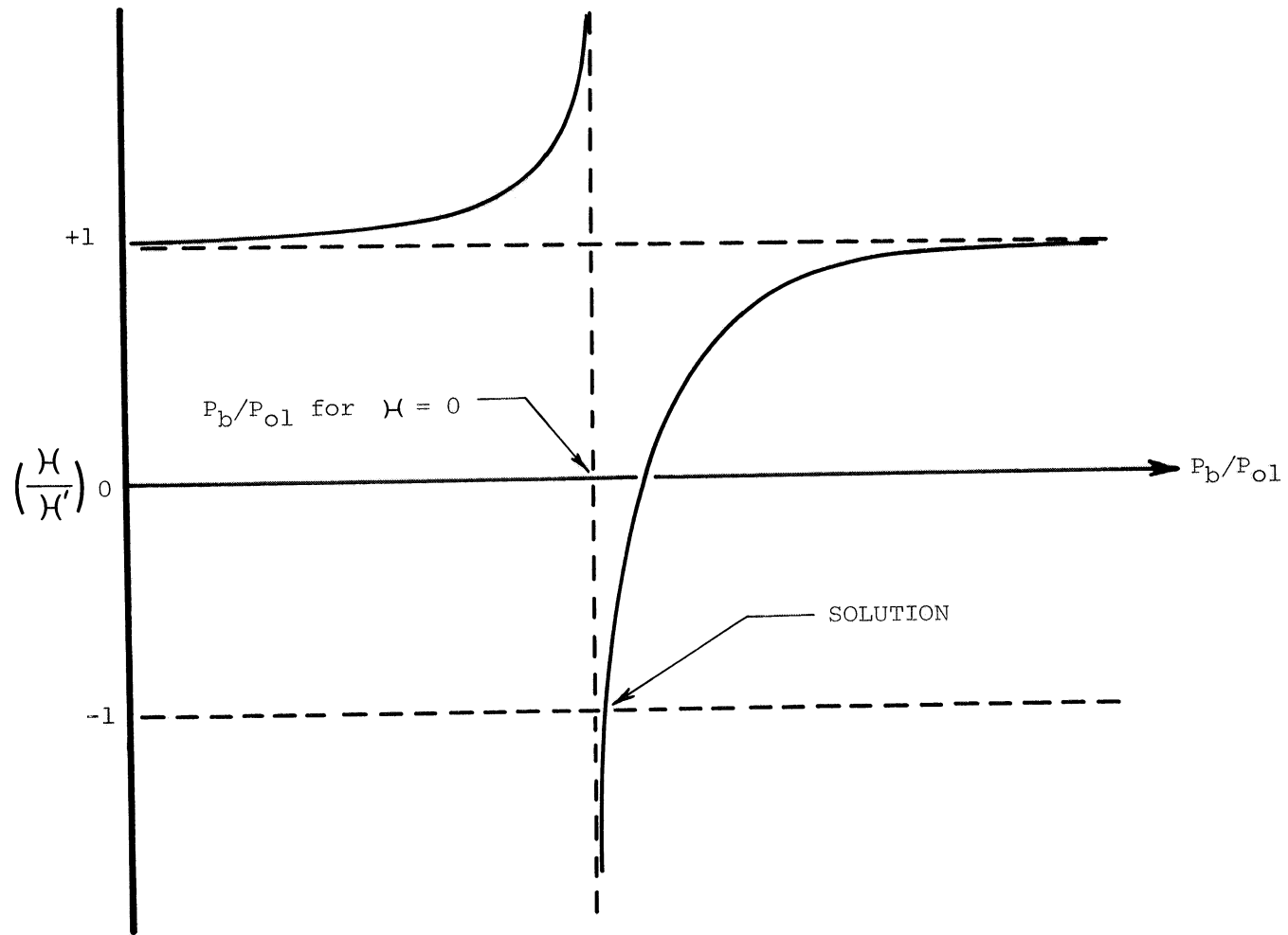
Fig. 42. Base Pressure Solution Curve When Base Bleed is Present.
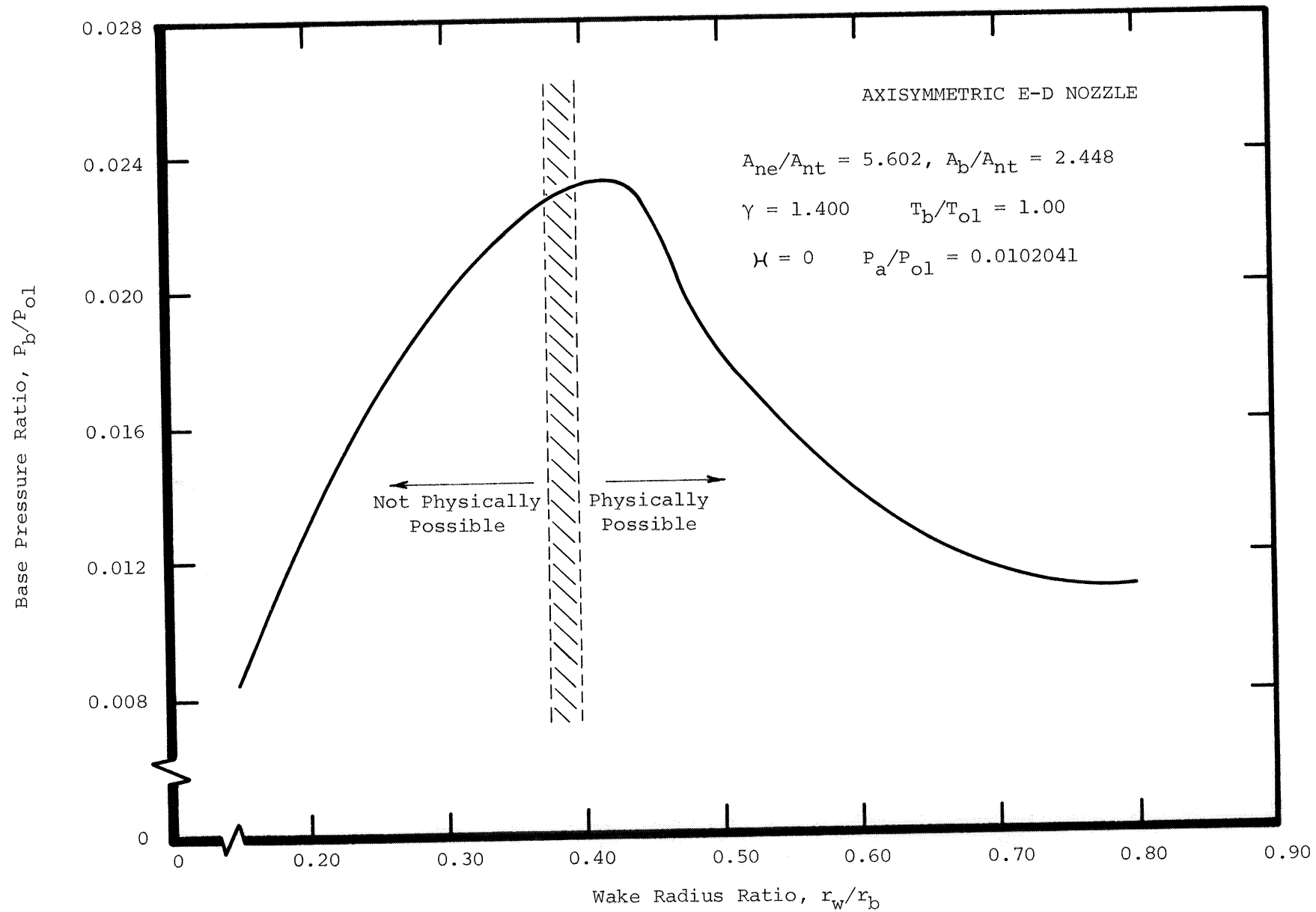
Fig. 43. Variation of Plug Base Pressure with Wake Radius Ratio for an Axisymmetric Expansion-Deflection Nozzle.
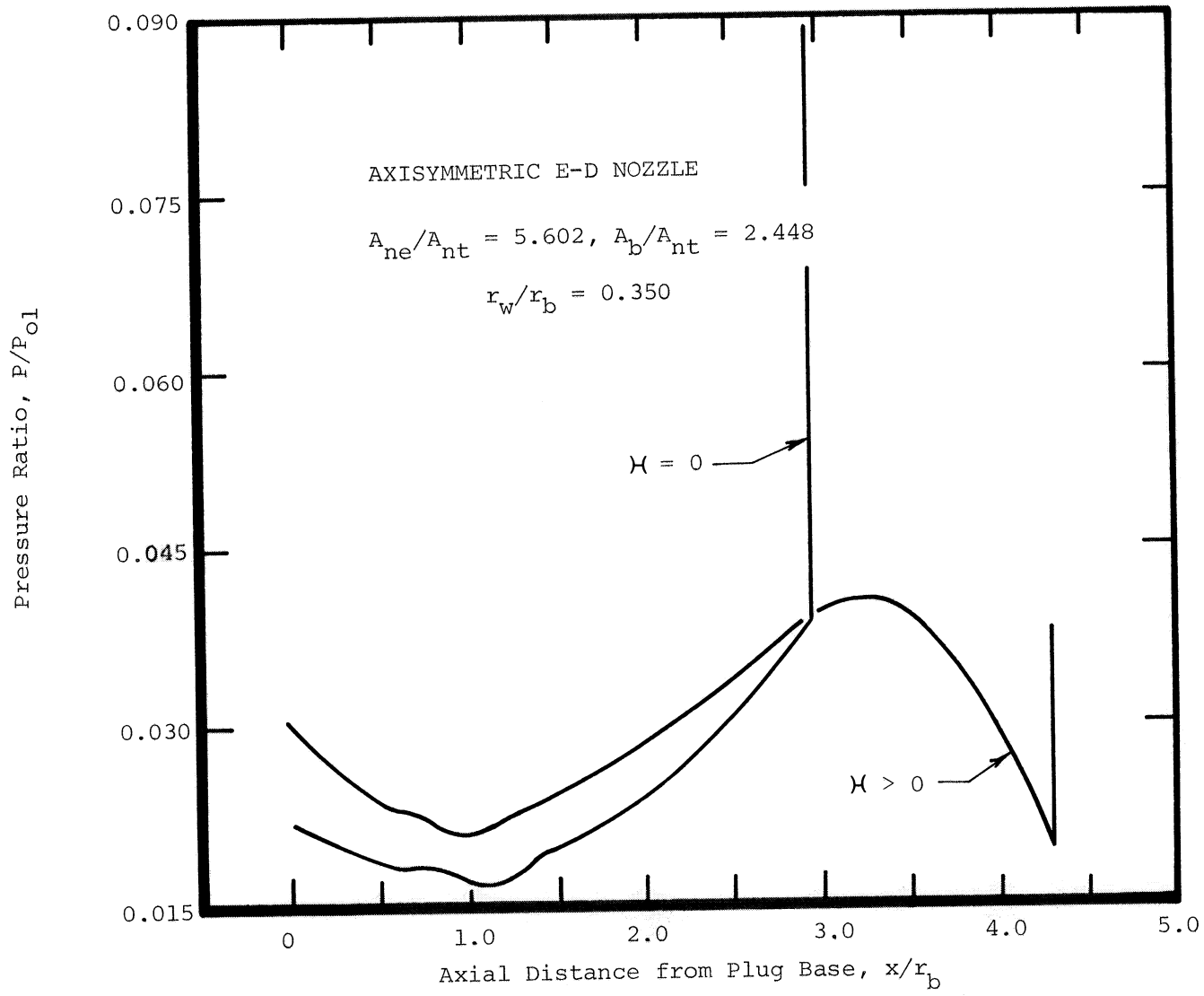
Fig. 44. Pressure Ratio Along the Near Wake from Computer Solution at Constant Wake Radius Ratio.
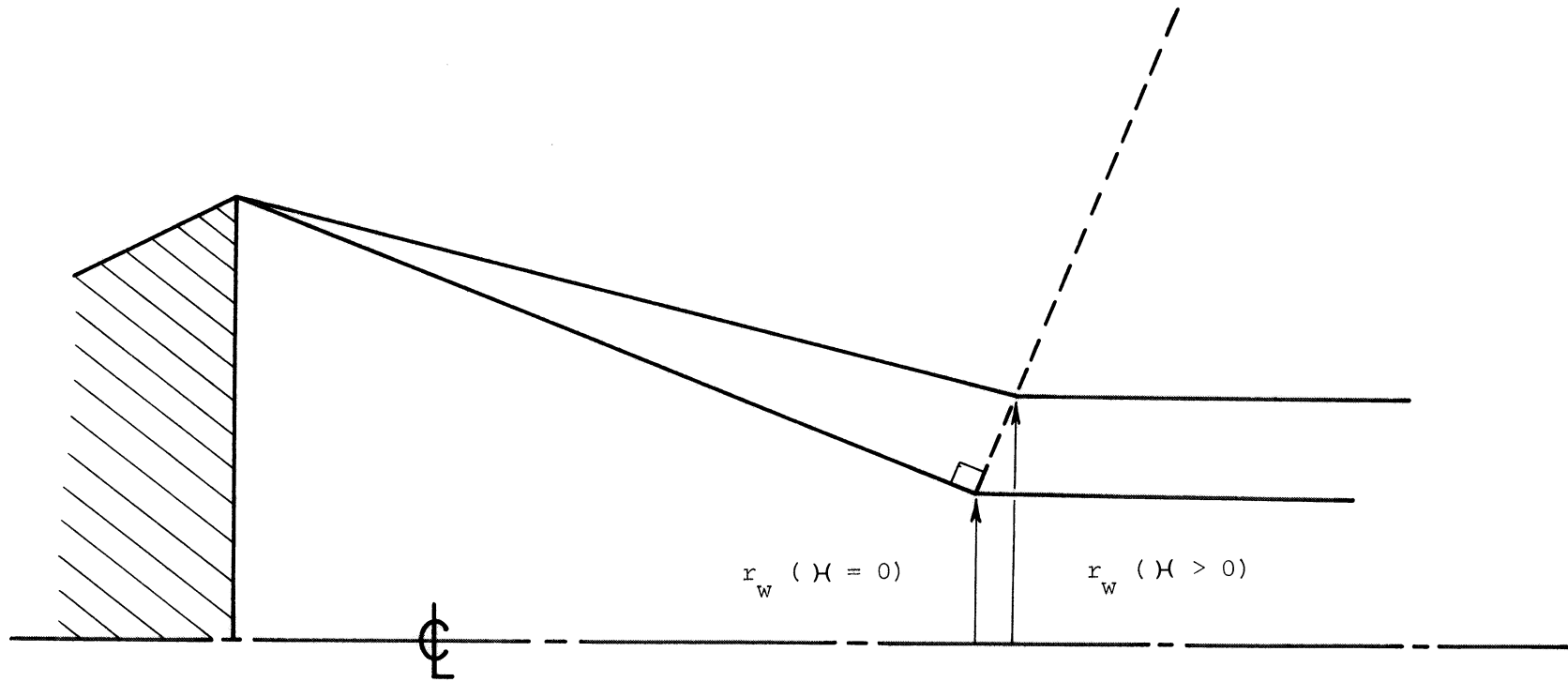
Fig. 45.   Solution of the Wake Radius Ratio Problem for Base Bleed.
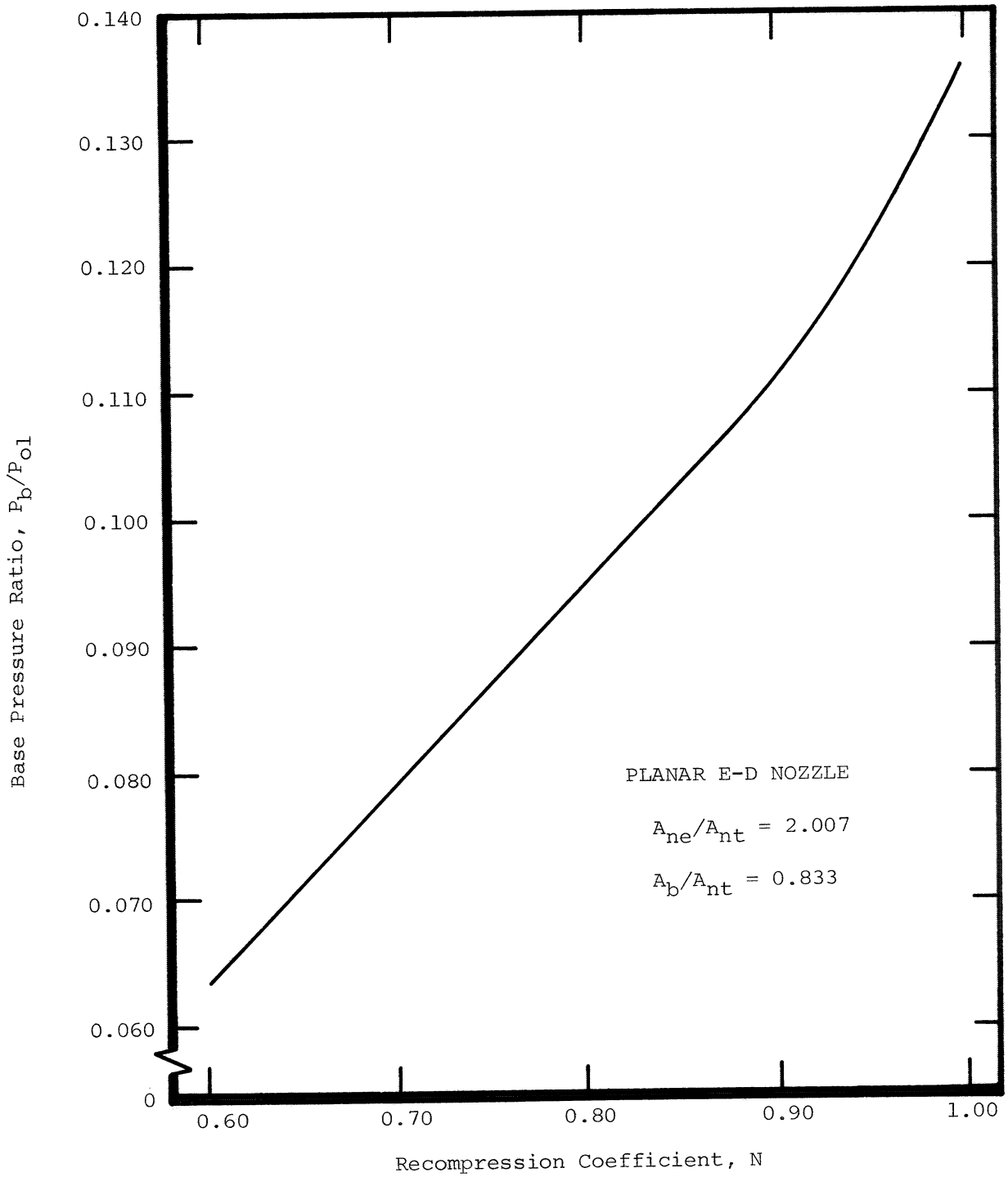
Fig. 46. Variation of the Base Pressure Ratio with Recompression
Coefficient for a Planar Expansion-Deflection Nozzle.
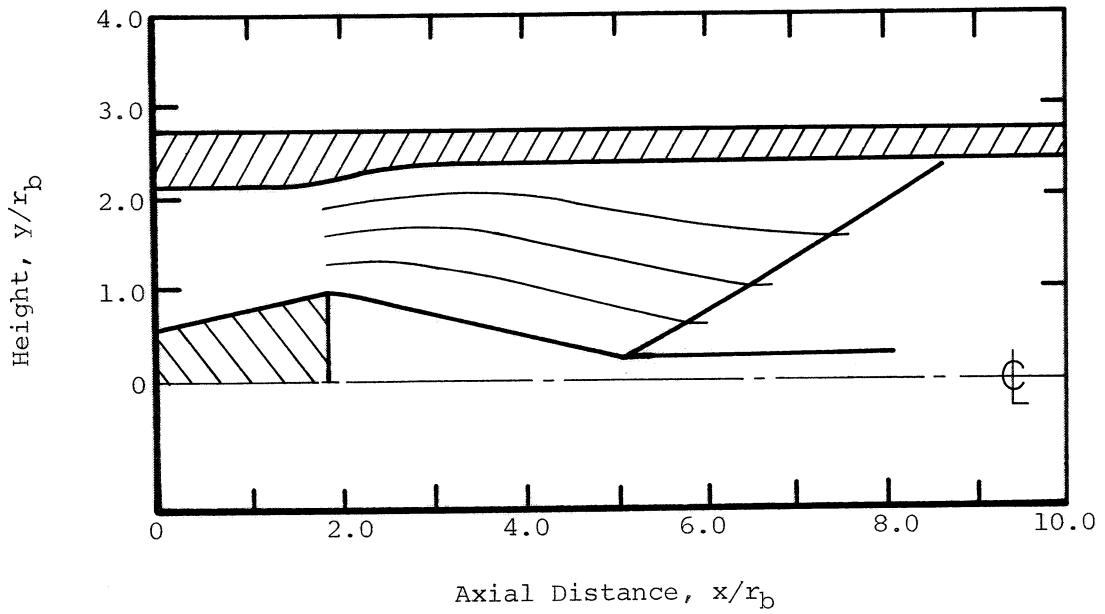
a.) 20 Characteristics in the Vertical Direction
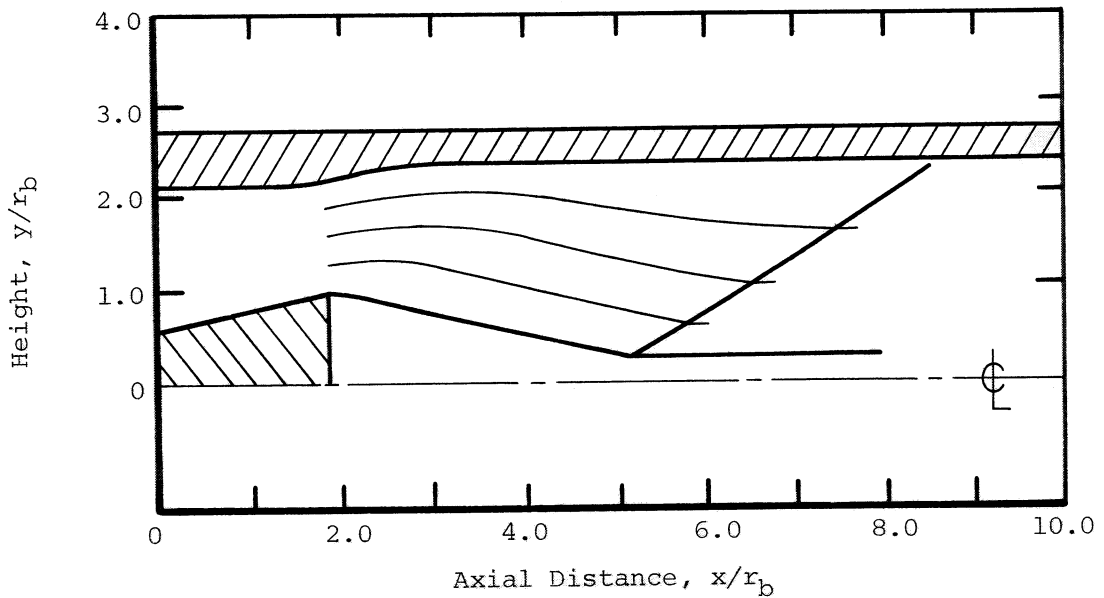
b.) 40 Characteristics in the Vertical Direction

Fig. 47. Flow Field Comparison for Differing Characteristic Mesh
Sizes of a Planar Expansion-Deflection Nozzle
$(A_{ne}/A_{nt} = 2.007$ and $A_b/A_{nt} = 0.833)$.
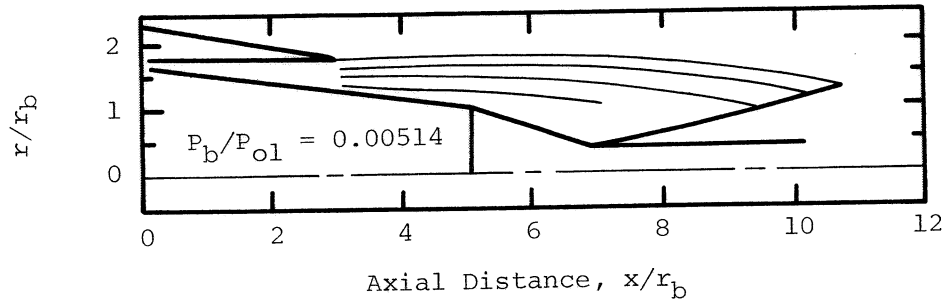
a.) Vertical Sonic Line ("Uniform")
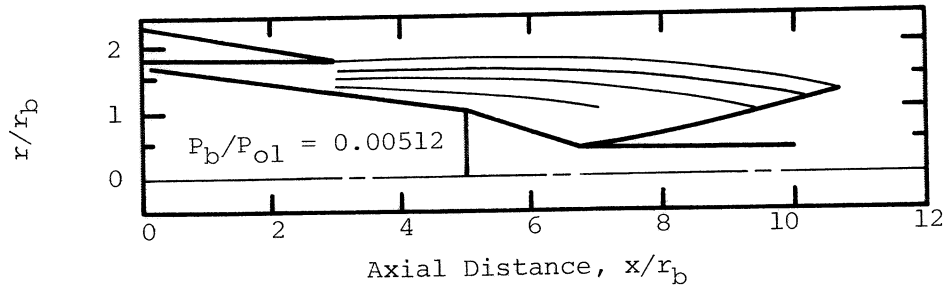
b) Parabolic Sonic Line
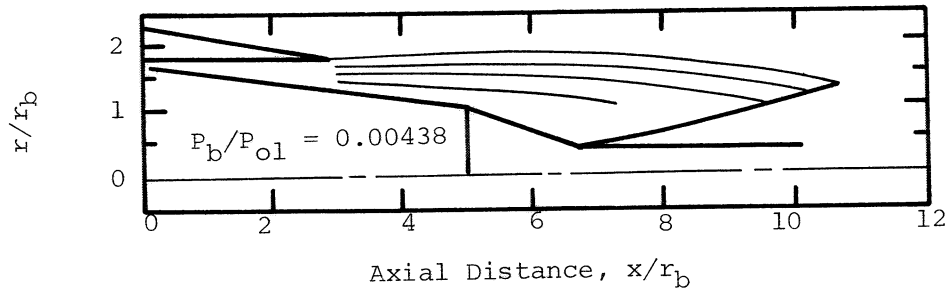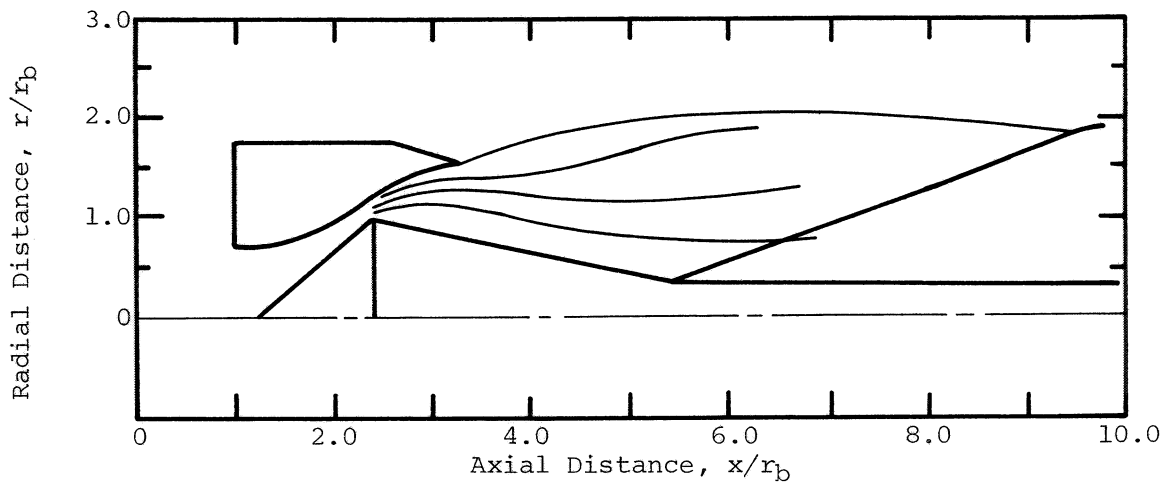

c.) Linear Sonic Line
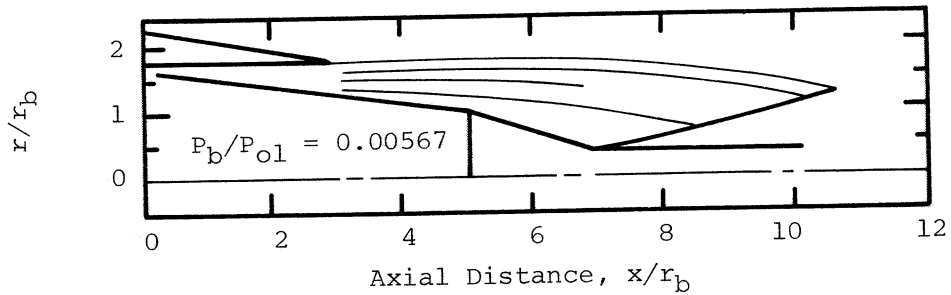
d.) Circular Arc Sonic Line

Fig. 48. The Influence of Sonic Line Shapes for an Axisymmetric Internal-External-Expansion Truncated Plug Nozzle.
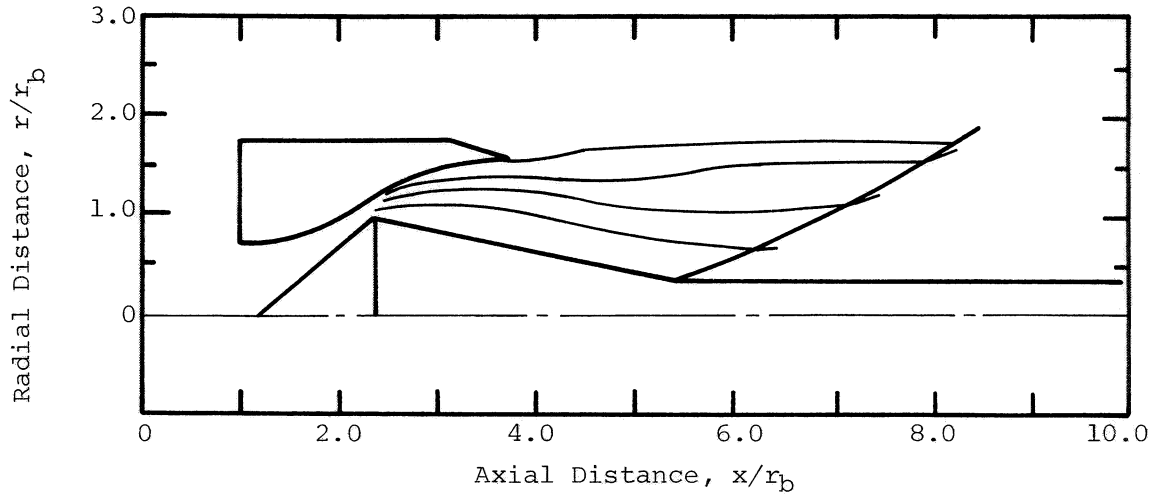
a.) $A_{ne}/A_{nt} = 5.602$
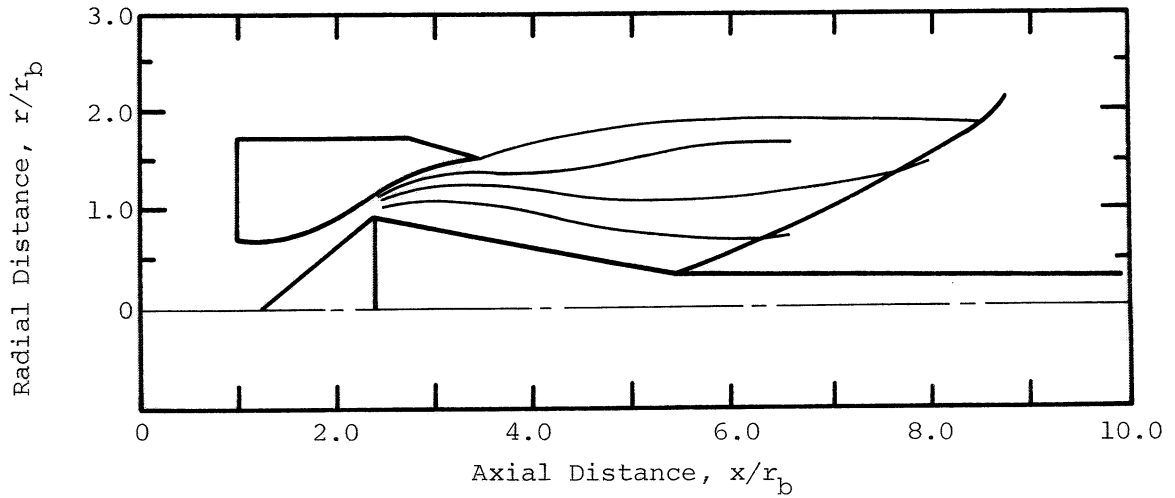
b.) $A_{ne}/A_{nt} = 5.580$

c.) $A_{ne}/A_{nt} = 5.513$

Fig. 49. Shroud Contour Truncation of an Axisymmetric Expansion-
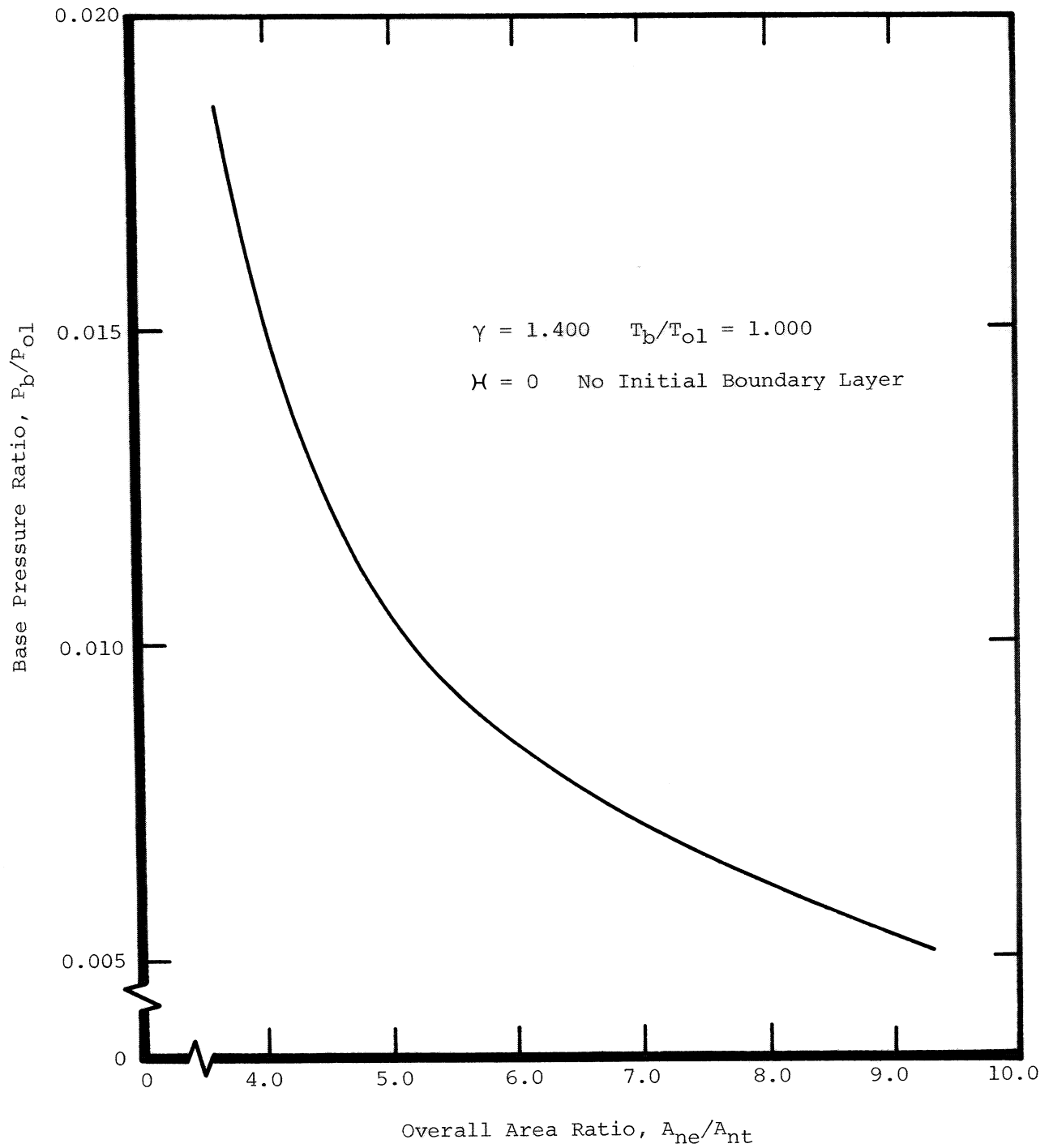Deflection Nozzle ($A_b/A_{nt} = 2.448$).

Fig. 50. Influence of Area Ratio on the Base Pressure Ratio of an Axisymmetric Internal-External-Expansion Truncated Plug Nozzle.
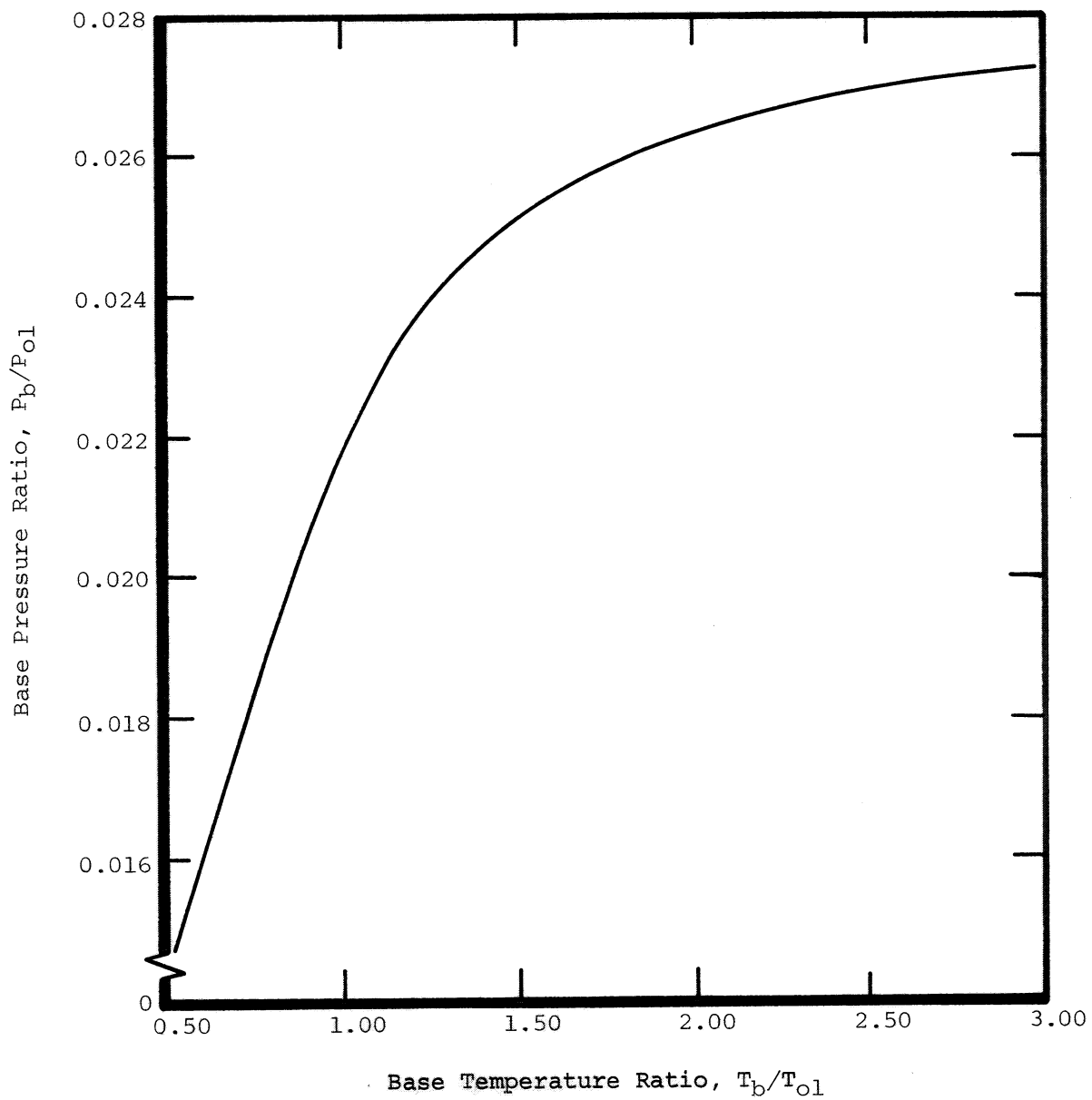
Fig. 51. Effect of Non-Isoenergetic Mixing on the Base Pressure of an Axisymmetric Expansion-Deflection Nozzle.
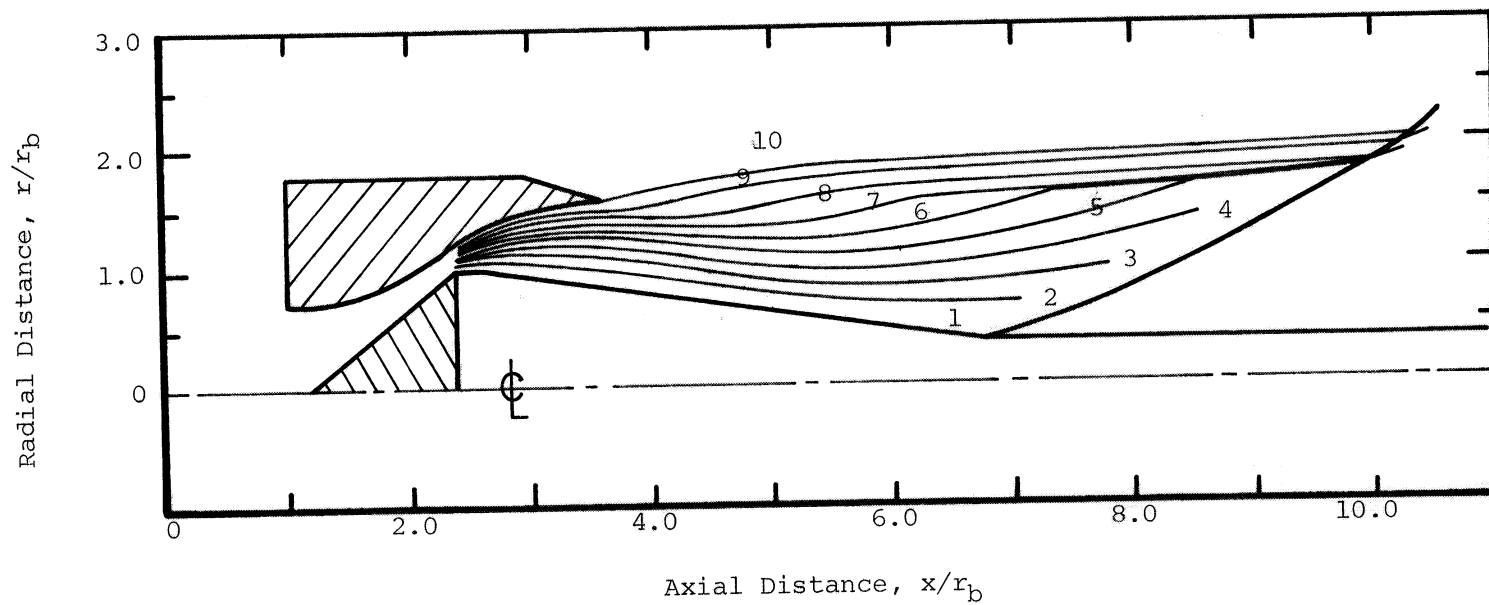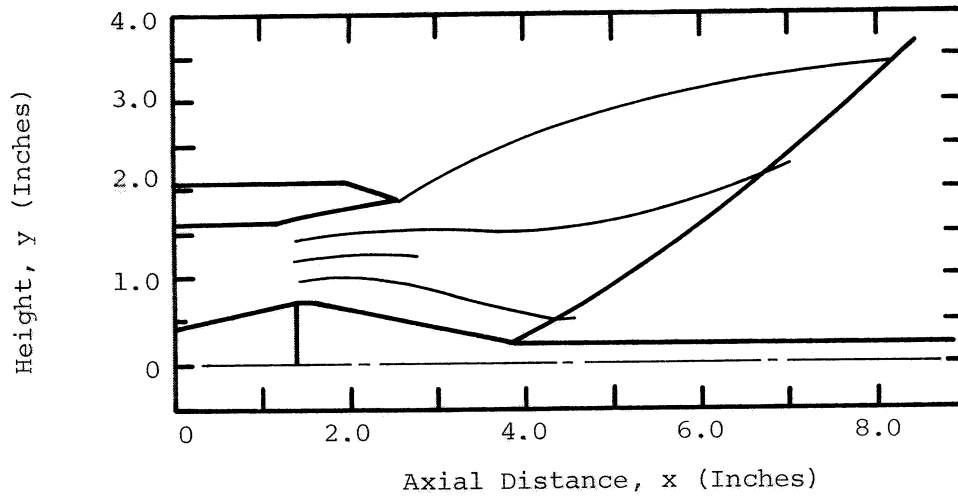
- 119 -
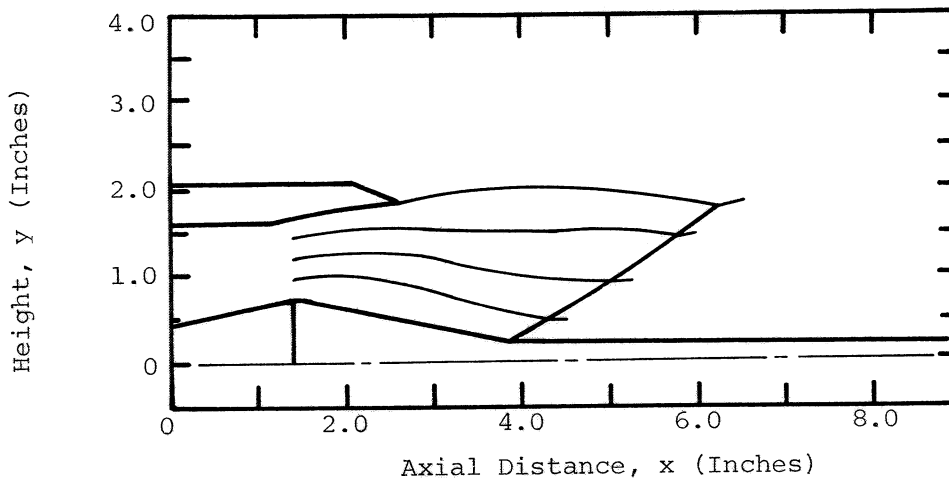
Fig. 52. Internal Shock Formation in an Axisymmetric Expansion-Deflection Nozzle (A_{ne}/A_{nt} = 5.602, A_b/A_{nt} = 2.448).

a.) $P_a/P_{ol} = 0.3401$

b.) $P_a/P_{ol} = 0.10204$

c.) $P_a/P_{ol} = 0.17007$

Fig. 53. Effects of Ambient Pressure on the Flow Field of a Planar Expansion-Deflection Nozzle ($A_{ne}/A_{nt} = 2.007$, $A_b/A_{nt} = 0.8333$).

- 120 -

a.) $P_a/P_{o1} = 0.01020$

b.) $P_a/P_{o1} = 0.02041$
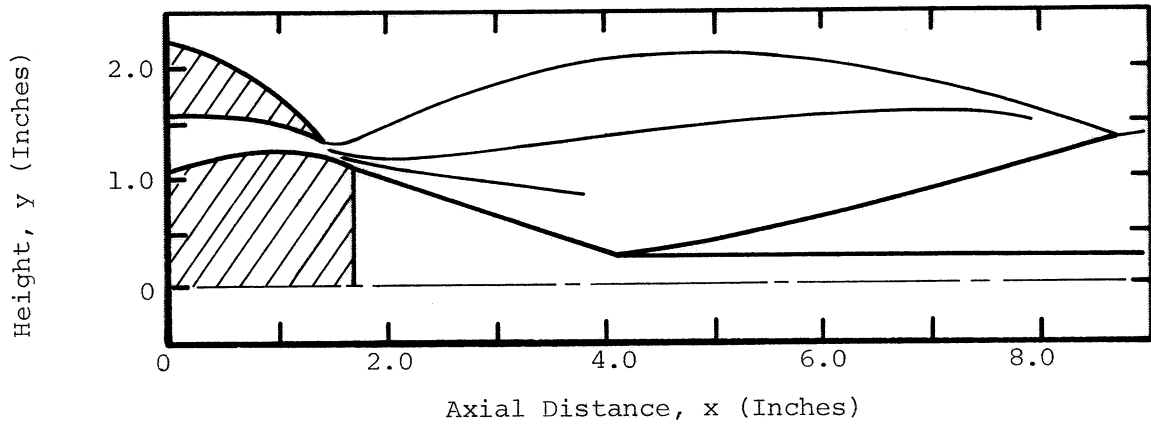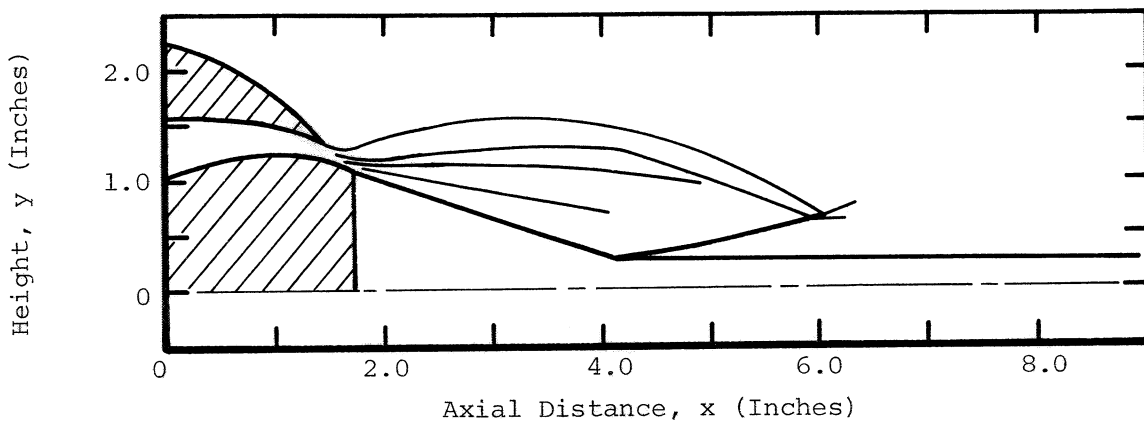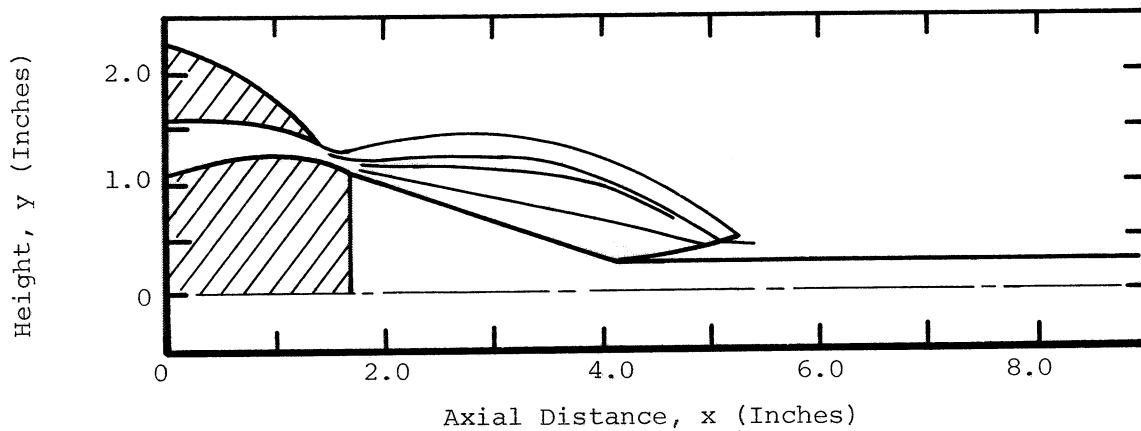
c.) $P_a/P_{o1} = 0.02721$

Fig. 54. Effect of Ambient Pressure on the Flow Field of a Planar
Truncated Plug Nozzle.

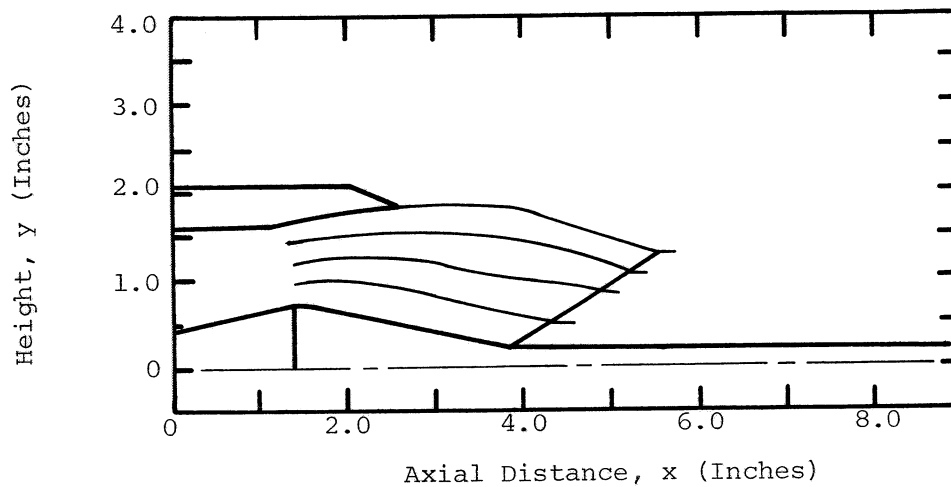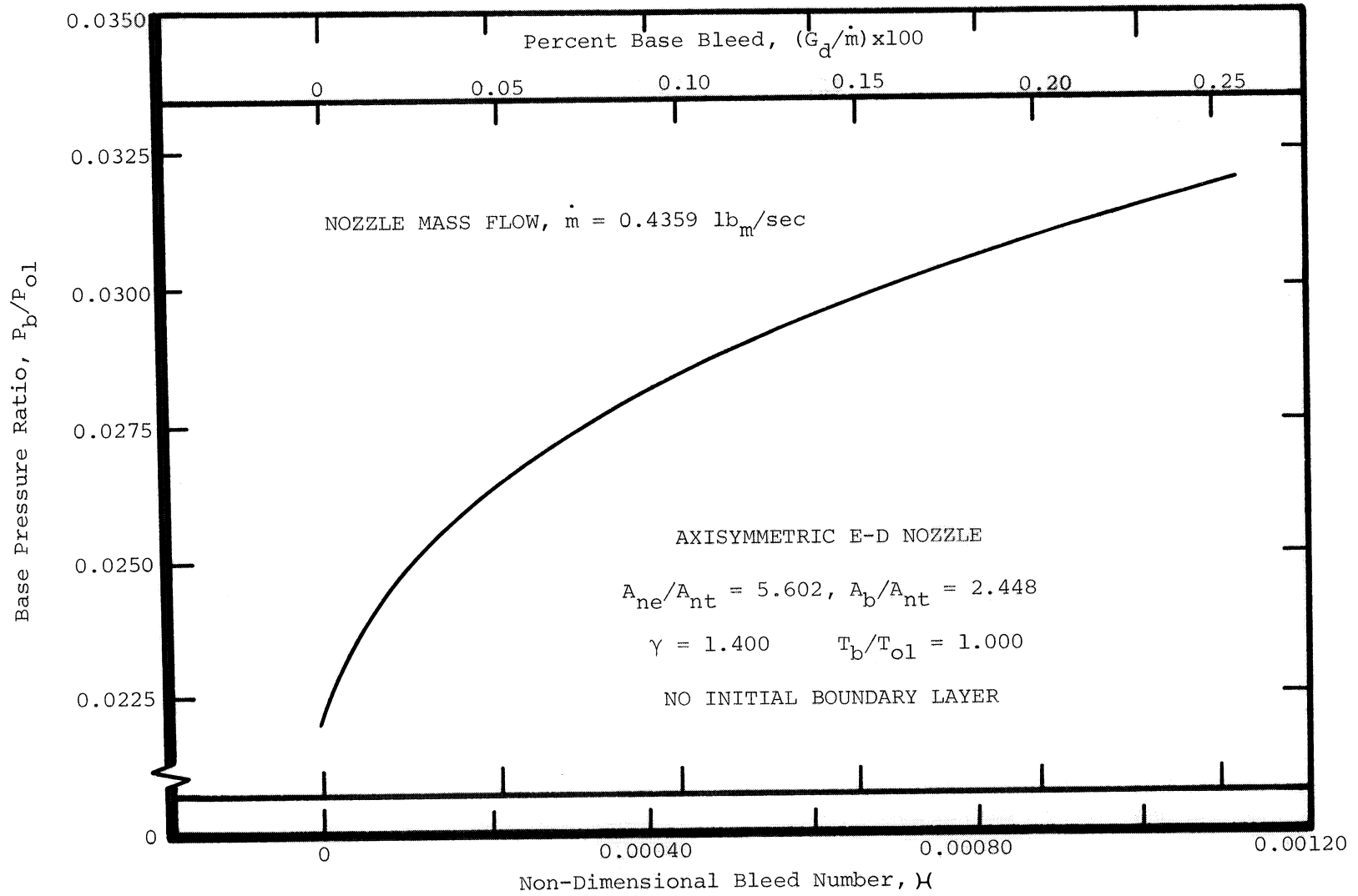Fig. 55. Effect of Base Bleed on the Base Pressure of an Axisymmetric Expansion-Deflection Nozzle.
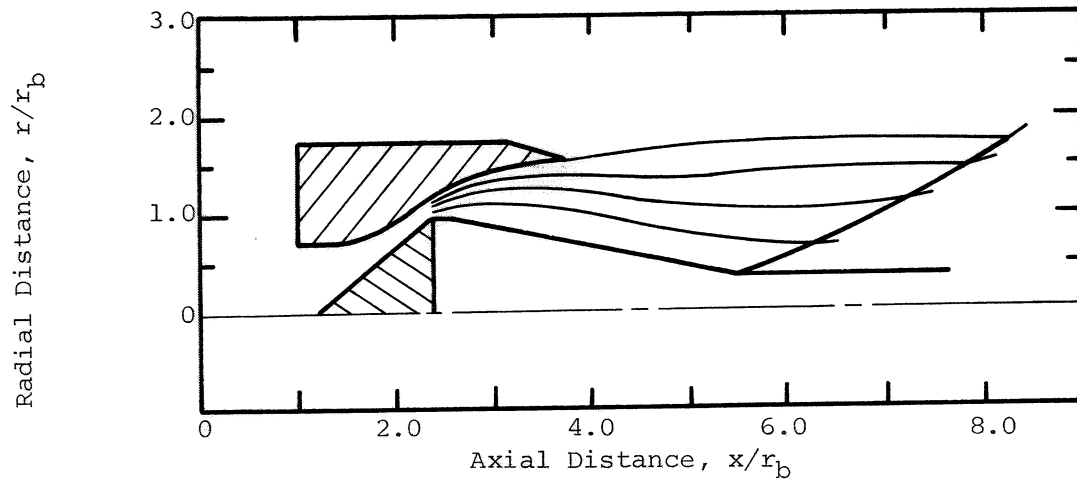
a.) Η = 0 (No Base Bleed)
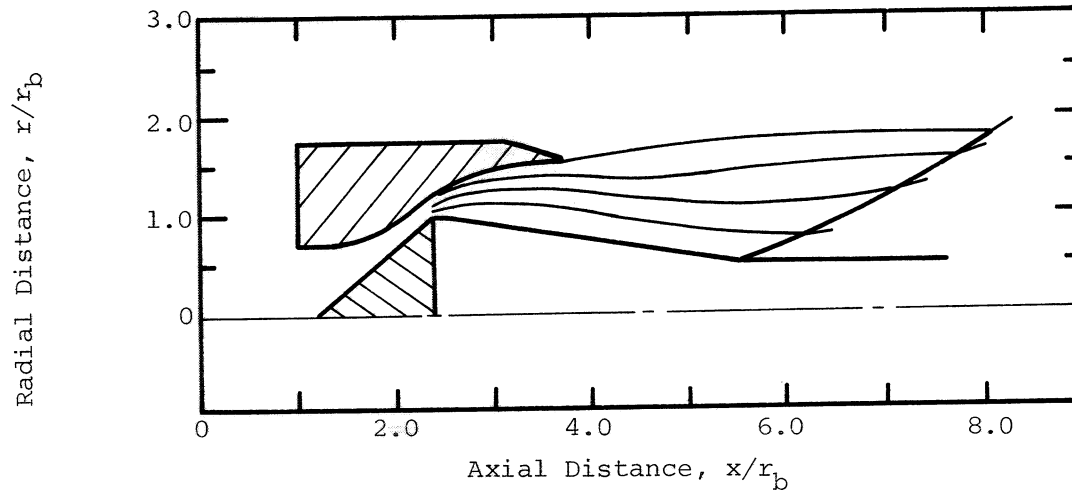
b.) Η = 0.00025841
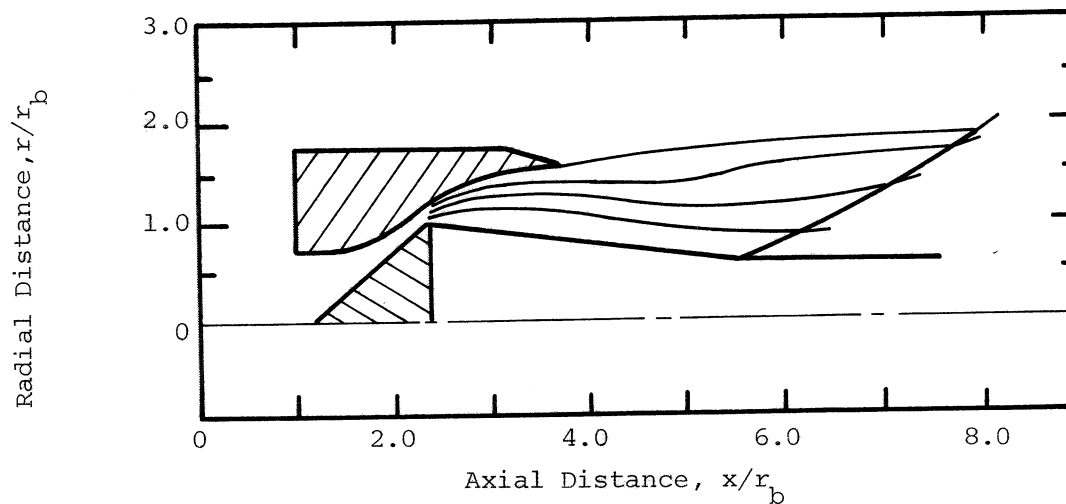
c.) Η = 0.00077703

Fig. 56. Effects of Base Bleed on the Flow Field of an Axisymmetric
Expansion-Deflection Nozzle.

- 123 -
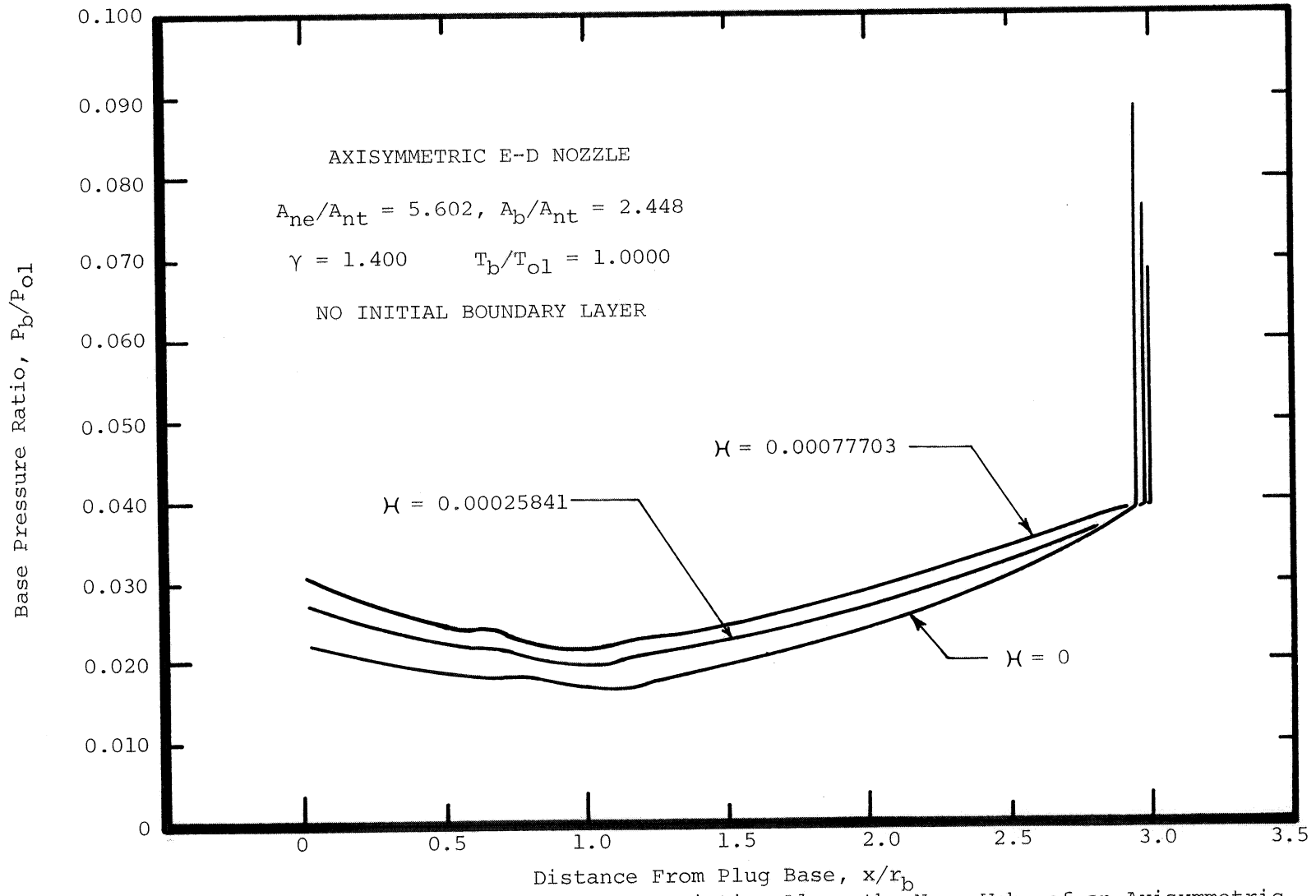
Fig. 57. Base Bleed Effects on the Pressure Variation Along the Near Wake of an Axisymmetric Expansion-Deflection Nozzle.
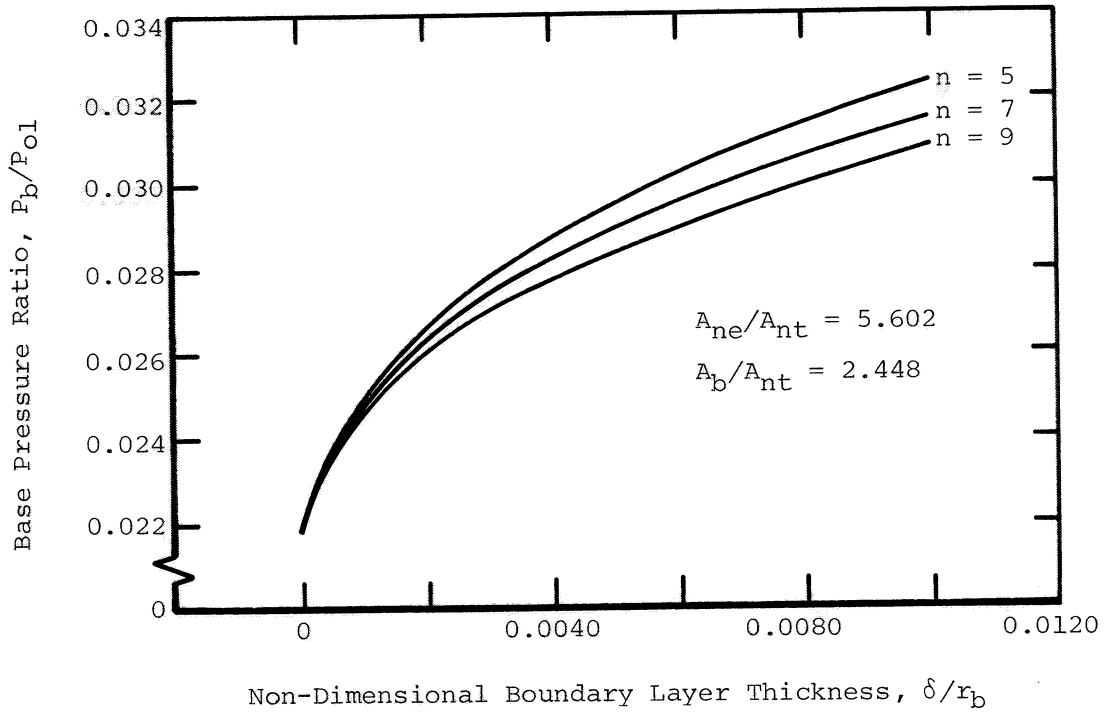
a.) Effect of Boundary Layer Profile Shape and Thickness on the Base Pressure
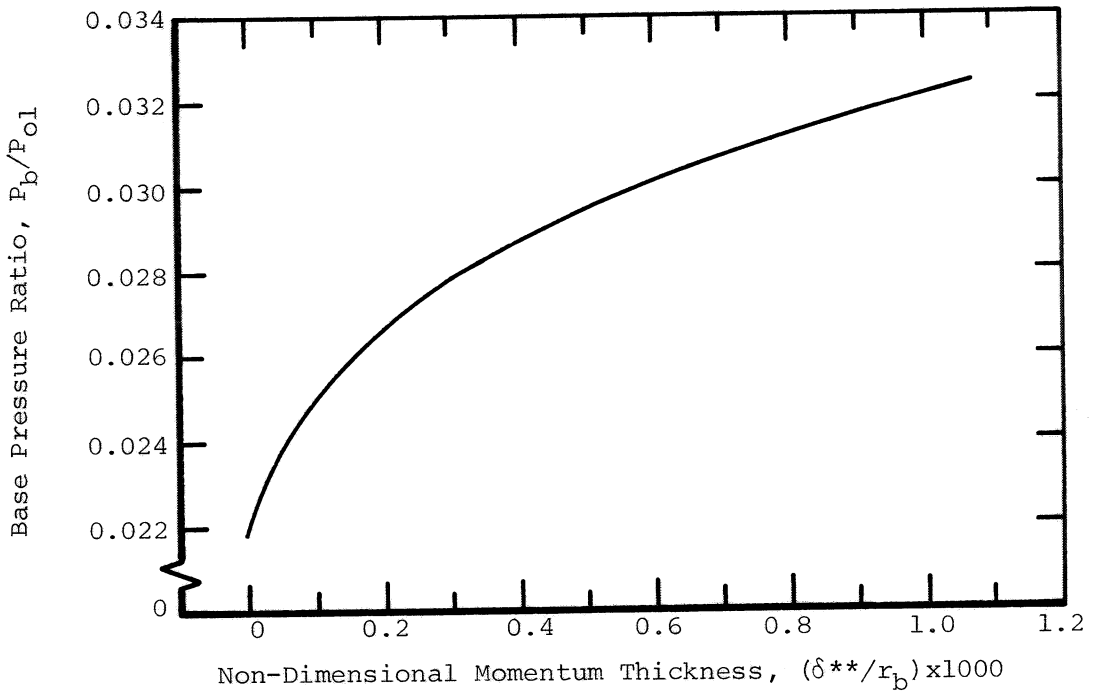
b.) Effect of Momentum Thickness on the Base Pressure.

Fig. 58. Boundary Layer Effects on the Base Pressure of an Axi-summmetric Expansion-Deflection Nozzle.

- 125 -

Fig. 59. Shadowgraph Photograph of the Flow Field of the Axisymmetric Internal-External-Expansion Nozzle.
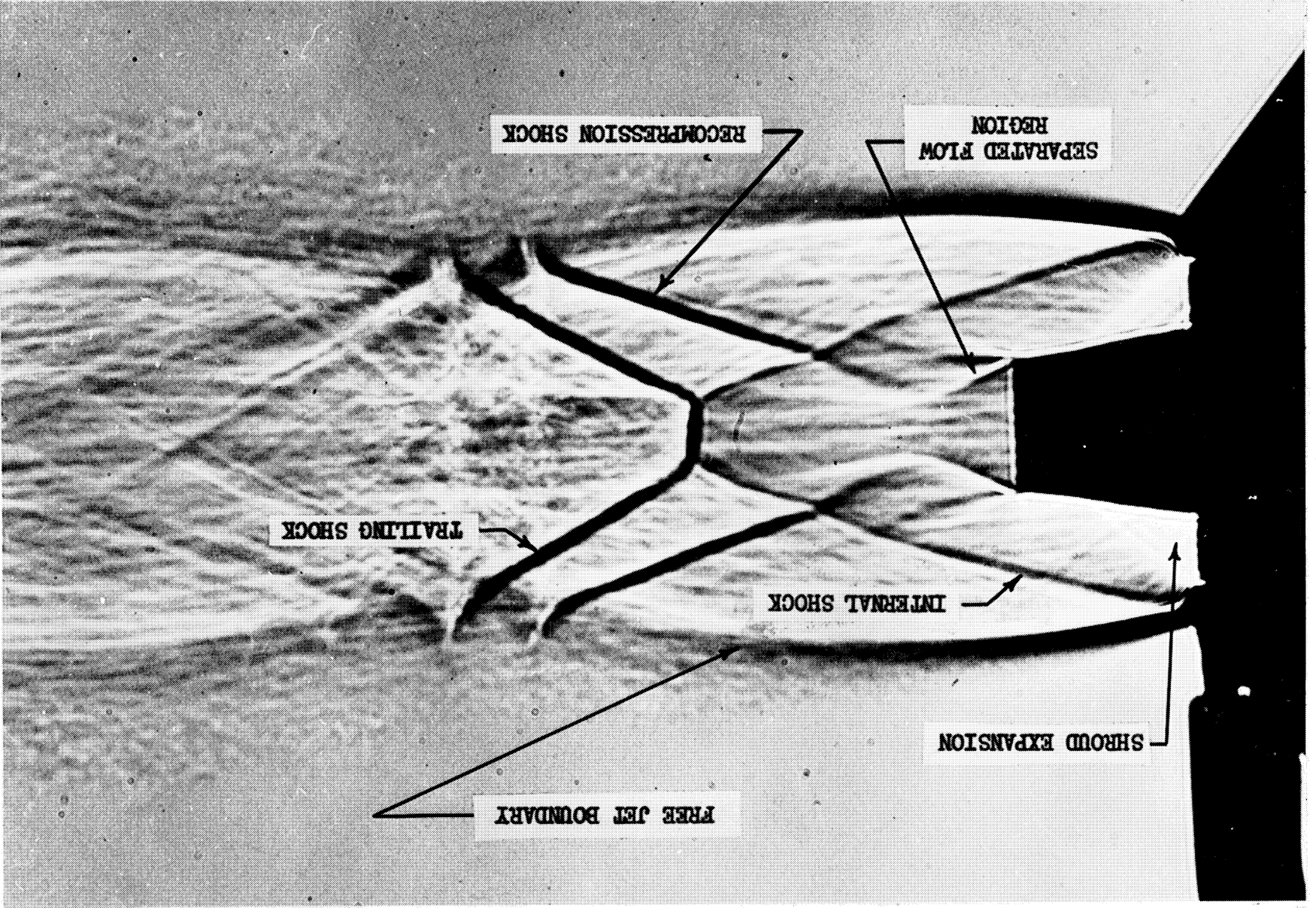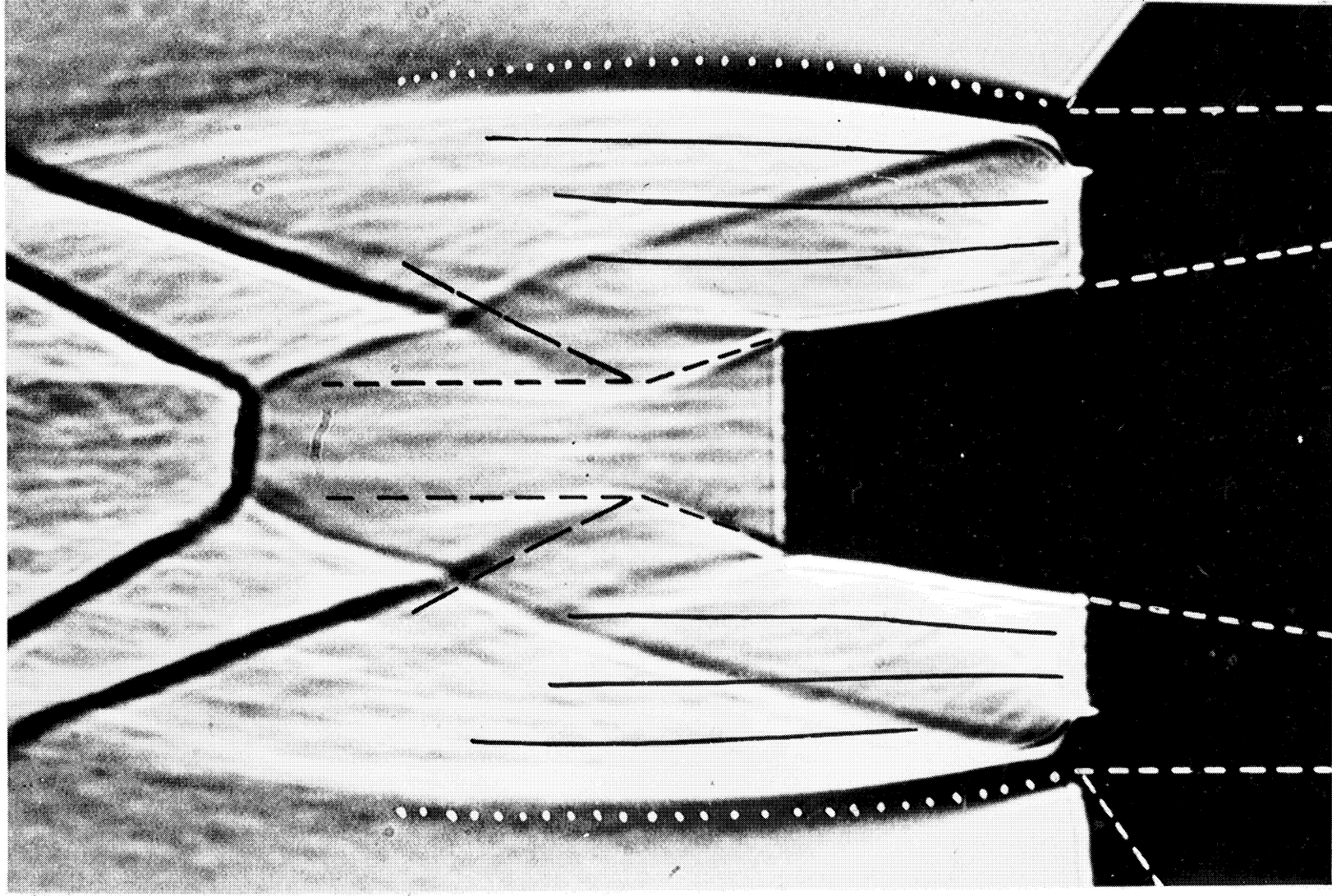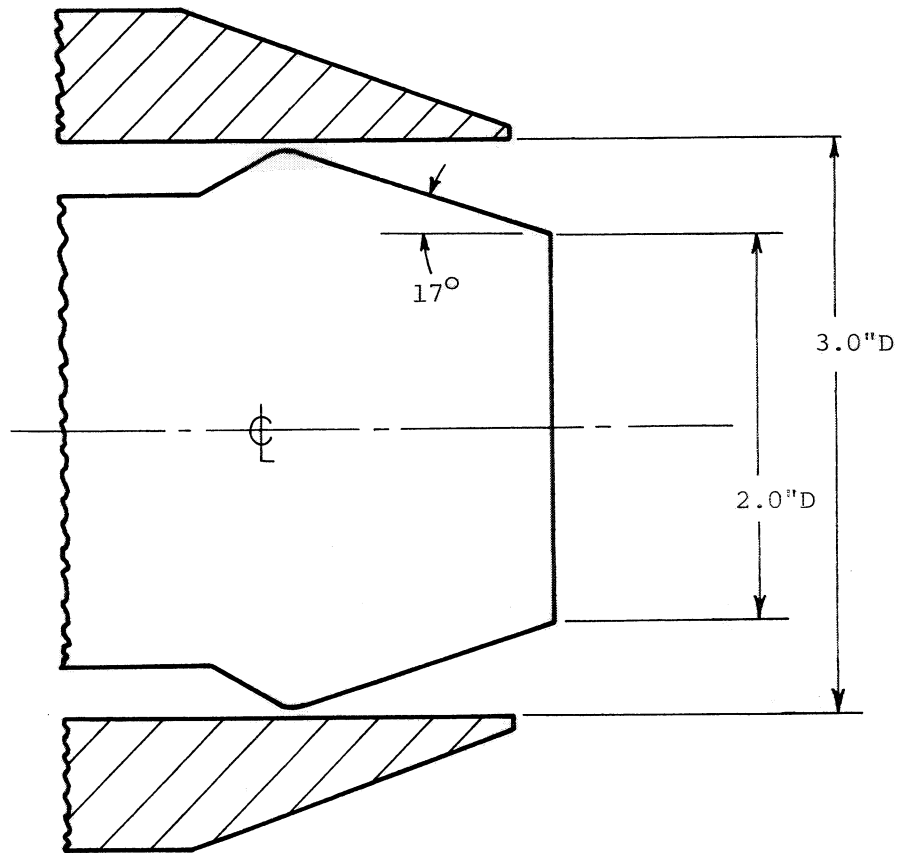
Fig. 61. Schematic of Internal-External-Expansion Nozzle
From Ref. 39.
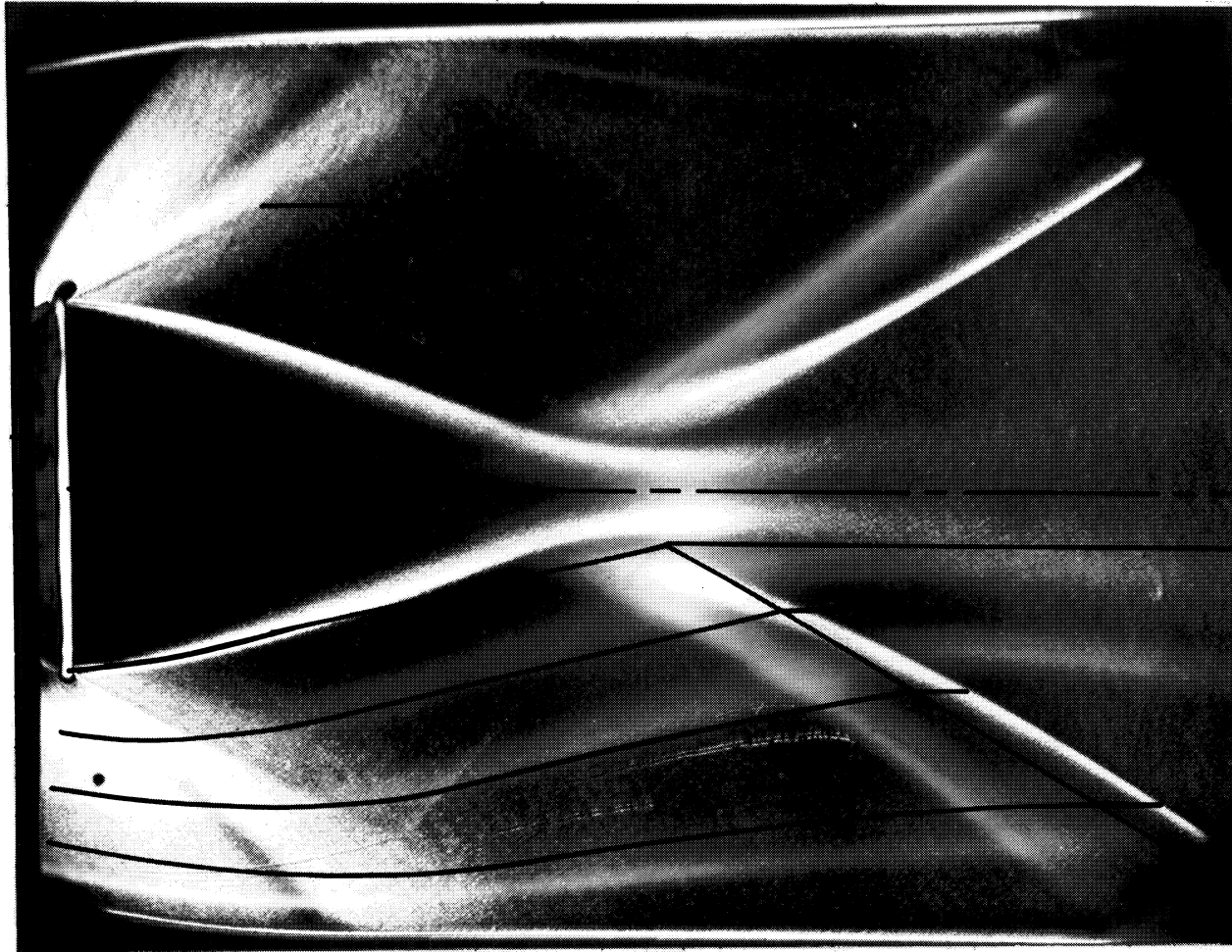
Fig. 62. Comparison Between Analytical Flow Field and Smokeline-Opaque-Stop Schlieren Photograph of Planar Expansion-Deflection Nozzle.

COPIES	RECIPIENT	DESIGNEE
	Ames Research Center NASA Moffett Field, California 94035	
1	A.S. Hertzog, Director of Procurement	(X)
1	Patents and Contracts Management	(X)
	Jet Propulsion Laboratory 4800 Oak Grove Dr. Pasadena, Calif. 91103	
10	Mr. Hartwell R. Long (Technical Manager)	(X)
3	Chief, Liquid Propulsion Technology RPL Office of Advanced Research and Technology NASA Headquarters Washington, D.C., 20546	(X)
1	Director, Technology Utilization Division Office of Technology Utilization NASA Headquarters Washington, D.C. 20546	(X)
20	NASA Scientific and Technical Information Facility P.O. Box 33 College Park, Maryland 20740	(X)
1	Director, Launch Vehicles and Propulsion, SV Office of Space Science and Applications NASA Headquarters Washington, D.C. 20546	(X)
1	Director, Advanced Manned Missions, MT Office of Manned Space Flight NASA Headquarters Washington, D.C. 20546	(X)
1	Mission Analysis Division NASA Ames Research Center Moffett Field, California 24035	(X)

NASA FIELD CENTERS

COPIES	RECIPIENT	DESIGNEE
2	Ames Research Center Moffett Field, California 94035	Hans M. Mark V.D. Reed
1	Goddard Space Flight Center Greenbelt, Maryland 20771	Merland L. Moseson Code 620

NASA FIELD CENTERS

COPIES	RECIPIENT	DESIGNEE
2	Jet Propulsion Laboratory California Institute of Technology 4800 Oak Grove Drive Pasadena, California 91103	Henry Burlage, Jr. Propulsion Div. 38
2	Langley Research Center Langley Station Hampton, Virginia 23365	Ed. Cortwright, Director D.J. Carter P.K. Pierpont
2	Lewis Research Center 21000 Brookpark Road Cleveland, Ohio 44135	B.T. Lundin, Director Dr. H. Mark
2	Marshall Space Flight Center Huntsville, Alabama 35812	Hans G. Paul Code R-P+VED V.F. Henson, S&E,AERO-AA
2	Manned Spacecraft Center Houston, Texas 77001	J.G. Thibodaux, Jr. Chief, Prop. + Power Div. B. Redd
2	John F. Kennedy Space Center, NASA Cocoa Beach, Florida 32931	Dr. Kurt H. Debus

GOVERNMENT INSTALLATIONS

COPIES	RECIPIENT	DESIGNEE
1	Aeronautical Systems Division Air Force Systems Command Wright-Patterson Air Force Base Dayton, Ohio 45433	D.L. Schmidt Code ASRCNC-2 V. Dahlem Code FDMG
1	Air Force Missile Development Center Holloman Air Force Base New Mexico 88330	
1	Air Force Missile Test Center Patrick Air Force Base, Florida	L.J. Ullian
1	Space and Missile Systems Organization Air Force Unit Post Office Los Angeles, California 90045	Col. Clark Technical Data Center Lt. J.F. Turk
1	Arnold Engineering Development Center Arnold Air Force Station Tullahoma, Tennessee 37388	Dr. H.K. Doetsch

GOVERNMENT INSTALLATIONS

COPIES	RECIPIENT	DESIGNEE
1	Bureau of Naval Weapons Department of the Navy Washington, D.C. 20546	J. Kay RTMS-41
1	Defense Documentation Center Hdqtrs. Cameron Station, Building 5 5010 Duke Street Alexandria, Virginia 22314 Attn: TISIA	
1	Headquarters, U.S. Air Force Washington, D.C. 20546	Col. C.K. Stambaugh AFRST
1	Picatinny Arsenal Dover, New Jersey 07801	I. Forsten, Chief Liquid Propulsion Laboratory
2	Air Force Rocket Propulsion Laboratory Research and Technology Division Air Force Systems Command Edwards, California 93523	RPRPD/Mr. H. Main Dr. L. Quinn C.H. Allen
1	U.S. Army Missile Command Redstone Arsenal Alabama 35809	Mr. Walter Wharton Dr. S.P.D. Smith
1	U.S. Naval Ordnance Test Station China Lake California 93557	Code 4562 Chief, Missile Propulsion Div.

CPIA

1	Chemical Propulsion Information Agency Applied Physics Laboratory 8621 Georgia Avenue Silver Spring, Maryland 20910	Tom Reedy T.M. Gilliland

INDUSTRY CONTRACTORS

1	Aerojet-General Corporation P.O. Box 296 Azusa, California 91703	W.L. Rogers
1	Aerojet-General Corporation P.O. Box 1947 Technical Library, Bldg.2015,Dept.2410 Sacramento, California 95809	R. Stiff Dr. V. H. Ransom

INDUSTRY CONTRACTORS

COPIES	RECIPIENT	DESIGNEE
1	Space Division Aerojet-General Corporation 9200 East Flair Dr. El Monte, California 91734	S. Machlawski
1	Aerospace Corporation 2400 East El Segundo Boulevard P.O. Box 95085 Los Angeles, California 90045	John G. Wilder MS-2293
1	Atlantic Research Corporation Edsall Road and Shirley Highway Alexandria, Virginia 22314	Dr. Ray Friedman
1	Avco Systems Division Wilmington, Massachusetts	Howard B. Winkley
1	Beech Aircraft Corporation Boulder Division Box 631 Boulder, Colorado	J.H. Rodgers
1	Bell Aerosystems Company P.O. Box 1 Buffalo, New York 14240	W.M. Smith
1	Bell Comm 955 L'Enfant Plaza, S.W. Washington, D.C.	H.S. London
1	Bendix Systems Division Bendix Corporation 3300 Plymouth Road Ann Arbor, Michigan 48105	John M. Brueger
1	Boeing Company P.O. Box 3707 Seattle, Washington 98124	J.D. Alexander E.D. Simon
1	Boeing Company 1625 K Street, N.W. Washington, D.C. 20006	Library
1	Boeing Company P.O. Box 1680 Huntsville, Alabama 35801	Ted Snow

INDUSTRY CONTRACTORS

COPIES	RECIPIENT	DESIGNEE
1	Missile Division Chrysler Corporation P.O. Box 2628 Detroit, Michigan 48231	Mr. John Gates
1	Wright Aeronautical Division Curtiss-Wright Corporation Wood-Ridge, New Jersey 07075	G. Kelley
1	Research Center Fairchild Hiller Corporation Germantown, Maryland	Ralph Hall
1	Republic Aviation Corporation Fairchild Hiller Corporation Farmingdale, Long Island, New York	Library
1	General Dynamics, Convair Division Library & Information Services (128-00) P.O. Box 1128 San Diego, Calif. 92112	Frank Dore
1	Missile and Space Systems Center General Electric Company Valley Forge Space Technology Center P.O. Box 8555 Philadelphia, Pa.	F. Mezger F.E. Schultz J.R. Rausch
1	Grumman Aircraft Engineering Corp. Bethpage, Long Island New York 11714	Joseph Gavin R. Haslet
1	Honeywell, Inc. Aerospace Div. 2600 Ridgway Rd. Minneapolis, Minn.	Mr. Gordon Harms
1	Hughes Aircraft Co. Aerospace Group Centinela and Teale Streets Culver City, Calif. 90230	E.H. Meier V.P. and Div. Mgr., Research & Dev. Div.
1	Walter Kidde and Company, Inc. Aerospace Operations 567 Main Street Belleville, New Jersey	R.J. Hanville Dir. of Research Eng.

INDUSTRY CONTRACTORS

COPIES	RECIPIENT	DESIGNEE
1	Ling-Temco-Vought Corporation P.O. Box 5907 Dallas, Texas 75222	
1	Arthur D. Little, Inc. 20 Acorn Park Cambridge, Massachusetts 02140	Library
1	Lockheed Missiles and Space Co. Attn: Technical Information Center P.O. Box 504 Sunnyvale, California 94088	J. Guill C.F. Ehrlich
1	Lockheed Propulsion Company P.O. Box 111 Redlands, California 92374	H.L. Thackwell
1	The Marquardt Corporation 16555 Saticoy Street Van Nuys, Calif. 91409	Howard McFarland R. C. Stechman
1	Baltimore Division Martin Marietta Corporation Baltimore, Maryland 21203	Mr. John Calathes (3214)
1	Denver Division Martin Marietta Corporation P.O. Box 179 Denver, Colorado 80201	Dr. Morganthaler A.J. Kullas L'.E. Fidler
1	Orlando Division Martin Marietta Corp. Box 5837 Orlando, Florida	J. Ferm
1	Astropower Laboratory Mc Donnell-Douglas Aircraft Co. 2121 Paularino Newport Beach, California 92663	Dr. George Moc Director, Research
1	McDonnel-Douglas Aircraft Corp. P.O. Box 516 Municipal Airport St. Louis, Missouri 63166	R.A. Herzmark
1	McDonnell-Douglas Astronautics Co. Bolsa Chica Avenue Huntington Beach, California 92640	R.J. Hoffman

INDUSTRY CONTRACTORS

COPIES	RECIPIENT	DESIGNEE
1	Missile and Space Systems Division McDonnell-Douglas Aircraft Company 3000 Ocean Park Boulevard Santa Monica, Calif. 90406	Mr. R.W. Hallet Chief Engineer Adv. Space Tech.
1	Space & Information Systems Div. North American Rockwell 12214 Lakewood Boulevard Downey, California 90241	F.G. Etheridge
1	Rocketdyne (Library 586-306) 6633 Canoga Avenue Canoga Park, Calif. 91304	Dr. R.J. Thompson S.F. Iacobellis J.C. Hyde
1	Northrop Space Laboratories 3401 West Broadway Hawthorne, California 90250	Dr. William Howard
1	Aeronutronic Division Philco Corporation Ford Road Newport Beach, California 92663	D.A. Garrison
1	Astro-Electronics Division Radio Corporation of America Princeton, New Jersey 08540	Y.Brill
1	Rocket Research Corporation York Center Redmond, Washington 98052	Foy McCullough, Jr. T.A. Groudle
1	Sunstrand Aviation 2421 11th Street Rockford, Illinois 61101	R.W. Reynolds
1	Stanford Research Institute 333 Ravenswood Avenue Menlo Park, California 94025	Dr. Gerald Marksman
1	TRW Systems Group TRW Incorporated One Space Park Redondo Beach, Calif. 90278	G.W. Elverum S.S. Cherry
1	Tapco Division TRW, Incorporated 23555 Euclid Avenue Cleveland, Ohio 44117	P.T. Angell

INDUSTRY CONTRACTORS

COPIES	RECIPIENT	DESIGNEE
1	Thiokol Chemical Corporation Huntsville Division Huntsville, Alabama 35807	John Goodloe
1	Research Laboratories United Aircraft Corp. 400 Main St. East Hartford, Conn. 06108	Erle Martin
1	Hamilton Standard Division United Aircraft Corp. Windsor Locks, Conn. 06096	Mr. R. Hatch
1	United Technology Center 587 Methilda Avenue P.O. Box 358 Synnyvale, California 94088	Dr. David Altman
1	Florida Research and Development Pratt and Whitney Aircraft United Aircraft Corporation P.O. Box 2691 West Palm Beach, Florida 33402	R.J. Coar L.E. Ruby
1	Vickers, Inc. Box 302 Troy, Michigan	
1	Sandia Corporation P.O. Box 5000 Albuquerque, New Mexico	Dr. J.K. Cole
1	Avco Corporation Avco Space Systems Div. Lowell Industrial Park Lowell, Mass. 01851	Dr. R.L. Reeves
1	Consolidated Engineering Technology Corp. 188 Whisman Road Mountain View, Calif. 94040	Dr. R. Anderson
1	G.V.R. Rao and Associates 14827 Ventura Boulevard Sherman Oaks, Calif. 91403	G.V.R. Rao

INDUSTRY CONTRACTORS

COPIES	RECIPIENT	DESIGNEE
1	Lockheed Missiles and Space Co. Huntsville Research and Engineering Center 4800 Bradford Drive Huntsville, Alabama	J.W. Benefield R.J. Prozan
1	Cornell Aeronautical Laboratory, Inc. Buffalo, New York 14221	Dr. J.G. Hall K. Hendershot